

ABSTRACT

KIM, EUNJUNG. Computational Biomechanical Models for the Pericellular Matrix of Articular Cartilage. (Under the direction of Dr. Mansoor A. Haider).

Articular cartilage is a resilient biological soft tissue that serves to support load in diarthrodial joints such as the knee, shoulder and hip. Cartilage can be idealized as a biphasic mixture that is comprised of a solid extracellular matrix (ECM) saturated by interstitial fluid. Cartilage ECM is maintained by a sparse population of cells called chondrocytes, which are surrounded by a narrow layer called the pericellular matrix (PCM). Together, the chondrocyte and its surrounding PCM are termed the chondron. Since cartilage is avascular and aneural, cell metabolic activity is highly dependent upon the mechanical characteristics of the local extracellular environment. However, the relationships between microscopic and macroscopic biphasic mechanical variables are not well understood. This research is motivated by the need to quantify these relationships. Two computational models were developed pertaining to mechanical interactions between the cells, the PCM and the ECM of articular cartilage.

In the first study, a transient finite element model (FEM) was developed for linear biphasic mechanics in the microscopic environment of a single cell within a cartilage layer under cyclic loading in confined compression. The microscopic domain was modeled as a micron-scale cylinder of ECM with a spherical inclusion arising from the presence of a single cell and its encapsulating PCM. Boundary conditions for the three-zone microscale model were generated using an analytical solution for macroscopic cyclic confined compressive loading of a cartilage layer. To perform these simulations, an axisymmetric displacement-velocity penalty biphasic FEM was implemented as a weak formulation in the software package Comsol Multiphysics. Accuracy of the implementation was verified against known analytical solutions for cyclic compressive loading of a biphasic layer, and dynamic radial deformation of a layered biphasic sphere. The microscale biphasic FEM was employed to analyze the effects of frequency on biphasic mechanical variables in the cellular microenvironment under macroscopic cyclic confined compressive loading at 1% engineering strain, and in the frequency range 0.01-1 Hz.

The second investigation consisted of the formulation, implementation and application of a multiscale axisymmetric elastic boundary element method (BEM) for simulating *in situ* chondron deformation in states of mechanical equilibrium within a cartilage explant under equilibrated unconfined compression. The microscopic domain was modeled as a micron-scale sphere of ECM with an ellipsoidal inclusion, representing the chondron. Boundary conditions for this microscale model were generated using a known analytical solution for unconfined compression of a cartilage layer. Accuracy of the three-zone BEM was evaluated and compared to analytical solutions and finite element solutions. The BEM was then integrated with a nonlinear optimization technique (Nelder-Mead) to determine PCM elastic properties *in situ* within the ECM of the cartilage explant by solving an inverse problem associated with the experimental data.

Computational Biomechanical Models for the Pericellular Matrix of
Articular Cartilage

by
Eunjung Kim

A dissertation submitted to the Graduate Faculty of
North Carolina State University
in partial fulfillment of the
requirements for the Degree of
Doctor of Philosophy

Applied Mathematics

Raleigh, North Carolina

2009

APPROVED BY:

Dr. Zhilin Li

Dr. Ralph C. Smith

Dr. Mansoor A. Haider
Chair of Advisory Committee

Dr. Farshid Guilak

BIOGRAPHY

Eunjung Kim was born on a late March morning in 1978. She is the daughter of Haengjo Kong and Haejoo Kim, and the sister of Yongsu Kim. She grew up in Masan, a southeast coastal city in the Republic of Korea, until she graduated from high school. After completing her high school education, she moved to Seoul to pursue her undergraduate studies at Ewha University. She earned a Bachelor of Science with honors in Mathematics in 2002 and continued to study mathematics in graduate school under the direction of Dr. Sunyoung Kim, obtaining her Masters of Science degree in 2004. In 2005, she entered the Department of Mathematics at North Carolina State University to pursue her doctoral studies. Under the supervision of her thesis advisor, Dr. Mansoor Haider, Eunjung conducted interdisciplinary research in modeling the mechanics of biological soft tissue. During this time, she married the first love of her life, Jaeyoung, who was a graduate student at the Department of Environmental and Molecular Toxicology at North Carolina State University. In June 2009, Eunjung will join The Interdisciplinary Center for the Study of Biocomplexity at the University of Notre Dame as a Postdoctoral Fellow.

ACKNOWLEDGMENTS

This degree would not have been possible without help of many people, especially Dr. Mansoor Haider. He has always been superb in providing exceptionally correct direction to my study, and in a very kind way. Under his guidance, I have learned a great deal of valuable and useful knowledge, and I have learned how to think as a scientist. Indeed, the past four years have been some of the most important and formative of my life, and I am tremendously grateful for Dr. Haider's mentoring during this important time.

For ideas and data related to this research, I am deeply grateful to Dr. Farshid Guilak of Orthopedic Surgery and Biomedical Engineering at Duke University.

I would like to thank my advisory committee, comprised of Dr. Ralph Smith, Dr. Zhilin Li, Dr. Guilak, and Dr. Mansoor Haider, for taking the time to serve on my committee, and for their guidance, recommendations, and help with my search for a postdoctoral position. I also extend my gratitude to all of the mathematics faculty and administrative staff at North Carolina State University.

I am also sincerely thankful to my friends who I grew up with, suffered with, and celebrated with during this difficult process. Whether by studying with me or listening to my practice presentations, thank you all so much for your time, your support, your well wishes, and your friendship. I am truly grateful!

I would like to thank my family. Thanks Mom and Dad for all of the unconditional love, guidance, and support. Thanks to my brother for his true friendship, his humor, and his support. Also, I wish to express my appreciation to my parents-in-law and my brother-in-law whose support and understanding have made this work possible.

I would like to express my utmost thanks to my husband, who endured this long process with me, always offering support, love, patience, and who will always be with me.

I am grateful to the Whitaker Foundation (RG-020933) and the National Institutes of Health (AG-15768) for their financial support of my Research Assistantship during the course of this research.

TABLE OF CONTENTS

LIST OF TABLES.....	vi
LIST OF FIGURES	vii
1 Introduction and Background.....	1
2 Finite Element Modeling of Microscale Biphasic Mechanics in Articular Cartilage under Dynamic Loading	7
2.1 Biphasic Theory	8
2.1.1 Biphasic Governing Equations	9
2.1.2 Biphasic Governing Equations at Equilibrium	10
2.2 Multiscale Model	10
2.2.1 Finite Element Modeling of Microscale Cartilage Deformation under Dynamic Loading	11
2.2.2 Mixed Penalty Weak Formulation	12
2.2.3 Axisymmetric Specialization of Weak Formulation	13
2.2.4 Implementation of the Axisymmetric Weak Formulation	16
2.2.5 Macroscale Modeling of Cartilage Deformation	18
2.2.6 Microscale Modeling of Cartilage Deformation	21
3 Simulations of the Dynamic Mechanical Environment of the Chondrocyte	23
3.1 Material Properties	23
3.2 Mesh Refinement and Verification	24
3.3 Simulations of Dynamic Cell-Matrix Interactions	30
3.3.1 Force Transmission	30
3.3.2 Strain Transmission	31
3.3.3 Osteoarthritis (OA) Effects on Strain Transmission	37
3.3.4 Discussion	37
4 Axisymmetric Elastic Boundary Element Method for Domains with Internal Interfaces	42
4.1 Axisymmetric Boundary Integral Formulation	43
4.1.1 Cartesian Boundary Integral Equations	43
4.1.2 Axisymmetric Boundary Integral Equations	48
4.1.3 Evaluation of C_{ij}	51
4.1.4 Domains with Internal Interfaces	51
4.2 Numerical Implementation	53
4.2.1 Discretization of the Boundary and Interfaces	54
4.2.2 Discretization of Boundary Integral Equations	55

4.2.3	Numerical Integration	58
4.2.4	Boundary Conditions and Assembly	61
5	Application of Axisymmetric Elastic BEM for Estimation of Pericellular Matrix Properties	64
5.1	Verification of BEM Model	65
5.2	Experimental Data for In Situ Chondron Deformation	75
5.3	Inverse Problem	76
5.4	Parameter Estimation	79
5.5	Results	80
5.6	Discussion	88
	Bibliography	91

LIST OF TABLES

Table 3.1 Material properties for the model of microscale biphasic mechanics based on [6]. In the presence of osteoarthritis (OA), Young's modulus of the PCM was significantly decreased, and the permeability was significantly elevated for both the PCM and the ECM.	24
Table 5.1 Chondrons' morphological parameters at superficial, middle and deep zones. Left columns in each zone represent uncompressed data and right columns represent deformed shapes under 10% compressive strain, from [30].	75
Table 5.2 Chondrocytes' morphological parameters at superficial, middle and deep zones. Left columns in each zone represent uncompressed data and right columns represent deformed shapes under 10% compressive strain, from [30].	76
Table 5.3 One parameter estimation of E_{PCM} with the cost function (5.7) and $\nu_{ECM} = \nu_{PCM} = 0.04$	82
Table 5.4 One parameter estimation of E_{PCM} with the cost function (5.7) and $\nu_{ECM} = \nu_{PCM} = 0.12$	83
Table 5.5 Two parameter estimation of E_{PCM} and ν_{PCM} with the cost function (5.7) and $\nu_{ECM} = 0.04$	83
Table 5.6 Two parameter estimation of E_{PCM} and ν_{PCM} with the cost function (5.7) and $\nu_{ECM} = 0.12$	83
Table 5.7 Two parameter estimation of E_{PCM} and ν_{PCM} with the cost function (5.8) and $\nu_{ECM} = 0.04$	86
Table 5.8 Two parameter estimation of E_{PCM} and ν_{PCM} with the cost function (5.8) and $\nu_{ECM} = 0.12$	86

LIST OF FIGURES

Figure 1.1 (a) Articular cartilage in a knee joint (b) A layer of articular cartilage showing presence of cells (chondrocytes) (Reprinted from Osteoarthritis and Cartilage, 2/2, Farshid Guilak, B. Christoph Meyer, Anthony Ratcliffe and Van C. Mow, The effects of matrix compression on proteoglycan metabolism in articular cartilage explants, 91-101., Copyright (1994), with permission from Elsevier.). (c) An isolated chondron (Reprinted from Osteoarthritis and Cartilage, 7/1, Farshid Guilak, Wendy R. Jones, H. Ping Ting-Beall and Greta M. Lee, The deformation behavior and mechanical properties of chondrocytes in articular cartilage, 57-70., Copyright (1999), with permission from Elsevier.).	2
Figure 2.1 Modeling the micromechanical environment in articular cartilage. (a) A layer of articular cartilage (Reprinted from Osteoarthritis and Cartilage, 2/2, Farshid Guilak, B. Christoph Meyer, Anthony Ratcliffe and Van C. Mow, The effects of matrix compression on proteoglycan metabolism in articular cartilage explants, 91-101., Copyright (1994), with permission from Elsevier.). (b) Microscale domain with a single cell, its encapsulating pericellular matrix (PCM) and extracellular matrix (ECM).	11
Figure 2.2 (a) A linear triangular element with local nodes, (b) a quadratic triangular element and (c) an example of a linear basis function $\psi_1(r_1, z_1)$.	16
Figure 2.3 Macroscopic <i>in vitro</i> confined compression test for cartilage explant under dynamic loading.	19
Figure 2.4 (a) Geometry and FEM mesh for simulation of microscale mechanical interactions between the chondron and ECM. (b) A square lattice arrangement of microscale domains in cartilage was used to estimate the dimensions of the mesh consistent with a 1% cell volume fraction.	22
Figure 3.1 The center of the microscale domain was taken at 50% depth, where the tissue thickness was $h = 1$ mm. The microscale domain was located between $z = 0.481 - 0.519$ mm.	24
Figure 3.2 Representative points : $3.8\mu m$ below the top of the microscale domain, $0.25\mu m$ below the cell-PCM interface and $0.5\mu m$ below the PCM-ECM interface.	25
Figure 3.3 Mesh refinement performed at loading frequency $f = 0.1$ Hz, to verify numerical convergence. The number of elements chosen were 274, 551, 784, and 1624.	

The results are shown for (a) pore pressure (ECM) and (b) axial strain (ECM) (c) axial (PCM) strain, and (d) cellular strain at representative points in Figure 3.2..	26
Figure 3.4 Effects of penalty number as it was varied from $\beta = 10^{12}$ to $\beta = 10^{22}$ performed at $f = 0.1$ Hz and shown for (a) pore pressure (ECM), and (b) axial strain (ECM), (c) axial strain (PCM), and (d) cellular axial strain at the three representative points (Figure 3.2).....	27
Figure 3.5 Verification of the biphasic finite element model (symbols) against analytical solution (2.41) and (2.43) for cyclic radial deformation (0.1 Hz). Comparisons are shown for (a) axial strain and (b) pore pressure at a point along the symmetry of axis at 50% height in the microscale domain.....	28
Figure 3.6 Verification of the biphasic finite element model (symbols) against a previous numerical solution [49] for cyclic radial deformation (0.1 Hz). Radial strain (top) and pore pressure (bottom) are shown at the chondron boundary and cell-PCM interface.	29
Figure 3.7 Simulations of pore pressure (a) and solid stress (b) transmitted to the microscale domain via normal ECM. Responses are shown at $z = 0.519$ mm for five different loading frequencies in the range of $f = 0.01 - 0.1$ Hz.	30
Figure 3.8 Illustration of force transmission at three points along the symmetry axis at 90% of the cell radius, 90% of the PCM thickness and at the top of the microscale domain (ECM). Axial solid stress is shown at four loading frequencies: (a) $f = 0.01$ Hz, (b) $f = 0.05$ Hz, (c) $f = 0.02$ Hz, and $f = 0.1$ Hz.....	32
Figure 3.9 Spherical stress distribution in the microscale domain. Spherical solid stress is shown after 4.5 loading cycles for loading frequencies: (a) $f = 0.01$ Hz, (b) $f = 0.05$ Hz and (c) $f = 0.1$ Hz.	33
Figure 3.10 Simulations of axial strain transmitted to the microscale domain via normal ECM shown at the top and bottom of the microscale domain for loading frequencies: (a) $f = 0.01$ Hz, (b) $f = 0.05$ Hz, (c) $f = 0.05$ Hz and (d) $f = 0.1$ Hz.....	34
Figure 3.11 Simulations of axial strain amplification within the chondron via representative points (Figure 3.2) with the loading frequencies: (a) $f = 0.01$ Hz, (b) $f = 0.05$ Hz, (c) $f = 0.05$ Hz and (d) $f = 0.1$ Hz.....	35
Figure 3.12 Spatial profiles of axial strain magnitude at times corresponding to peak strain amplification for $f = 0.01$ Hz ((a) $t=80$ s), $f = 0.05$ Hz ((b) $t=50$ s) and $f = 0.1$ Hz ((c) $t=70$ s), and steady state amplification at local minima for $f = 0.01$ Hz ((d) $t=480$ s), $f = 0.05$ Hz ((e) $t=450$ s) and $f = 0.1$ Hz ((f) $t=490$ s).	36
Figure 3.13 Simulations of cellular axial strain amplification within the chondrocyte via	

a representative point (Figure 3.2) comparing cases of normal PCM and ECM and OA exclusive to the PCM, for the loading frequencies: (a) $f = 0.01$ Hz, (b) $f = 0.05$ Hz, (c) $f = 0.05$ Hz and (d) $f = 0.1$ Hz.....	38
Figure 3.14 Simulations of cellular axial strain amplification within the chondrocyte via a representative point (Figure 3.2) comparing cases of normal PCM & ECM and OA PCM & ECM, for the loading frequencies: (a) $f = 0.01$ Hz, (b) $f = 0.02$ Hz, (c) $f = 0.05$ Hz and (d) $f = 0.1$ Hz.....	39
Figure 4.1 An extension of the boundary Γ around the point P	46
Figure 4.2 Coordinate representations of a point P in the plane $\theta = 0$ and the point Q in the axisymmetric boundary integral formulation.	48
Figure 4.3 Local geometry to calculate C_{ij}	51
Figure 4.4 A three-zone domain for a BEM model of coupled cell-PCM-ECM deformation in articular cartilage.....	52
Figure 4.5 A three node isoparametric quadratic boundary element with local coordinate ξ	54
Figure 4.6 A strongly singular point P located between two boundary elements Γ_b and Γ_a on a boundary element mesh.....	59
Figure 5.1 Verification of BEM model for plane strain with $\nu = 0.3$ and $E = 1000$ Pa shown for (a) displacement, (b) radial traction, and (c) axial traction comparing BEM model solutions (circles) to the analytical solution (solid line).....	66
Figure 5.2 Verification of BEM model for plane stress with $\nu = 0.3$ and $E = 1000$ Pa shown for (a) displacement, (b) radial traction, and (c) axial traction comparing BEM model solutions (circles) to the analytical solution (solid line).....	67
Figure 5.3 Diagram of unconfined compression test on a cylindrical biphasic sample. .	68
Figure 5.4 Verification of BEM model for unconfined compression with $\nu = 0.3$ and $E = 1000$ Pa shown for (a) displacement, (b) radial traction, and (c) axial traction comparing BEM solutions (circles) to the analytical solution (solid line).	69
Figure 5.5 Verification of the three-zone BEM model for plane strain with $\nu_{ECM} = \nu_{PCM} = \nu_{cell} = 0.2$ and $E_{ECM} = E_{PCM} = E_{cell} = 2000$ Pa shown for (a) displacement on cell-PCM and PCM-ECM interfaces, (b) radial traction on PCM-ECM interface, (c) axial traction on PCM-ECM interface comparing BEM model solutions (circles) to the analytical solution (solid line).	71

- Figure 5.6 Verification of the three-zone BEM model for plane stress with $\nu_{ECM} = \nu_{PCM} = \nu_{cell} = 0.2$ and $E_{ECM} = E_{PCM} = E_{cell} = 2000\text{Pa}$ shown for (a) displacement on cell-PCM and PCM-ECM interfaces, (b) radial traction on PCM-ECM interface, (c) axial traction on PCM-ECM interface comparing BEM solutions (circles) to the analytical solution (solid line). 72
- Figure 5.7 Verification of the three-zone BEM model for unconfined compression test with $\nu_{ECM} = \nu_{PCM} = \nu_{cell} = 0.2$ and $E_{ECM} = E_{PCM} = E_{cell} = 2000\text{Pa}$ shown for (a) displacement on cell-PCM and PCM-ECM interfaces, (b) radial traction on PCM-ECM interface, (c) axial traction on PCM-ECM interface comparing BEM solutions (circles) to the analytical solution (solid line). 73
- Figure 5.8 Verification of three-zone BEM model solutions for unconfined compression shown for (a) displacement on cell-PCM and PCM-ECM interfaces and (b) magnified figure of displacement comparing BEM solutions (open circles) to finite element solutions (solid circle). 74
- Figure 5.9 (a) Fluorescence confocal images of cartilage tissue explant and deformed chondron shapes in (b) superficial (c) middle, and (d) deep zones [30] (Reprinted from Journal of Biomechanics, 40/12, Jae Bong Choi, Inchan Youn, Li Cao, Holly A. Leddy, Christopher L. Gilchrist, Lori A. Setton and Farshid Guilak, Zonal changes in the three-dimensional morphology of the chondron under compression: The relationship among cellular, pericellular, and extracellular deformation in articular cartilage, 2596-2603., Copyright (2007), with permission from Elsevier.). 76
- Figure 5.10 Representation of the Nelder-Mead simplex method in 2 dimensions where solid circles indicate new simplex for (a) Expansion, (b) Reflection, (c) Contraction from reflection, (d) Contraction from the worst point and (e) Shrinkage toward to the best point $P_{(1)}$ 78
- Figure 5.11 Illustration of the three-zone BEM model for simulation of chondron deformation in unconfined compression. The analytical solution (5.3-5.4) was prescribed on the outer (ECM) boundary. 81
- Figure 5.12 Generation of data points on the chondron boundary by parameterization of the ellipsoid as $(r, z) = \left(\frac{w_d}{2} \sin \theta, -\frac{h_d}{2} \cos \theta\right)$. The centers of the ellipses in the BEM simulation of the deformed chondrons were aligned to the corresponding centers in the experimental data. 82
- Figure 5.13 Comparisons of the chondron shape between the optimal BEM model prediction (circles) with estimated E_{PCM} and the experimental data (solid line) in the case of one parameter estimation: (a) $\hat{E}_{PCM} = 44.375 \text{ kPa}$ from Table 5.3 and (b) $\hat{E}_{PCM} = 118.28 \text{ kPa}$ from Table 5.4. 84
- Figure 5.14 Comparisons of the chondron shape between the optimal BEM model predic-

tion (circle) with estimated E_{PCM} and ν_{PCM} and the experimental data (solid line) in the case of two parameter estimation: (a) $\hat{E}_{PCM} = 47.58$ kPa and $\hat{\nu}_{PCM} = 0.166$ from Table 5.5 and (b) $\hat{E}_{PCM} = 125.30$ kPa and $\hat{\nu}_{PCM} = 0.003$ from Table 5.6. .. 85

Figure 5.15 Comparisons of the deformed chondron and cell shapes between the optimal BEM model prediction (circles), with estimated values of E_{PCM} and ν_{PCM} , and the experimental data (solid line) based on the cost function (5.8): (a) $\hat{E}_{PCM} = 53.4$ kPa and $\hat{\nu}_{PCM} = 0.353$ from Table 5.7 and (b) $\hat{E}_{PCM} = 84.9$ kPa and $\hat{\nu}_{PCM} = 0.386$ from Table 5.8. 87

Chapter 1

Introduction and Background

Articular cartilage is the connective tissue that lines the surface of bones in diarthroidal joints of the hips, shoulders, and knees (Figure 1.1(a)). Cartilage is a highly hydrated soft biological tissue and serves as a low-friction, load-bearing material that facilitates joint motion [74]. Articular cartilage is comprised primarily of interstitial water (roughly 80% by volume) that saturates a solid extracellular matrix (ECM). The biomechanical properties and resiliency of articular cartilage are attributed to the unique structure and composition of its ECM. The ECM is comprised of a cross-linked network of type-II collagen fibers and proteoglycan macromolecules that have a net negative charge [69]. Structural degradation of cartilage ECM leads osteoarthritis (OA), a painful condition that is predominantly associated with aging. Under deformation, the biomechanical and biophysical environment within articular cartilage results from a complex combination of mechanisms such as matrix deformation, fluid pressurization, diffusive fluid-solid drag and ionic effects.

Multiphasic continuum mixture theories have been widely employed to model the biomechanics of articular cartilage, with the two most common approaches being biphasic (fluid-solid) models [73] and triphasic (fluid-solid-ion) models [41, 59]. The models developed in this dissertation are based on the biphasic theory and, as such, ionic effects are neglected. Experiments associated with biphasic modeling are conducted by saturating the tissue in isotonic solution, which mimics the osmolarity of synovial fluid, e.g. $\approx 0.15\text{M}$ NaCl. Biphasic models of articular cartilage capture fundamental aspects of the tissue's functional capacity due to load-partitioning and dissipation mechanisms that include elastic and viscoelastic deformation, pressurization of the interstitial fluid, and Darcy-like drag as fluid

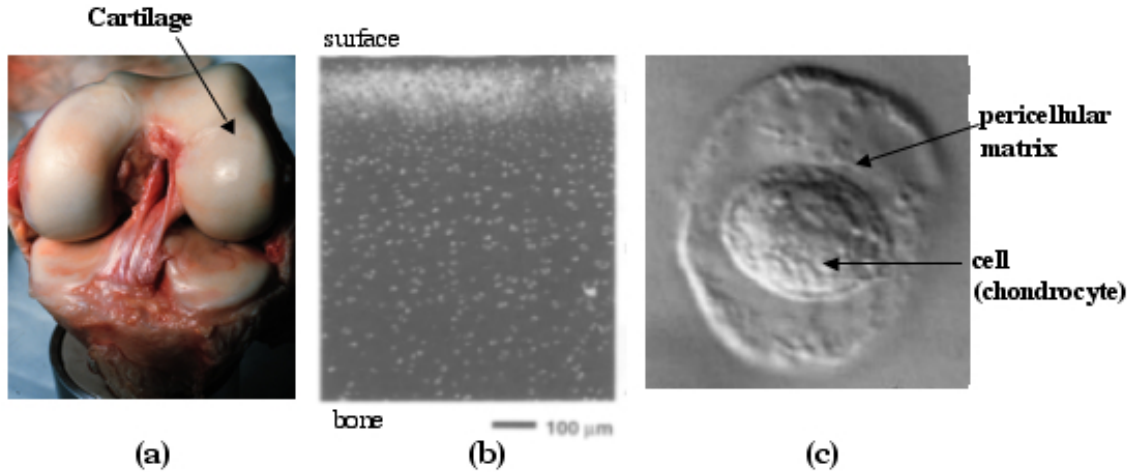


Figure 1.1: (a) Articular cartilage in a knee joint (b) A layer of articular cartilage showing presence of cells (chondrocytes) (Reprinted from *Osteoarthritis and Cartilage*, 2/2, Farshid Guilak, B. Christoph Meyer, Anthony Ratcliffe and Van C. Mow, The effects of matrix compression on proteoglycan metabolism in articular cartilage explants, 91-101., Copyright (1994), with permission from Elsevier.). (c) An isolated chondron (Reprinted from *Osteoarthritis and Cartilage*, 7/1, Farshid Guilak, Wendy R. Jones, H. Ping Ting-Beall and Greta M. Lee, The deformation behavior and mechanical properties of chondrocytes in articular cartilage, 57-70., Copyright (1999), with permission from Elsevier.).

flows past the solid phase of the ECM.

The biological nature of articular cartilage is apparent from the presence of a single population of specialized cells called chondrocytes. These cells are sparsely dispersed within the ECM and occupy between 1-10% of the tissue volume [96]. Chondrocytes are responsible for maintenance and repair of the ECM components [72]. Since cartilage is avascular and aneural, metabolic activities of the chondrocytes are highly dependent on their local biophysical and biomechanical environment. Thus, mathematical models of the local environment of the chondrocyte can contribute to understanding relationships between local physical variables and alterations in the physiological response of the tissue.

Within the ECM, chondrocytes are surrounded, individually or in groups, by a distinct region of ECM called the pericellular matrix (PCM). Together, the unit consisting of the chondrocyte and its surrounding PCM has been termed a chondron [81]. The PCM is known to have distinct mechanical properties as compared to cartilage ECM. Specifically, the presence of type-VI collagen in cartilage is exclusive to the PCM, and the PCM

also has a high proteoglycan concentration relative to the ECM. In the presence of OA, chondron size is enlarged in conjunction with an increase in cell proliferation [62]. In vitro micropipette aspiration studies of chondrons isolated from human and canine tissue indicate that the PCM is several orders of magnitude stiffer than the chondrocyte in the middle and deep zones [4, 6, 45]. Several of these studies also demonstrated that PCM elastic and biphasic mechanical properties exhibit significant alterations in the presence of OA [4, 6]. These studies suggest that the PCM plays a critical biomechanical role in regulating cell-matrix interactions in articular cartilage [6]. The PCM is believed to provide a protective layer around the cell since it is much stiffer and denser than chondrocyte. Since all mechanical signals are transmitted via the ECM to the chondron and, in turn, via the PCM to chondrocyte, the PCM is also hypothesized to play a significant role in mechanical signal transduction from the macroscopic scale of the tissue to the microscopic scale of the chondrocytes.

Models describing biomechanics in the local environment of the chondrocyte typically examine the hypothesized dual role of the PCM as a protective layer and a mechanical transducer around the cell. However, to date, very few studies have considered the development of such models. Guilak and Mow [47] developed a multiscale computational finite element model of biphasic cell-matrix interactions that incorporated the structure and properties of chondrocytes, the PCM and the ECM. In their investigation, the presence of the PCM strongly influenced the micromechanical environment of the chondrocyte under loading conditions of unconfined compressive stress relaxation. Haider [49] developed a model of dynamic biphasic interactions within a chondron, but ECM effects were neglected and the model assumed exclusively radial deformation.

These models involve internal interfaces, at the cell-PCM and PCM-ECM boundaries, with complex interactions between interstitial fluid and moving elastic solid constituents. Mathematically, these problems can be viewed as interface problems, which usually lead to differential equations with discontinuous or non-smooth solutions across interfaces. Typically, interface problems have one or more of the following properties. (a) The coefficients of the differential equations may be discontinuous across the interface. (b) The solution and the derivatives may be discontinuous. (c) There may be discontinuous or singular sources along the interface. (d) The interfaces are moving. (e) There may be more than one interface. The properties of our interest in this study are (a), (b) and (e).

Many numerical methods for interface problems have been developed and an excellent review can be found in [68]. As mentioned in [68], there are several efficient numerical methods for interface problems: the immersed boundary method, the ghost fluid method, the finite element method using body-fitted grid, the immersed interface method, the level set method, the immersed finite element method, and the boundary element method.

The immersed boundary method [71, 78, 79, 85] was originally developed by Peskin to model blood flow in the heart. The method is a standard numerical method for interface problems that involves prescription of singular forces along interfaces. The ghost fluid method was first presented by Fedkiw et al. in [38]. This method is particularly useful for a sharp interface and has been applied to multiphase incompressible flow. The finite element method has been widely used in solving structural, mechanical, heat transfer, and fluid dynamics problems [10, 15, 29, 36, 64, 101, 111]. The finite element method has the advantage of a rigorous theoretical framework, conforming elements along interfaces and many optimized commercial implementations. Thus, finite element methods have been applied to many interface problems. The immersed interface method developed by LeVeque and Li [63, 67] has been applied to many problems arising from elliptic, parabolic, hyperbolic and mixed type equations, with fixed or moving interface problems and is often more accurate than Peskin's immersed boundary method. The level set method [76, 89] has been successfully used to treat a number of moving boundary/interface problems [27]. In general, the immersed boundary, ghost fluid, immersed interface and level set methods employ rectangular grids, while the finite element method uses conforming elements. An exception is the immersed finite element method, first presented by Li in [66]. Both conforming and non-conforming finite element spaces can be used and the method is second order accurate. The basic idea is to form a partition which is independent of interface so that partitions with simple and efficient structures can be used to solve an interface problem with a complex interface. The boundary element method uses integral formulation of the governing partial differential equations, which can be written exclusively in terms of integrals along the domain boundary and internal interfaces. Since the method requires discretization exclusively on the boundary and interfaces, it is often more efficient than other methods. The fact that the boundary element method employs fundamental solutions to the governing equations accounts for another advantage, which is the improved accuracy. The method has been applied in many areas of structural mechanics, fluid dynamics, acoustics, electromagnetics,

and fracture mechanics [16, 17, 18, 21, 33, 51, 82, 113], but it is limited to linear problems.

In this study, the natural variables (displacement and traction) are continuous along interfaces at the cell-PCM and PCM-ECM boundaries. Hence, this interface problem can be efficiently solved by numerical methods that use conforming finite element meshes or direct discretization of interfaces as in the boundary element method. These two numerical methods were considered in analyzing the biomechanical cell-matrix interactions in this dissertation.

Overall, results for computational modeling of mechanical cell-matrix interactions in cartilage are strongly dependent on the assumed mechanical properties of the ECM, PCM and chondrocyte. Mechanical properties of ECM and chondrocyte are well established from several *in vitro* mechanical tests performed on cartilage explants [12, 73] and isolated cells, respectively [55, 103]. Mechanical properties of the PCM have been measured via micropipette testing of chondrons isolated from varying depths of normal and OA cartilage by comparison to elastic [4] and biphasic [6] theoretical and numerical solutions. Recently, *in situ* changes in three-dimensional morphology of the chondron within the ECM of a cartilage explant under equilibrium unconfined compression were quantified using a novel fluorescence imaging technique based on confocal microscopy and immunolabeling of type VI collagen [30].

In this dissertation, two computational models were developed to analyze the multiphasic micromechanical environment of chondrocytes in articular cartilage. In the first, a penalty finite element model of biphasic cell-matrix interactions was developed as an extension of [91]. A custom implementation of the finite element formulation was conducted using the software package *Comsol Multiphysics*. The resulting computational model was employed to characterize the microscale stress-strain environment in an articular cartilage explant subjected to dynamic confined compressive loading. The biphasic model of articular cartilage was used to describe tissue deformation resulting from a combination of fluid and solid phase load-partitioning and dissipation mechanisms. Solid phase deformation was idealized to be linear, isotropic and in the range of infinitesimal strain. Since many configurations in cartilage mechanics are assumed to have axial symmetry due to the extraction of cartilage explants as cylindrical plugs, and cells and chondrons can be approximated as spheres or ellipsoids, models were developed under the assumption of axisymmetric geometry.

In the second component of this dissertation, an axisymmetric elastic boundary element method was developed to model *in situ* chondron deformation under equilibrated deformation of a cartilage explant subjected to unconfined compressive loading. In the case of the linear biphasic model at equilibrium, the governing equations reduce to those of linear elasticity theory, which are a system of linear, elliptic partial differential equations. For such equations, the boundary element method can be employed as an alternative to finite difference or finite element methods. Boundary element methods are based on the use of analytical fundamental solutions of the governing partial differential equations. These methods are particularly efficient when quantities of interest reside, exclusively, on the domain boundary or internal interfaces, because the method relies on discretization of only surface (boundary or interface) quantities. In the context of cartilage mechanics, a previous study developed an axisymmetric boundary element model for assessing elastic mechanics for single cells under micropipette aspiration [50]. In this part of the dissertation, a multiscale extension of a previous model [50] was developed, via a custom implementation in compiled C, for simulation of *in situ* chondron deformation in states of mechanical equilibrium. This computational model of the forward problem was then integrated to solve the inverse problem of determining elastic properties via analysis of data based on the novel confocal fluorescence imaging technique developed in [30].

In chapter 2, the linear biphasic theory, multiscale modeling, finite element formulation and implementation as a finite element method are described. In chapter 3, the accuracy of the numerical method developed in chapter 2 is evaluated and application to modeling dynamic biphasic cell-matrix interactions under uniaxial confined compression is analyzed. Chapter 4 describes the elastic boundary integral formulation and its specialization to the case of axisymmetric geometry and domains with internal interfaces. Detailed numerical methods for discretization and implementation of the associated axisymmetric boundary element method are also presented. In chapter 5, the accuracy of the boundary element model developed in chapter 4 is evaluated and the model is applied to the inverse problem for parameter estimation of PCM elastic properties based on experimental data from [30].

Chapter 2

Finite Element Modeling of Microscale Biphasic Mechanics in Articular Cartilage under Dynamic Loading

Many experimental groups have studied the effects of dynamic loading on the biosynthetic activity of chondrocytes in articular cartilage. Some have examined the effects on cell metabolic activity in cartilage explants [19, 24, 65, 77, 80, 86, 87, 94, 102], tissue-engineered cartilage [31, 32, 34, 54, 60, 61, 70, 106, 108] and chondrocyte cell cultures [9, 107]. Others have studied the effects on chondrocyte differentiation in cell-seeded scaffolds [37]. In vitro studies of cartilage explants have suggested that cyclic loading can increase or suppress glycosaminoglycan (GAG) synthesis [65], while static loading inhibits GAG synthesis. Biosynthetic activities of the chondrocyte have been shown to be dependent primarily on mechanical factors such as the frequency [24, 65, 77, 86, 87, 95] and magnitude of dynamic load [80, 86, 95, 102], duration of load application [87, 95], as well as the radial position in unconfined cylindrical explants [24]. These studies indicate that macroscopic dynamic mechanical loading of articular cartilage strongly influences regulatory pathways by which chondrocytes respond to their surroundings.

Under dynamic compression, the diffusive drag force as interstitial fluid flows past

cartilage ECM is an important contributor to the apparent viscoelastic response of the tissue. This fundamental biomechanical mechanism can be quantified within the framework of biphasic theory [73], which models articular cartilage as an incompressible continuum mixture of fluid and solid phases. Macroscopic loading on the millimeter-scale of a cartilage layer or explant induces nonuniform deformation [25, 30, 48] on the micron scale of the chondrocyte, as well as stress, strain, pressure, and flow fields that can be simulated via biphasic models. Such models have the potential to aid in delineation of specific components of the biphasic cellular microenvironment that are involved in cell metabolic regulatory responses to mechanical load. Previously, theoretical models using linear biphasic theory were developed for dynamic confined compressive and unconfined compressive loading of cartilage extracellular matrix [98, 100]. While these theoretical solutions can be used to quantify the macroscopic mechanical environment of articular cartilage, they neglect the presence of the chondron and its potential influence on biphasic mechanics at the microscale. A more detailed description of mechanisms by which macroscopic mechanical signals translate into microscopic signals is required.

A detailed description of biphasic mechanics in the local cellular environment of cartilage necessitates a multiscale extension of macroscopic homogeneous models to include inhomogeneous inclusions representing the chondrocyte and its encapsulating pericellular matrix (PCM). Previously, multiscale finite element models have been developed and applied to simulate biphasic cell-matrix interactions for spheroidal inclusions representing chondrocytes [112], a chondron embedded in cartilage ECM under steady state loading [5], and transient stress relaxation in unconfined compression [47]. In these cases, the inclusion of a biphasic region representing the PCM that surrounds the chondrocyte strongly influenced the mechanical environment of the cell. In this chapter, a biphasic model of cell-matrix interactions is developed under cyclic loading conditions. The resulting model can aid in correlation of fluid and solid mechanics in the cellular microenvironment with chondrocyte biosynthetic activity in tissue explants and tissue-engineered constructs.

2.1 Biphasic Theory

The biphasic mixture theory [73] was developed to model the effects of interstitial fluid on the mechanical properties of articular cartilage. In the biphasic theory, articular

cartilage is modeled as a continuum mixture of two phases, a solid and a fluid phase. The solid phase consists primarily of collagen fibers and proteoglycan macromolecules. The fluid phase is comprised of interstitial fluid and dissolved ions. The overall mechanical behavior of cartilage depends not only on the solid matrix deformation, but also on movement of fluid in and out of the tissue pores during the deformation. Upon loading, the interstitial fluid pressure builds up within the tissue instantaneously, and then the fluid is redistributed within the matrix as the solid matrix exhibits deformation. Since there is a large diffusive drag between fluid and solid, energy is dissipated as the fluid is redistributed resulting in an apparent viscoelastic response. Since fluid plays a key role in the load transfer in these tissues, it follows that the stress-strain behavior of the tissue will be time dependent. In this section, the fundamentals of biphasic theory, as a constitutive model for a fluid saturated deformable solid, are discussed.

2.1.1 Biphasic Governing Equations

The biphasic theory idealizes articular cartilage as a mixture consisting of superimposed fluid and solid phase continua. The inertial terms in the momentum balance equations are assumed to be negligible as the tissue has a high elastic stiffness and diffusive drag, and since loading frequencies are relatively low (< 10 Hz). The mixture is assumed to be intrinsically incompressible and saturated.

Under these assumptions, the governing equations for the biphasic continuum mixture model of cartilage mechanics are

$$\nabla \cdot \sigma^s + \Pi = \mathbf{0}, \quad (2.1)$$

$$\nabla \cdot \sigma^f - \Pi = \mathbf{0}, \quad (2.2)$$

$$\nabla \cdot (\phi \partial_t \mathbf{u} + (1 - \phi) \mathbf{v}) = 0. \quad (2.3)$$

Equations (2.1) and (2.2) are momentum balance equations for the solid and fluid phases, respectively. σ^s and σ^f are partial Cauchy stress tensors for the solid and fluid phases, respectively, and Π is the fluid-solid diffusive drag force per unit volume as fluid flows past solid in the mixture. The intrinsic incompressibility condition (2.3) is written in terms of solid displacement \mathbf{u} , fluid velocity \mathbf{v} , and the solid volume fraction ϕ .

Under the assumption of a linear isotropic solid phase, an inviscid fluid phase, and diffusive fluid-solid drag with constant diffusive drag coefficient K , the constitutive relations are

$$\sigma^s = -\phi p \mathbf{I} + \lambda_s \text{tr}(\mathbf{e}) \mathbf{I} + 2\mu_s \mathbf{e}, \quad \sigma^f = -(1 - \phi)p \mathbf{I}, \quad \Pi = K(\mathbf{v} - \partial_t \mathbf{u}), \quad (2.4)$$

where \mathbf{I} is the identity tensor, p is a pore pressure, $\mathbf{e} \left(= \frac{\nabla \mathbf{u} + \nabla \mathbf{u}^T}{2} \right)$ is the solid phase infinitesimal strain, λ_s, μ_s are Lamé coefficients, and the diffusive drag coefficient K is defined in terms of constant hydraulic permeability κ and solid volume fraction ϕ , as $K = \frac{(1-\phi)^2}{\kappa}$.

2.1.2 Biphasic Governing Equations at Equilibrium

When the motion of fluid through the pores of the deforming biphasic mixture ceases, the mixture reaches its equilibrium. When cartilage is in this “drained” state of biphasic equilibrium, the linear biphasic theory reduces to the equations of linear isotropic elasticity. Thus, the governing equations can be reduced to

$$\nabla \cdot \sigma = \mathbf{0}, \quad \sigma = \lambda_s \text{tr}(\mathbf{e}) \mathbf{I} + 2\mu_s \mathbf{e}, \quad 2\mathbf{e} = \nabla \mathbf{u} + \nabla \mathbf{u}^T. \quad (2.5)$$

2.2 Multiscale Model

To model the microscopic environment in articular cartilage, the tissue is viewed on two different scales. At the macroscopic level, cartilage ($\sim 1\text{-}5$ mm thick) is a multiphasic continuum mixture comprised of interstitial fluid that saturates a solid extracellular matrix. Since chondrocytes occupy roughly 1-10% of the tissue volume and the PCM is a narrow tissue surrounding chondrocytes, a homogeneous continuum mixture model is a first approximation for modeling mechanisms of deformation of cartilage ECM on the macroscopic scale. However, to study mechanical interactions between the ECM, the PCM and the chondrocyte, it is necessary to include the other characteristic (micron) length scale in an extended model. In the context of cartilage mechanics, a previous study [47] developed a multiscale model to simulate microscale response under biphasic stress relaxation of a cylindrical layer in unconfined compression via the finite element method. In this study, a similar multiscale modeling approach is used to simulate microscale effects of macroscopic dynamic loading. Specifically, the microscale environment of a single chondrocyte is modeled as a three-zone region consisting of a spherical cell with a surrounding pericellular layer that is

embedded in a cylindrical ECM, as depicted in Figure 2.1. Macroscopic cartilage deformation is modeled via an analytical solution for dynamic loading of a linear biphasic cylinder in confined compression [100]. This solution is employed to formulate far field boundary conditions for microscopic deformation. In cartilage, this is a reasonable assumption since cells occupy roughly 1-10% of the overall tissue volume, and are sparsely arranged in the ECM.

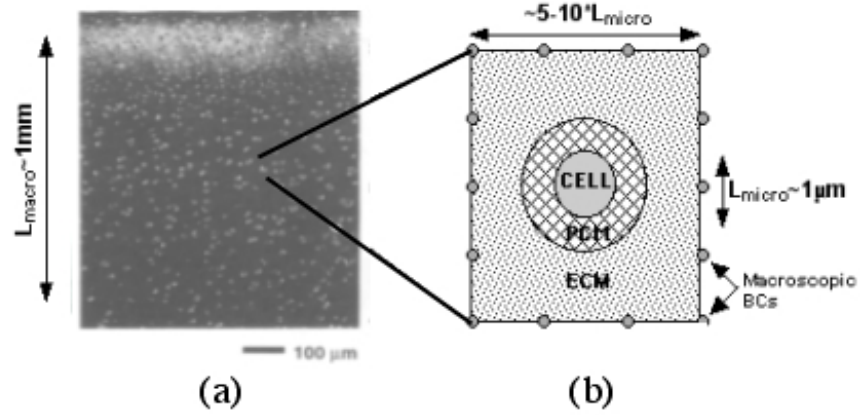


Figure 2.1: Modeling the micromechanical environment in articular cartilage. (a) A layer of articular cartilage (Reprinted from *Osteoarthritis and Cartilage*, 2/2, Farshid Guilak, B. Christoph Meyer, Anthony Ratcliffe and Van C. Mow, The effects of matrix compression on proteoglycan metabolism in articular cartilage explants, 91-101., Copyright (1994), with permission from Elsevier.). (b) Microscale domain with a single cell, its encapsulating pericellular matrix (PCM) and extracellular matrix (ECM).

2.2.1 Finite Element Modeling of Microscale Cartilage Deformation under Dynamic Loading

The finite element method (FEM) has been widely used in the numerical solution of partial differential equations. In particular, the FEM has been successfully employed to solve the governing equations of elasticity and structural mechanics in applications with complex geometries. In the context of cartilage mechanics, the FEM has been widely used

to model small strain [40, 91, 92, 93], large strain [7, 8, 26, 46, 90, 99, 110] and contact [35, 104, 105, 109] problems. Multiscale FEM models of cell-matrix interactions [5, 47] have also been developed in recent years.

Motivated by [47], a multiscale finite element method is developed for the case of axisymmetric geometries. In general, four steps are taken to develop a FEM model. First, a weak integral formulation is derived via multiplication of the governing equations by weighting functions that satisfy essential boundary conditions, and applying the Divergence Theorem to integrate by parts. Second, a geometric mesh is generated with an associated set of basis functions $\{\psi_j\}_{j=1}^N$. Third, the solution is approximated using a linear combination of the basis functions, i.e., $u_N = \sum_{j=1}^N \alpha_j \psi_j$ where $\{\alpha_j\}_{j=1}^N$ are nodal unknowns. Lastly, a linear system of equations for the unknowns is assembled and solved. In this study, the weak formulation is derived by adapting the formulation in [91], and developing a new implementation in the *Comsol Multiphysics* software environment. This choice is based on *Comsol Multiphysics*'s capability to handle custom weak formulations in conjunction with robust numerical solvers, a variety of element types, versatile mesh generation and rapid solution post-processing and visualization [1, 2].

2.2.2 Mixed Penalty Weak Formulation

The mixed penalty method replaces the continuity equation (2.3) with its penalty form,

$$\nabla \cdot (\phi \partial_t \mathbf{u} + (1 - \phi) \mathbf{v}) + \frac{p}{\beta} = 0, \quad (2.6)$$

where β is a user specified penalty parameter, chosen to be several orders of magnitude larger than typical pressures in the tissue. Note that in the limit of $\beta \rightarrow 0$, the original continuity equation is obtained from equation (2.6).

Adapted from [91], the weighted residual form used in our implementation can be obtained in the following way. Let $\mathbf{w}^{s,f}$ be admissible weighting functions for the solid and fluid phases. Weighting functions $\mathbf{w}^{s,f}$ must be continuous and satisfy homogeneous versions of the essential boundary conditions. A scalar weighting function w^c is also introduced to incorporate (2.6) into the weighted residual formulation. The resulting weighted residual

formulation is

$$\begin{aligned} & \int_{\Omega} \mathbf{w}^s \cdot \nabla \cdot \sigma^s d\Omega + \int_{\Omega} \mathbf{w}^s \cdot \Pi d\Omega + \int_{\Gamma} \mathbf{w}^s \cdot [\hat{\mathbf{t}}_E^s - \mathbf{t}_E^s] d\Gamma + \int_{\Gamma} \mathbf{w}^s \cdot \phi[p - \hat{p}] \mathbf{n} d\Gamma \\ & + \int_{\Omega} \mathbf{w}^f \cdot \nabla \cdot \sigma^f d\Omega - \int_{\Omega} \mathbf{w}^f \cdot \Pi d\Omega + \int_{\Omega} w^c \cdot \left[\nabla \cdot ((1 - \phi)\mathbf{v} + \phi \partial_t \mathbf{u}) + \frac{p}{\beta} \right] d\Omega = 0, \end{aligned} \quad (2.7)$$

where Ω is a biphasic domain with unit outward normal \mathbf{n} on the boundary Γ , and $\hat{\mathbf{t}}_E^s$ and \hat{p} are prescribed values of the elastic part of the solid phase traction and pore pressure on the boundary, respectively. The divergence theorem is applied to the first integral in (2.7). After substitution of the constitutive equations (2.4), the resulting weak formulation of the weighted residual form is

$$\begin{aligned} & - \int_{\Omega} \nabla \mathbf{w}^s : (-\phi p \mathbf{I} + \lambda_s \text{tr}(\mathbf{e}) \mathbf{I} + 2\mu_s \mathbf{e}) d\Omega + \int_{\Omega} \mathbf{w}^s \cdot K(\mathbf{v} - \partial_t \mathbf{u}) d\Omega + \int_{\Gamma} \mathbf{w}^s \cdot \hat{\mathbf{t}}_E^s d\Gamma \\ & + \int_{\Omega} \mathbf{w}^f \cdot \nabla(-(1 - \phi)) p \mathbf{I} d\Omega - \int_{\Omega} \mathbf{w}^f \cdot K(\mathbf{v} - \partial_t \mathbf{u}) d\Omega + \int_{\Gamma} \mathbf{w}^s \cdot \phi(-\hat{p}) \mathbf{n} d\Gamma \\ & + \int_{\Omega} w^c \cdot \left[\nabla \cdot ((1 - \phi)\mathbf{v} + \phi \partial_t \mathbf{u}) + \frac{p}{\beta} \right] d\Omega = 0, \end{aligned} \quad (2.8)$$

where $\mathbf{A} : \mathbf{B} = \text{tr}(\mathbf{A}\mathbf{B}^T)$.

2.2.3 Axisymmetric Specialization of Weak Formulation

To develop an axisymmetric specialization of (2.8), solid strain and stress tensors need to be obtained in a cylindrical coordinate system. In cylindrical coordinates, the primary dependent variables can be written as $\mathbf{u} \equiv (u_r, u_\varphi, u_z)$, $\mathbf{v} \equiv (v_r, v_\varphi, v_z)$ and $p \equiv p(z)$. In the implementation, fluid displacement $\mathbf{u}^f \equiv (u_r^f, u_\varphi^f, u_z^f)$ is used instead of velocity and solid displacement is denoted by $\mathbf{u} \equiv \mathbf{u}^s \equiv (u_r^s, u_\varphi^s, u_z^s)$. Under the assumption of axial symmetry, the component of \mathbf{u}^s in the φ direction together with the corresponding strain and stress components are assumed to be zero. The resulting strain and solid phase stress tensors have the respective representations

$$\mathbf{e} = \begin{pmatrix} \frac{\partial u_r^s}{\partial r} & 0 & \frac{1}{2} \left(\frac{\partial u_r^s}{\partial z} + \frac{\partial u_z^s}{\partial r} \right) \\ 0 & \frac{u_r^s}{r} & 0 \\ \frac{1}{2} \left(\frac{\partial u_r^s}{\partial z} + \frac{\partial u_z^s}{\partial r} \right) & 0 & \frac{\partial u_z^s}{\partial z} \end{pmatrix} \quad (2.9)$$

$$\sigma^s = \begin{pmatrix} \sigma_{rr}^s & 0 & \sigma_{rz}^s \\ 0 & \sigma_{\varphi\varphi}^s & 0 \\ \sigma_{zr}^s & 0 & \sigma_{zz}^s \end{pmatrix}. \quad (2.10)$$

Using the constitutive equation (2.4), components of the solid phase stress tensor can be written as

$$\sigma_{rr}^s = (\lambda_s + 2\mu_s) \frac{\partial u_r^s}{\partial r} + \lambda_s \frac{u_r^s}{r} + \lambda_s \frac{\partial u_z^s}{\partial z} - \phi p, \quad (2.11)$$

$$(2.12)$$

$$\sigma_{\varphi\varphi}^s = \lambda_s \frac{\partial u_r^s}{\partial r} + (\lambda_s + 2\mu_s) \frac{u_r^s}{r} + \lambda_s \frac{\partial u_z^s}{\partial z} - \phi p, \quad (2.13)$$

$$(2.14)$$

$$\sigma_{zz}^s = \lambda_s \frac{\partial u_r^s}{\partial r} + \lambda_s \frac{u_r^s}{r} + (\lambda_s + 2\mu_s) \frac{\partial u_z^s}{\partial z} - \phi p, \quad (2.15)$$

$$(2.16)$$

$$\sigma_{rz}^s = \sigma_{zr}^s = \mu_s \left(\frac{\partial u_r^s}{\partial z} + \frac{\partial u_z^s}{\partial r} \right). \quad (2.17)$$

In cylindrical coordinates, the weak formulation can be written explicitly as

$$\begin{aligned} & \int_{\Omega} 2\pi \left[\frac{\partial w_r^s}{\partial r} \sigma_{rr}^s + \frac{\partial w_z^s}{\partial r} \sigma_{zr}^s + \frac{1}{r} w_r^s \sigma_{\varphi\varphi}^s + \frac{\partial w_r^s}{\partial z} \sigma_{rz}^s + \frac{\partial w_z^s}{\partial z} \sigma_{zz}^s \right] r dr dz + \int_{\Gamma} \mathbf{w}^s \cdot \hat{\mathbf{t}}_E^s dr dz \\ & + \int_{\Omega} 2\pi \left[w_r^s K \left(\frac{\partial u_r^f}{\partial t} - \frac{\partial u_r^s}{\partial t} \right) + w_z^s K \left(\frac{\partial u_r^f}{\partial t} - \frac{\partial u_r^s}{\partial t} \right) \right] r dr dz \\ & - (1 - \phi) \int_{\Omega} 2\pi \left[w_r^f \frac{\partial p}{\partial r} + w_z^f \frac{\partial p}{\partial z} \right] r dr dz + \int_{\Gamma} \mathbf{w}^s \cdot \phi(-\hat{p}) \mathbf{n} dr dz \\ & - \int_{\Omega} 2\pi \left[w_r^f K \left(\frac{\partial u_r^f}{\partial t} - \frac{\partial u_r^s}{\partial t} \right) + w_z^f K \left(\frac{\partial u_r^f}{\partial t} - \frac{\partial u_r^s}{\partial t} \right) \right] r dr dz \\ & + \int_{\Omega} 2\pi w_c \phi \left(\frac{1}{r} \frac{\partial}{\partial r} \left(r \frac{\partial u_r^s}{\partial t} \right) + \frac{\partial}{\partial z} \frac{\partial u_z^s}{\partial t} \right) r dr dz \\ & + \int_{\Omega} 2\pi w_c \left[(1 - \phi) \left(\frac{1}{r} \frac{\partial}{\partial r} \left(r \frac{\partial u_r^f}{\partial t} \right) + \frac{\partial}{\partial z} \frac{\partial u_z^f}{\partial t} \right) + \frac{p}{\beta} \right] r dr dz = 0. \end{aligned} \quad (2.18)$$

To avoid division by r in the first integral of (2.18), which gives rise to a singularity on the axis of symmetry ($r = 0$), a new dependent variable \bar{u}_r

$$\bar{u}_r = \frac{u_r^s}{r} \quad (2.19)$$

is introduced to replace the solid phase displacement u_r^s as a primary variable in the formulation. To obtain the final version of the axisymmetric weak formulation, equation (2.18) can be rewritten in terms of the new dependent variable \bar{u}_r as

$$\begin{aligned} & \int_{\Omega} 2\pi \frac{\partial w_r^s}{\partial r} \left((\lambda_s + 2\mu_s) r^2 \frac{\partial \bar{u}_r}{\partial r} + (\lambda_s + 2\mu_s) r \bar{u}_r + \lambda_s r \bar{u}_r + \lambda_s r \frac{\partial u_z^s}{\partial z} \right) dr dz \\ & + \int_{\Omega} 2\pi w_r^s \left(\lambda_s r \frac{\partial \bar{u}_r}{\partial r} + \lambda_s \bar{u}_r + (\lambda_s + 2\mu_s) \bar{u}_r + \lambda \frac{\partial u_z^s}{\partial z} \right) dr dz \\ & + \int_{\Omega} 2\pi \frac{\partial w_z^s}{\partial r} \left(\mu_s r \frac{\partial w_z^s}{\partial r} + \mu_s r^s \frac{\partial \bar{u}_r}{\partial s} \right) dr dz + \int_{\Gamma} \mathbf{w}^s \cdot \hat{\mathbf{t}}_E^s dr dz \\ & + \int_{\Omega} 2\pi \frac{\partial w_r^s}{\partial z} \left(\mu_s r \frac{\partial w_z^s}{\partial r} + \mu_s r^2 \frac{\partial \bar{u}_r}{\partial z} \right) dr dz \\ & + \int_{\Omega} 2\pi \frac{\partial w_z^s}{\partial z} \left(\lambda_s r^2 \frac{\partial \bar{u}_r}{\partial r} + 2\lambda_s r \bar{u}_r + (\lambda_s + 2\mu_s) r \frac{\partial w_z^s}{\partial z} \right) dr dz \\ & + \int_{\Omega} 2\pi \left[w_r^s K \left(\frac{\partial u_r^f}{\partial t} - \frac{\partial(r\bar{u}_r)}{\partial t} \right) + w_z^s K \left(\frac{\partial u_r^f}{\partial t} - \frac{\partial(r\bar{u}_r)}{\partial t} \right) \right] r dr dz \\ & - (1 - \phi) \int_{\Omega} 2\pi \left[w_r^f \frac{\partial p}{\partial r} + w_z^f \frac{\partial p}{\partial z} \right] r dr dz + \int_{\Gamma} \mathbf{w}^s \cdot \phi(-\hat{p}) \mathbf{n} dr dz \\ & - \int_{\Omega} 2\pi \left[w_r^f K \left(\frac{\partial u_r^f}{\partial t} - \frac{\partial(r\bar{u}_r)}{\partial t} \right) + w_z^f K \left(\frac{\partial u_r^f}{\partial t} - \frac{\partial(r\bar{u}_r)}{\partial t} \right) \right] r dr dz \\ & + \int_{\Omega} 2\pi w_c \phi \left(\frac{1}{r} \frac{\partial}{\partial r} \left(r \frac{\partial(r\bar{u}_r)}{\partial t} \right) + \frac{\partial}{\partial z} \frac{\partial u_z^s}{\partial t} \right) r dr dz \\ & + \int_{\Omega} 2\pi w_c \left[(1 - \phi) \left(\frac{1}{r} \frac{\partial}{\partial r} \left(r \frac{\partial u_r^f}{\partial t} \right) + \frac{\partial}{\partial z} \frac{\partial u_z^f}{\partial t} \right) + \frac{p}{\beta} \right] r dr dz = 0. \end{aligned} \quad (2.20)$$

2.2.4 Implementation of the Axisymmetric Weak Formulation

The axisymmetric weak formulation was implemented as a custom weak form in *Comsol Multiphysics*. Specifically, a 2D model was created using the option “*PDE/Modes /Weak Form, Subdomain/ Time-dependent analysis*” with 5 dependent variables corresponding to p , $\mathbf{u}^s = (\bar{u}_r, u_z^s)$, and $\mathbf{u}^f = (u_r^f, u_z^f)$. The resulting user interface has 5 component equations for the weak formulation of the weighted residual statement in which the domain integral and boundary integral terms in equation (2.18) are separately specified, as in [1]. For the time dependent terms, i.e., the third and the fifth integrals in (2.18), the “dweak” dialog box was used. To prescribe boundary conditions, the “Boundary Settings” dialog box was used.

A conforming triangular element space was considered as the domain space for the spatial part of the finite element solution. Via use of a conforming mesh, *Comsol Multiphysics* automatically enforces interface conditions, $[[\mathbf{u}^s]] = 0$, $[[p]] = 0$, $[[\lambda_s \text{tr}(\mathbf{e}) + 2\mu_s \mathbf{e}]] \cdot \mathbf{n} = 0$, $[[(1 - \phi) \frac{\partial \mathbf{u}^f}{\partial t}]] \cdot \mathbf{n} = 0$, where $[[\cdot]] \equiv (\cdot)_+ - (\cdot)_-$, since these conditions are either primary variables or naturally continuous flux quantities. Linear and quadratic triangular finite elements are depicted in Figure 2.2. A linear triangular element is characterized by three nodes, located at the three vertices of the triangle and a quadratic element can be obtained with six nodes located at the vertices and the edge midpoint of the triangle (Figure 2.2 (a),(b)). An example of a linear basis function is also depicted in Figure 2.2 (c).

Radial and axial displacements were approximated by Lagrange quadratic elements, and pressure was approximated by Lagrange linear elements. Lagrange elements

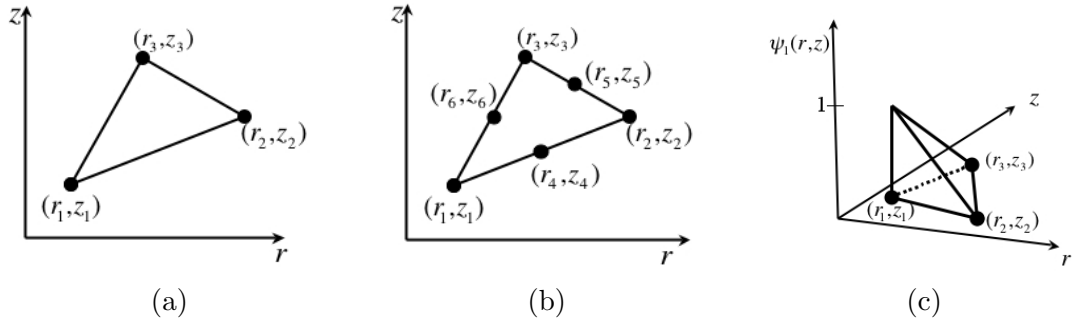


Figure 2.2: (a) A linear triangular element with local nodes, (b) a quadratic triangular element and (c) an example of a linear basis function $\psi_1(r_1, z_1)$.

are formed from basis functions $\{\psi_j\}$, which maintain important properties of Lagrange polynomials: (1) basis functions are C^0 continuous, (2) each function is one at the node with which it is associated and is zero at all other nodes (Figure 2.2 (c)), (3) each function is zero outside the element (i.e., it is zero almost everywhere). Linear basis functions $\{\psi_j^l\}$ exhibiting all of these properties in two dimensional space are

$$\psi_1^l(\xi, \eta) = 1 - \xi - \eta, \quad \psi_2^l(\xi, \eta) = \xi, \quad \psi_3^l(\xi, \eta) = \eta, \quad (2.21)$$

$$\xi = \frac{1}{2A}[(z_3 - z_1)(r - r_1) - (r_3 - r_1)(z - z_1)], \quad (2.22)$$

$$\eta = \frac{1}{2A}[-(z_2 - z_1)(r - r_1) + (r_2 - r_1)(z - z_1)], \quad (2.23)$$

$$2A = \det \begin{bmatrix} 1 & 1 & 1 \\ r_1 & r_2 & r_3 \\ z_1 & z_2 & z_3 \end{bmatrix}. \quad (2.24)$$

$$(2.25)$$

Quadratic Lagrangian basis functions are defined as

$$\begin{aligned} \psi_1(r, z) &= \psi_1^l(2\psi_1^l - 1), & \psi_4(r, z) &= \psi_1^l\psi_2^l, \\ \psi_2(r, z) &= \psi_2^l(2\psi_2^l - 1), & \psi_5(r, z) &= \psi_2^l\psi_3^l, \\ \psi_3(r, z) &= \psi_3^l(2\psi_3^l - 1), & \psi_6(r, z) &= \psi_3^l\psi_1^l, \end{aligned} \quad (2.26)$$

where node 4 is assumed to be midway between node 1 and node 2. Nodes 5 and 6 are also at the midpoint of their respective sides (Figure 2.2 (b)).

After mesh generation, the element interpolations

$$\begin{aligned} \bar{u}_r &= \sum_{j=1}^N (\bar{u}_r^s)_j \psi_j^s, & u_z^s &= \sum_{j=1}^N (u_z^s)_j \psi_j^s, \\ u_r^f &= \sum_{j=1}^N (u_r^f)_j \psi_j^f, & u_z^f &= \sum_{j=1}^N (u_z^f)_j \psi_j^f, \\ p &= \sum_{j=1}^N p_j \psi_j^p, \end{aligned} \quad (2.27)$$

were substituted into the weak formulation (2.18) automatically in *COMSOL*, where $(\bar{u}_r^s)_j$, $(u_z^s)_j$, $(u_r^f)_j$, $(u_z^f)_j$, and p_j are the solid nodal displacements, fluid nodal displacements, and nodal pressure for any element, respectively. Similarly, weighting functions can be discretized as

$$\begin{aligned} w_r^s &= \sum_{j=1}^N (w_r^s)_j \psi_j^s, & w_z^s &= \sum_{j=1}^N (w_z^s)_j \psi_j^s, \\ w_r^f &= \sum_{j=1}^N (w_r^f)_j \psi_j^f, & w_z^f &= \sum_{j=1}^N (w_z^f)_j \psi_j^f, \\ w_c &= \sum_{j=1}^N (w_c)_j \psi_j^p. \end{aligned} \quad (2.28)$$

These interpolations lead to a discretized system of first order linear ordinary differential equations $\mathbf{C} \frac{d\mathbf{X}}{dt} + \mathbf{K}\mathbf{X} = \mathbf{F}$, $\mathbf{X} = [\bar{u}_r, u_z^s, u_r^f, u_z^f, p]_{j=1, \dots, M}^T$ that are solved using the “Time dependent” solver option. This solver views the discretized equations as a differential-algebraic system and employs a version of the DASPK solver. This solver employs an implicit scheme that uses step size backward differentiation formulas as in [22] and [2]. At each time step, the spatial linear system is solved using the solver option “direct (UMFPACK)”, which employs the unsymmetric-pattern multifrontal method and direct LU factorization.

The numerical convergence of the custom model has been tested with mesh refinement and various penalty parameters β in equation (2.6). Results are shown in Chapter 3. Accuracy of the custom model was also verified by comparison to existing one dimensional dynamic radial deformation solutions for a layered biphasic sphere [49] at frequency 0.1Hz, and comparisons are also shown in Chapter 3.

2.2.5 Macroscale Modeling of Cartilage Deformation

Application of the computational model focuses on characterizing microscale biphasic mechanics in cartilage under dynamic loading in the *in vitro* confined compression test for a cylindrical cartilage explant. In this test, a cylindrical cartilage explant is constrained in a confining chamber and is subjected to a cyclic and exclusively compressive load via a rigid porous platen, as shown in Figure 2.3.

This configuration assumes axisymmetric deformation at the macroscale, and the macroscopic solution was used to formulate boundary conditions for a microscale, cell-PCM-ECM domain. Suh et al. [100] derived an analytical series solution of equations (2.1) - (2.4) for uniaxial cyclic confined compression of a linear biphasic layer. In this simplified geometry, the governing equations (2.1)-(2.3) and constitutive equations (2.4)

$$\frac{\partial \sigma^s}{\partial z} + \Pi = 0, \quad \frac{\partial \sigma^f}{\partial z} - \Pi = 0, \quad \frac{\partial(\phi \partial_t \mathbf{u} + (\mathbf{1} - \phi) \mathbf{v})}{\partial z} = 0 \quad (2.29)$$

$$\sigma^s = -\phi p + (\lambda_s + 2\mu_s) \frac{\partial u}{\partial z}, \quad \sigma^f = -(1 - \phi)p, \quad \Pi = K(v - \partial_t u). \quad (2.30)$$

for the axial displacement component $u(z, t)$ reduce to a single diffusion equations. By substituting first two equations in (2.30) into (2.29) and combining the last two equations in (2.29), the equations

$$(\lambda_s + 2\mu_s) \frac{\partial^2 u}{\partial z^2} = \frac{\partial p}{\partial z}, \quad \frac{(1 - \phi)^2}{K} \frac{\partial^2 p}{\partial z^2} = \frac{\partial^2 u}{\partial t \partial z}, \quad (2.31)$$

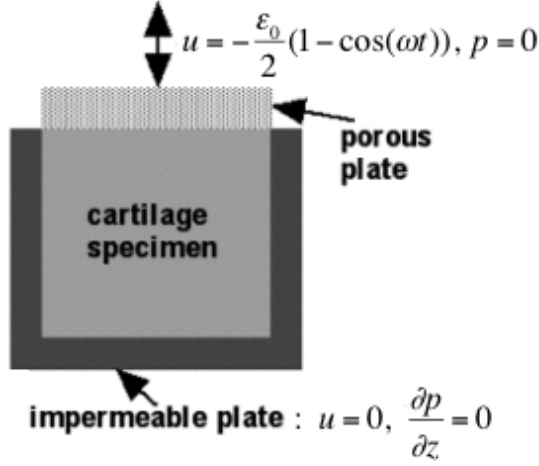


Figure 2.3: Macroscopic *in vitro* confined compression test for cartilage explant under dynamic loading.

are obtained. By integrating the second equation in (2.31) with respect to z and substituting the integrated equation into the first equation of (2.31), the following parabolic partial differential equation for the axial displacement component of the solid matrix, $u(z, t)$ is obtained:

$$\frac{\partial u}{\partial t}(z, t) - \kappa(\lambda + 2\mu) \frac{\partial^2 u}{\partial z^2}(z, t) = 0, \text{ where } \kappa = \frac{(1 - \phi)^2}{K}. \quad (2.32)$$

Suh et al. [100] derived a theoretical solution for the following initial and boundary conditions

$$\begin{aligned} u(z, 0) &= 0, \quad 0 \leq z \leq h, \\ u(0, t) &= 0, \quad \frac{\partial u}{\partial z}(h, t) = -p_0[1 - \cos(2\pi ft)], \quad t > 0, \end{aligned} \quad (2.33)$$

where h is the tissue thickness, p_0 is the applied pore pressure and f is the loading frequency. Since a primary focus of this study was on strain signal transduction, similar mathematical techniques were used to derive a theoretical solution for displacement initial and boundary conditions

$$\begin{aligned} u(z, 0) &= 0, \quad 0 \leq z \leq h, \\ u(0, t) &= 0, \quad u(h, t) = -\frac{\epsilon_0}{2}(1 - \cos(\omega t)), \quad t > 0, \end{aligned} \quad (2.34)$$

where ϵ_0 is the applied strain.

To derive an analytical series solutions, let $f(t) \equiv u(h, t)$ and $v(z, t) \equiv u(z, t) - \alpha(z)f(t)$, where $\alpha(z)(= z/h)$ is found from the boundary conditions. The parabolic differential equation

tion (2.32) can be transformed to

$$\begin{aligned} \frac{\partial v}{\partial t}(z, t) &= \kappa(\lambda + 2\mu) \frac{\partial^2 v}{\partial z^2}(z, t) + \frac{z}{h} \frac{\epsilon_0 \omega}{2} \sin(\omega t), \quad 0 < z < h, \quad t > 0, \\ v(0, t) &= 0, \quad v(h, t) = 0, \quad t > 0. \end{aligned} \quad (2.35)$$

The $v(z, t)$ can be written in following series form

$$v(z, t) \equiv \sum_{n=0}^{\infty} T_n(t) \sin((n\pi z)/h). \quad (2.36)$$

The last term in the transformed parabolic equation (2.35) can be expanded as

$$\frac{(\epsilon_0 \omega)}{2} \frac{z}{h} \sin(\omega t) = \sum_{n=1}^{\infty} \tau_n(t) \sin\left(\frac{n\pi z}{h}\right). \quad (2.37)$$

Multiplying by $\sin\left(\frac{m\pi z}{h}\right)$, integrating (2.37) from $z = 0$ to $z = h$, and using the orthogonality property of sin functions, $\tau_n(t)$ can be obtained as follows for $m = 1, 2, \dots, \infty$,

$$\begin{aligned} \frac{(\epsilon_0 \omega)}{2h} \sin(\omega t) \int_0^h z \sin\left(\frac{m\pi z}{h}\right) dz &= \sum_{n=1}^{\infty} \tau_n(t) \int_0^h \sin\left(\frac{n\pi z}{h}\right) \sin\left(\frac{m\pi z}{h}\right) dz, \\ \tau_m(t) &= \frac{\epsilon_0 \omega}{h^2} \sin(\omega t) \int_0^h z \sin\left(\frac{m\pi z}{h}\right) dz = (-1)^{m+1} \frac{\epsilon_0 \omega}{m\pi} \sin(\omega t). \end{aligned} \quad (2.38)$$

By using the relationship (2.37) and substituting τ_n to the parabolic differential equation, equation (2.35) can be written in series form

$$\begin{aligned} \sum_{n=1}^{\infty} T'_n(t) \sin\left(\frac{n\pi z}{h}\right) &= \kappa(\lambda_s + 2\mu_s) \sum_{n=1}^{\infty} \frac{-n^2 \pi^2}{h^2} T_n(t) \sin\left(\frac{n\pi z}{h}\right) \\ &+ \sum_{n=1}^{\infty} (-1)^{n+1} \frac{\epsilon_0 \omega}{n\pi} \sin(\omega t) \sin\left(\frac{n\pi z}{h}\right). \end{aligned} \quad (2.39)$$

The ordinary differential equation for $T_n(t)$ from the above equation is

$$T'_n(t) + \kappa(\lambda_s + 2\mu_s) \frac{-n^2 \pi^2}{h^2} T_n(t) = (-1)^{n+1} \frac{\epsilon_0 \omega}{n\pi} \sin(\omega t).$$

The solution

$$T_n(t) = \frac{\beta_n \omega}{\omega^2 + \alpha_n^2} e^{-\alpha_n t} - \frac{\beta_n \omega}{\omega^2 + \alpha_n^2} \cos(\omega t) + \frac{\alpha_n \beta_n}{\omega^2 + \alpha_n^2} \sin(\omega t), \quad (2.40)$$

where $\alpha_n = \frac{\kappa(\lambda_s + 2\mu_s) n^2 \pi^2}{h^2}$ and $\beta_n = (-1)^{n+1} \frac{\epsilon_0 \omega}{n\pi}$ can be easily obtained by the method of undetermined coefficients.

By substituting $T_n(t)$ into equation (2.36), the analytical series solution for displacement is obtained:

$$u(z, t) = -\frac{\epsilon_0 z}{2h}(1 - \cos(\omega t)) + \sum_{n=1}^{\infty} \frac{\beta_n}{\omega^2 + \alpha_n^2} [\omega e^{-\alpha_n t} - \omega \cos(\omega t) + \alpha_n \sin(\omega t)] \sin\left(\frac{n\pi z}{h}\right), \quad (2.41)$$

where $\omega = 2\pi f$ and the axial fluid phase velocity can be determined from equation (2.29), via the formula $v = -\frac{\phi}{1-\phi} \frac{\partial u}{\partial t}$. Once the displacement solution $u(z, t)$ is obtained, the pore pressure solution can be derived from the equation

$$\begin{aligned} p &= (\lambda_s + 2\mu_s) \left(\frac{\partial u}{\partial z}(z, t) - \frac{\partial u}{\partial z}(h, t) \right), \\ p(h, t) &= 0, \quad \frac{\partial p}{\partial z}(0, t) = 0. \end{aligned} \quad (2.42)$$

The resulting analytical solution for pore pressure is

$$\begin{aligned} p(z, t) &= (\lambda + 2\mu) \sum_{n=1}^{\infty} \frac{n\pi}{h} \frac{\beta_n}{\omega^2 + \alpha_n^2} [\omega e^{-\alpha_n t} - \omega \cos(\omega t) + \alpha_n \sin(\omega t)] \cos\left(\frac{n\pi z}{h}\right) \\ &\quad - (\lambda + 2\mu) \sum_{n=1}^{\infty} \frac{n\pi}{h} \frac{\beta_n}{\omega^2 + \alpha_n^2} [\omega e^{-\alpha_n t} - \omega \cos(\omega t) + \alpha_n \sin(\omega t)] \cos(n\pi). \end{aligned} \quad (2.43)$$

2.2.6 Microscale Modeling of Cartilage Deformation

In all subsequent simulations, the chondron is modeled as a spherical inclusion with a cell radius of $5 \mu m$ and a pericellular layer thickness of $2.5 \mu m$ [47]. The dimensions of the microscale cylindrical domain are chosen to be a radius of $19 \mu m$ and a height of $38 \mu m$, as shown in Figure 2.4(a). This geometry corresponds to a roughly 1% volume fraction of chondrocytes in cartilage when tissue is idealized as a periodic arrangement of cubes with side length equal to the diameter of the microscale cylindrical domain (Figure 2.4(b)).

To simulate microscale biphasic mechanics, the solutions in (2.41) and (2.43) were used as pressure and displacement boundary conditions on the three-zone microscale domain depicted in Figure 2.4. This is a reasonable simplification since the cells of articular cartilage are sparsely distributed within the tissue's extracellular matrix. All simulations, as well as verification of the FEM computational model, are presented in the next chapter.

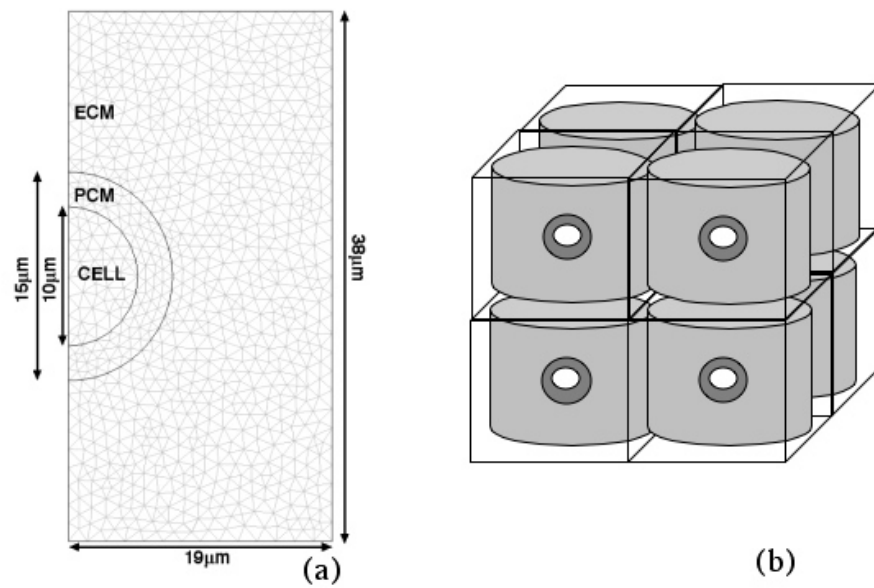


Figure 2.4: (a) Geometry and FEM mesh for simulation of microscale mechanical interactions between the chondron and ECM. (b) A square lattice arrangement of microscale domains in cartilage was used to estimate the dimensions of the mesh consistent with a 1% cell volume fraction.

Chapter 3

Simulations of the Dynamic Mechanical Environment of the Chondrocyte

The multiscale model described in chapter 2 was used to simulate the effects of macroscopic loading frequency on linear biphasic cell-matrix interactions in articular cartilage. Verification of the finite element implementation and results of the simulations are described in this chapter.

3.1 Material Properties

Cell, PCM and ECM material properties used in the simulations are shown in Table 3.1. In particular, the choice of PCM properties was based on a micropipette aspiration study [6], which developed a linear biphasic finite element model for *in vitro* micropipette aspiration and applied it to measure biphasic PCM properties for isolated chondrons from non-degenerate and osteoarthritic human cartilage. These PCM properties were employed in this study, along with the representative biphasic material property values for articular cartilage ECM and for the chondrocyte.

Loading frequencies in the range $f=0.01 - 0.1\text{Hz}$, were considered, at a level of 1% macroscopic strain. To represent mid-zone cartilage, the center of the microscale domain was taken at 50% depth, $z/h = 0.5$, where the tissue thickness was taken as $h = 1 \text{ mm}$.

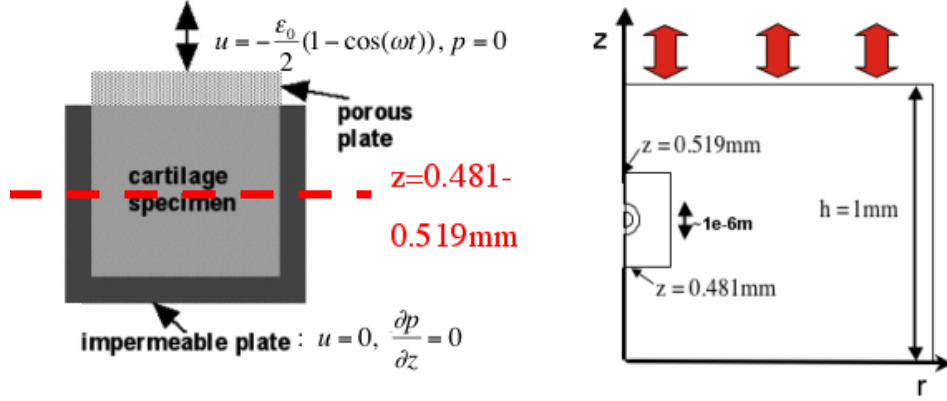


Figure 3.1: The center of the microscale domain was taken at 50% depth, where the tissue thickness was $h = 1$ mm. The microscale domain was located between $z = 0.481 - 0.519$ mm.

The top and bottom of microscale domain correspond to $z = 0.519$ mm and $z = 0.481$ mm, respectively, as depicted in Figure 3.1. For all results shown in Chapter 3, it was verified that the chosen mesh resolution (Figure 2.4) was sufficient for accurate computation of stress and strain via successive mesh refinement. The results were also analyzed to ensure that solutions did not exhibit boundary layers near the domain edges. The presence of such boundary layers would preclude the inherent assumptions in the model that microscale perturbations in the macroscopic biphasic deformation due to inclusion of the chondron vanish in the far field, where the macroscopic boundary conditions are prescribed.

Table 3.1: Material properties for the model of microscale biphasic mechanics based on [6]. In the presence of osteoarthritis (OA), Young's modulus of the PCM was significantly decreased, and the permeability was significantly elevated for both the PCM and the ECM.

	Chondrocyte	PCM	OA PCM	ECM	OA ECM
E [kPa]	0.35	38.7	23.5	1000	600
ν	0.43	0.04	0.03	0.04	0.04
κ [m^4/Ns]	10^{-16}	4.19×10^{-17}	10.2×10^{-17}	10^{-15}	2.0×10^{-15}

3.2 Mesh Refinement and Verification

To establish the final mesh resolution of 1624 elements to be employed in the simulations, the mesh was successively refined from 274 elements to 1624 elements in the

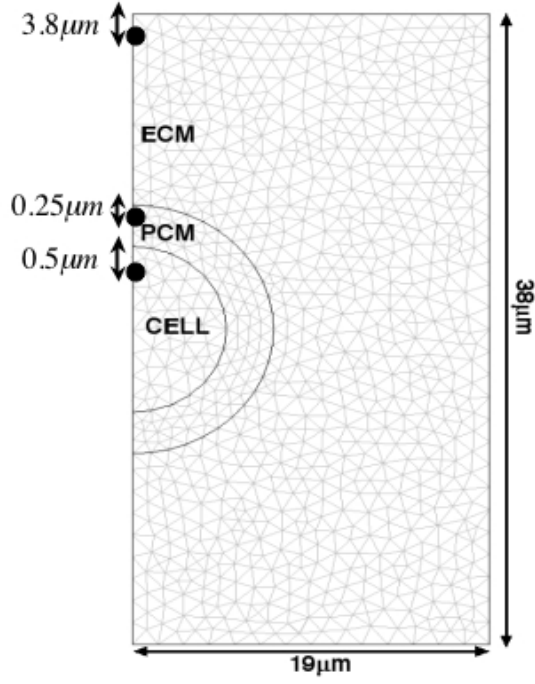


Figure 3.2: Representative points : $3.8\mu m$ below the top of the microscale domain, $0.25\mu m$ below the cell-PCM interface and $0.5\mu m$ below the PCM-ECM interface.

case where the material properties in the three zones were chosen as in Table 3.1. With these successive mesh refinements, simulation was performed at the frequency $f = 0.1$ Hz and the results are shown for pore pressure and axial strain (Figure 3.3). Pore pressure and axial strain solutions were evaluated at a point along the symmetry axis at 90% of microscale domain height, 90% of PCM thickness, and 90% of the cell radius as depicted in Figure 3.2.

With a mesh resolution of 1624 elements, the penalty number β in equation (2.6) was also varied to establish an appropriate magnitude ($\beta = 10^{20}$), and results of this procedure are shown in Figure 3.4.

The numerical solutions for axial solid strain and pore pressure were also compared with macroscopic analytical solutions (2.41) and (2.43) with material properties assigned to those of ECM (Table 3.1) in all three zones of the microscale domain. Accuracy of the custom model was also validated by comparison to previous one dimensional dynamic radial deformation solutions for a layered biphasic sphere [49] at frequency 0.1 Hz (Figure 3.6).

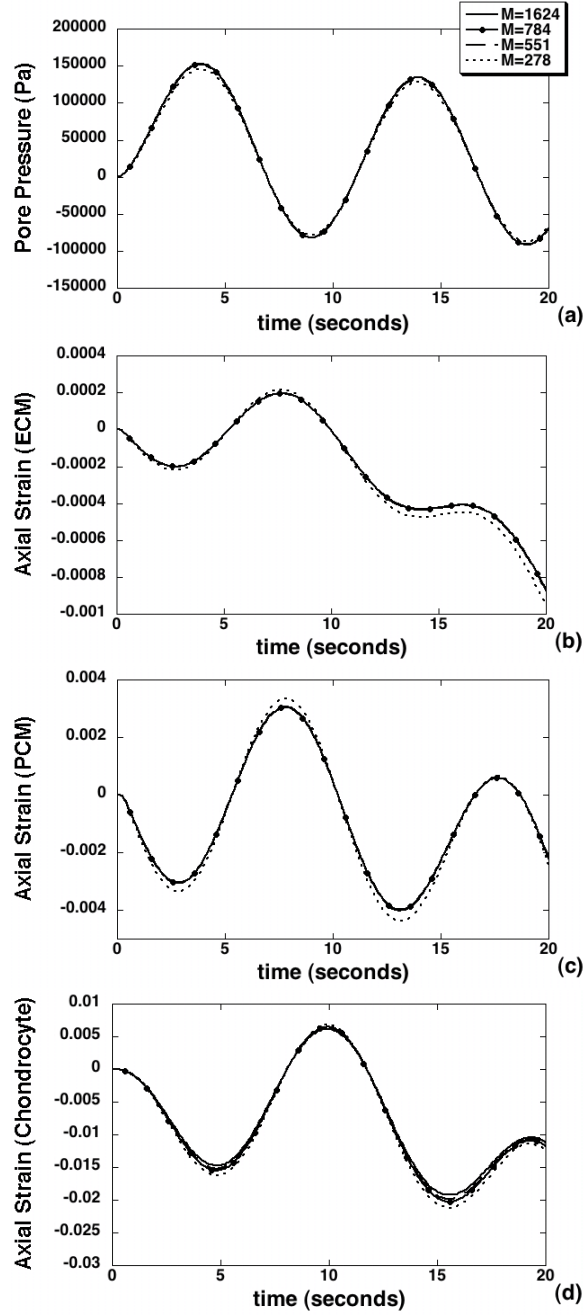


Figure 3.3: Mesh refinement performed at loading frequency $f = 0.1$ Hz, to verify numerical convergence. The number of elements chosen were 274, 551, 784, and 1624. The results are shown for (a) pore pressure (ECM) and (b) axial strain (ECM) (c) axial (PCM) strain, and (d) cellular strain at representative points in Figure 3.2.

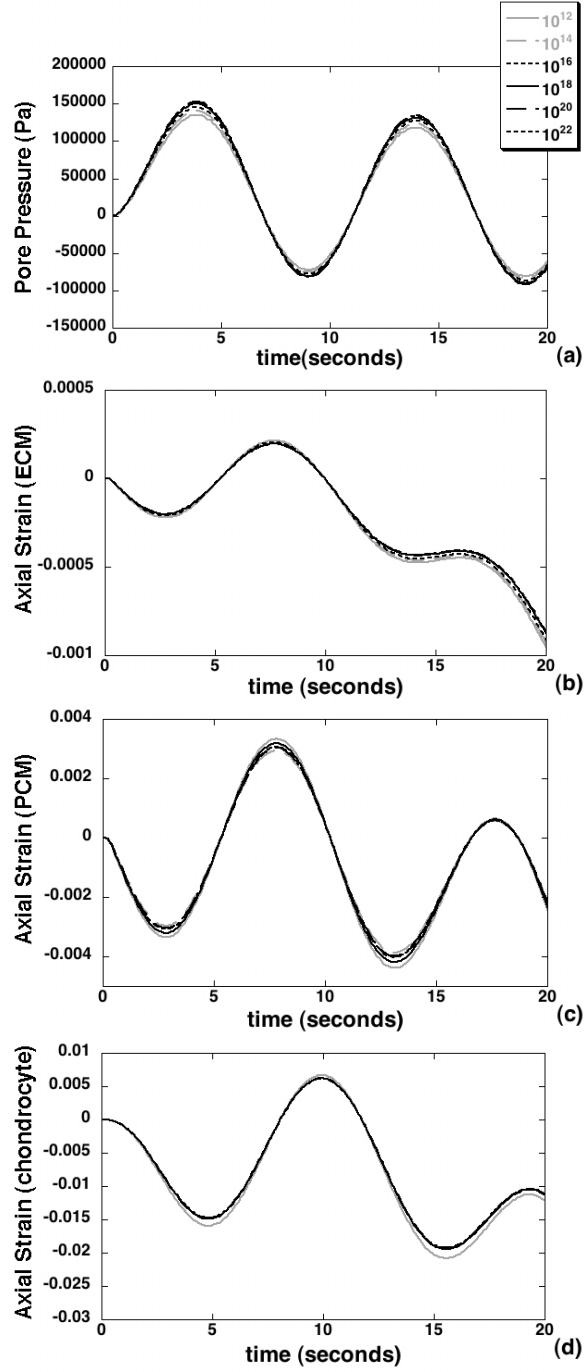


Figure 3.4: Effects of penalty number as it was varied from $\beta = 10^{12}$ to $\beta = 10^{22}$ performed at $f = 0.1$ Hz and shown for (a) pore pressure (ECM), and (b) axial strain (ECM), (c) axial strain (PCM), and (d) cellular axial strain at the three representative points (Figure 3.2).

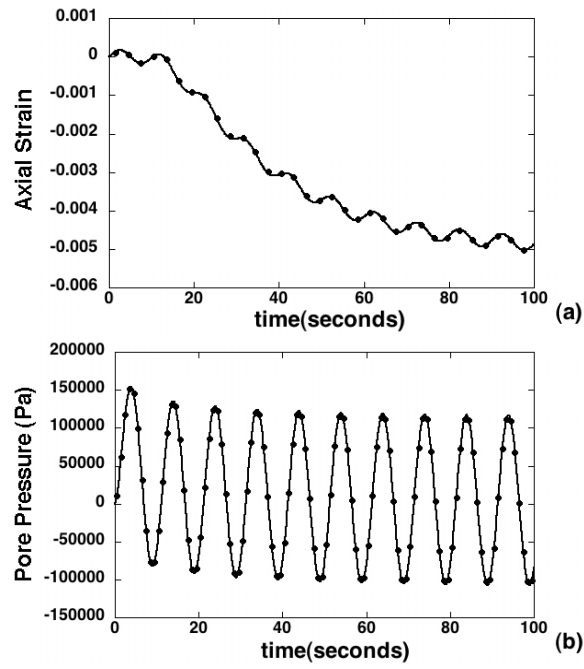


Figure 3.5: Verification of the biphasic finite element model (symbols) against analytical solution (2.41) and (2.43) for cyclic radial deformation (0.1 Hz). Comparisons are shown for (a) axial strain and (b) pore pressure at a point along the symmetry of axis at 50% height in the microscale domain.

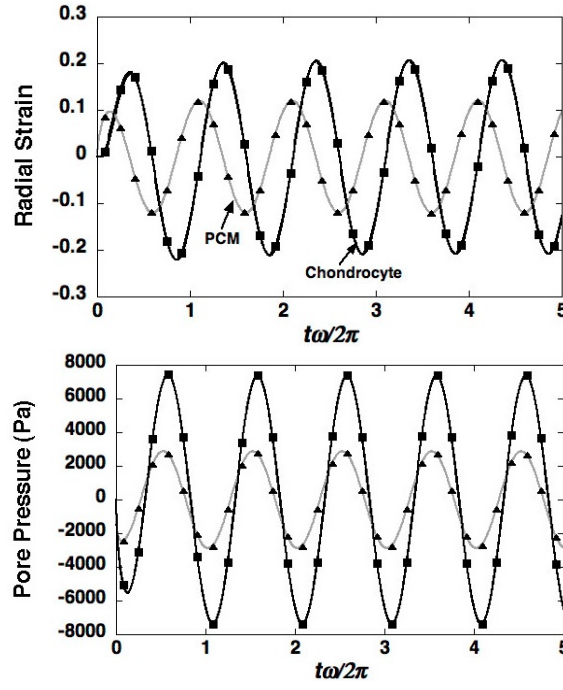


Figure 3.6: Verification of the biphasic finite element model (symbols) against a previous numerical solution [49] for cyclic radial deformation (0.1 Hz). Radial strain (top) and pore pressure (bottom) are shown at the chondron boundary and cell-PCM interface.

3.3 Simulations of Dynamic Cell-Matrix Interactions

In this section, simulation results for force transmission, strain transmission and effects of osteoarthritis on strain transmission are described. Macroscopic and microscopic force and strain transmissions are evaluated and strain amplifications in the microscopic domain for normal and osteoarthritis cases are compared.

3.3.1 Force Transmission

Theoretical solutions (2.41) and (2.43) were used to simulate the effects of loading frequency f on macroscopic transmission of forces via normal ECM to the microscopic domain containing a chondron. Specifically, axial solid stress and pore pressure were evaluated at $z = 0.519$ mm with increasing loading frequencies as depicted Figure 3.7. Amplitudes of transmitted axial solid stress and pressure were observed to increase with loading frequency. Force transmission within the microscale domain was evaluated along the symmetry axis

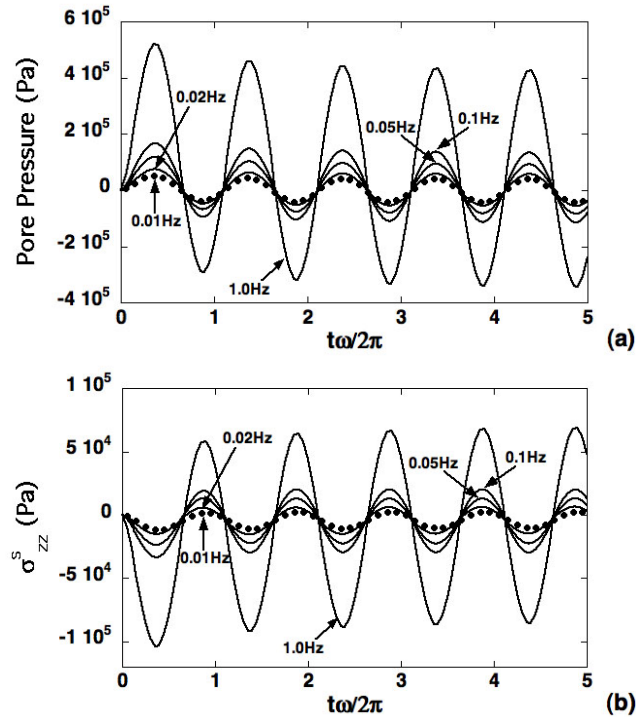


Figure 3.7: Simulations of pore pressure (a) and solid stress (b) transmitted to the microscale domain via normal ECM. Responses are shown at $z = 0.519$ mm for five different loading frequencies in the range of $f = 0.01 - 0.1$ Hz.

via a representative pericellular solid stress at $0.25 \mu\text{m}$ below the PCM-ECM interface and a representative chondrocyte solid stress at $0.5 \mu\text{m}$ below cell-PCM interface (Figure 3.2). These point locations correspond to a distance from the cell center equal to 90% of the cell radius and equal to cell radius plus 90% of PCM layer thickness (Figure 3.2). The ECM solid stress was evaluated at the top of the microscale domain. In all cases, microscale axial stress amplitude increased with advancing loading frequency, and the PCM axial solid stress response was indistinguishable from that of chondrocyte. Relative to ECM, axial stress in the chondron exhibited larger tensile amplitude and smaller compressive amplitude, with more pronounced differences at lower frequencies (Figure 3.8).

Spatial distribution of forces on the chondron is shown via a “spherical stress”, which was determined as the projection of the solid phase traction vector in the direction normal to the boundary of the chondron (Figure 3.9). The effects of increasing frequency on these spatial profiles is shown after 4.5 cycles of loading, where the stress has been normalized to its prescribed value at the upper boundary. The presence of the biphasic inclusion, representing the chondron, leads to reduction in solid stress magnitude of up to 35% at the lowest frequency $f = 0.01 \text{ Hz}$ (Figure 3.9(a)). This effect diminishes significantly with increasing loading frequency (Figure 3.9(c)).

3.3.2 Strain Transmission

Using the analytical solution (2.41), the magnitude of axial strain transmitted to the microscale domain was also evaluated (Figure 3.10). It was generally observed that macroscopically prescribed axial strain $\epsilon_0 = 1\%$ was diminished significantly in mechanical transduction to 50% depth but remained exclusively compressive. At the lower frequencies (0.01-0.02 Hz), the microscale strain exhibited a two-scale response with oscillations at the loading frequency enveloped in a slower exponentially varying curve (Figures 3.10(a), (b)). As frequency was increased, the oscillations were diminished and the response became frequency-insensitive. A slower exponentially varying curve governs the transition to equilibrium (Figures 3.10(c) and 3.10(d)).

Strain amplification in the chondrocyte was also simulated via evaluation of the axial strain, normalized to the prescribed macroscopic strain ϵ_0 . Amplification factors were evaluated at the representative points $0.25 \mu\text{m}$ below from cell-PCM interface and $0.5 \mu\text{m}$ below from PCM-ECM interface (Figure 3.2). Over the entire course of loading (500 s), the peak

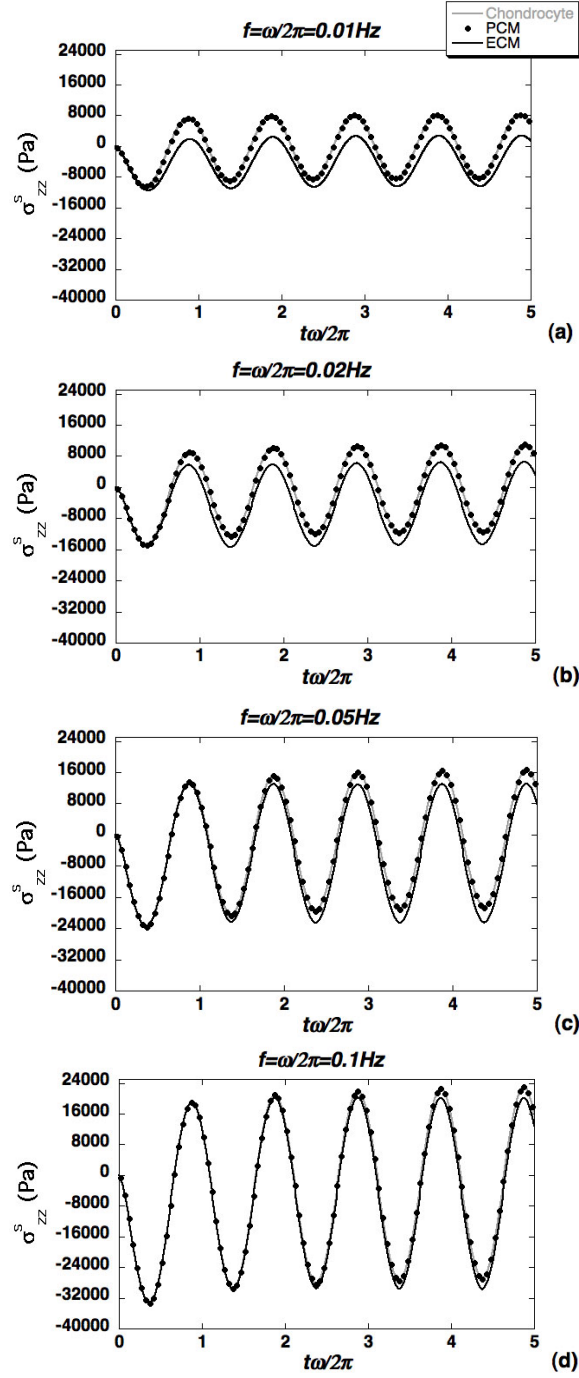


Figure 3.8: Illustration of force transmission at three points along the symmetry axis at 90% of the cell radius, 90% of the PCM thickness and at the top of the microscale domain (ECM). Axial solid stress is shown at four loading frequencies: (a) $f = 0.01$ Hz, (b) $f = 0.05$ Hz, (c) $f = 0.02$ Hz, and $f = 0.1$ Hz.

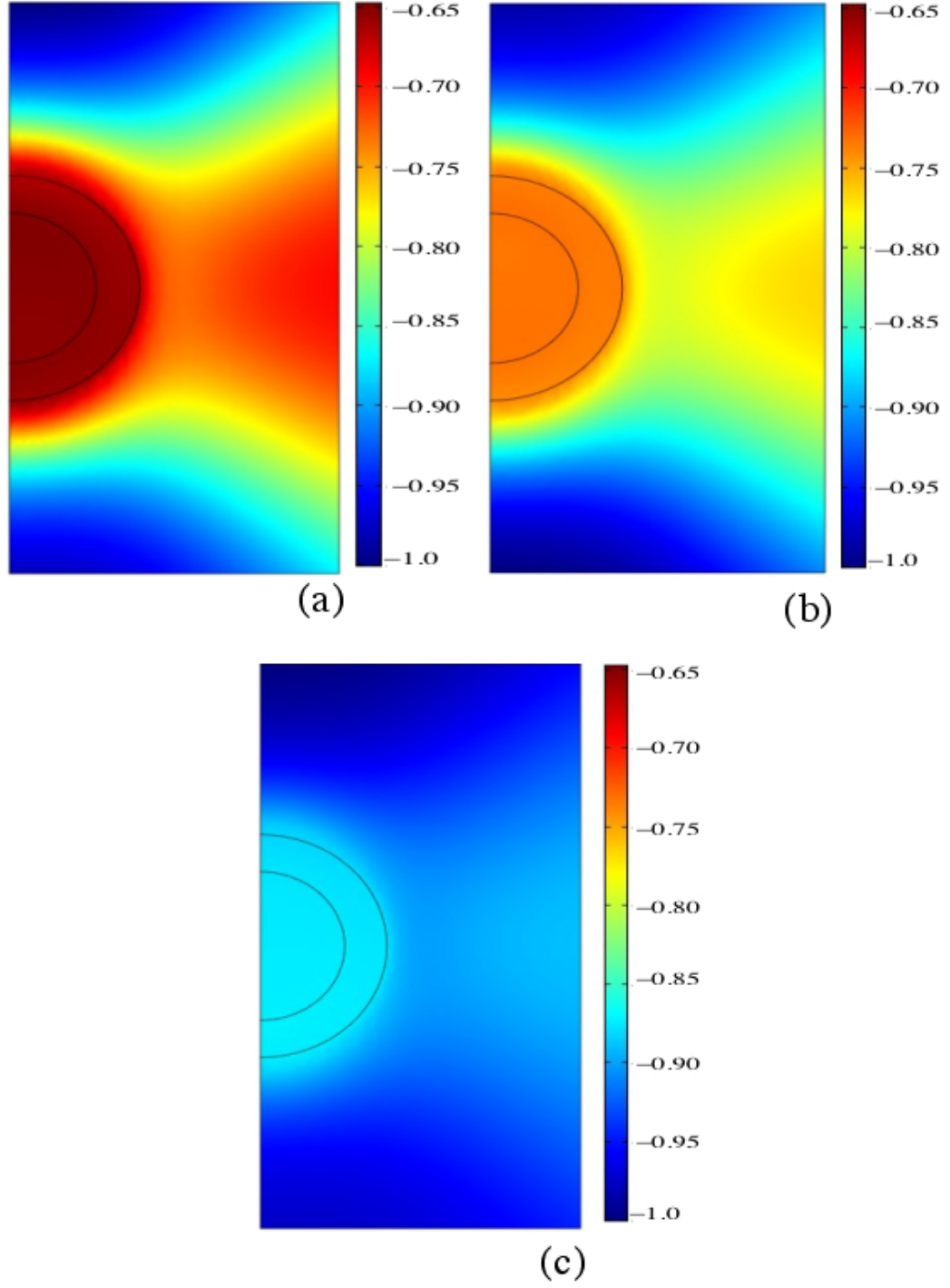


Figure 3.9: Spherical stress distribution in the microscale domain. Spherical solid stress is shown after 4.5 loading cycles for loading frequencies: (a) $f = 0.01$ Hz, (b) $f = 0.05$ Hz and (c) $f = 0.1$ Hz.

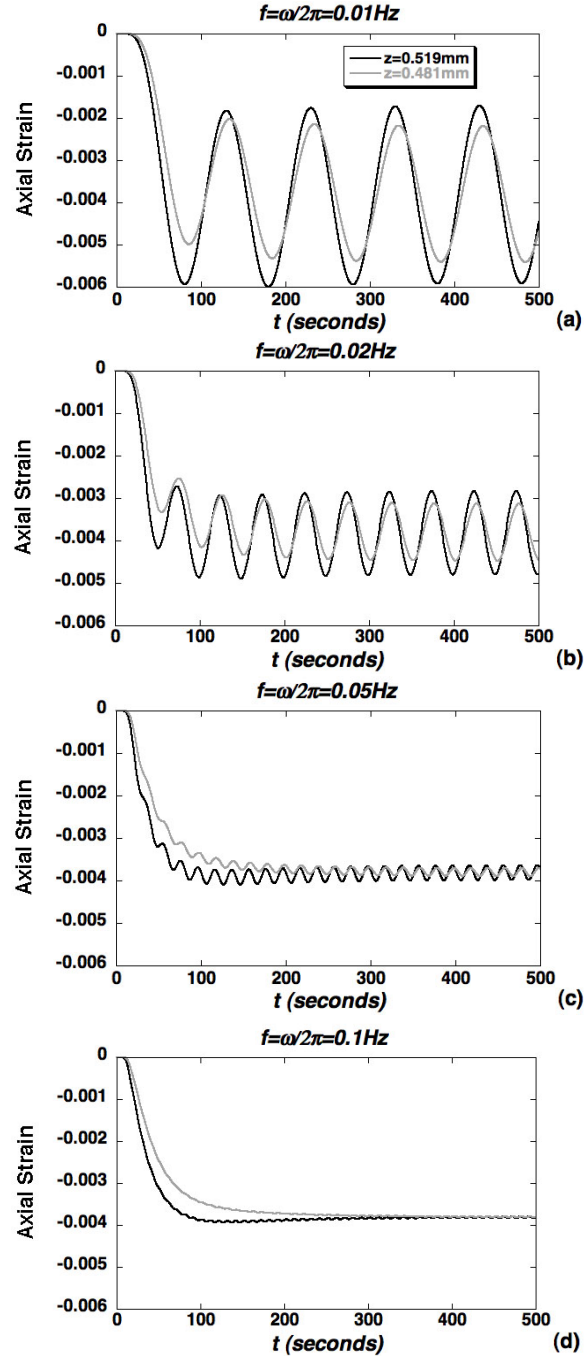


Figure 3.10: Simulations of axial strain transmitted to the microscale domain via normal ECM shown at the top and bottom of the microscale domain for loading frequencies: (a) $f = 0.01 \text{ Hz}$, (b) $f = 0.05 \text{ Hz}$, (c) $f = 0.05 \text{ Hz}$ and (d) $f = 0.1 \text{ Hz}$.

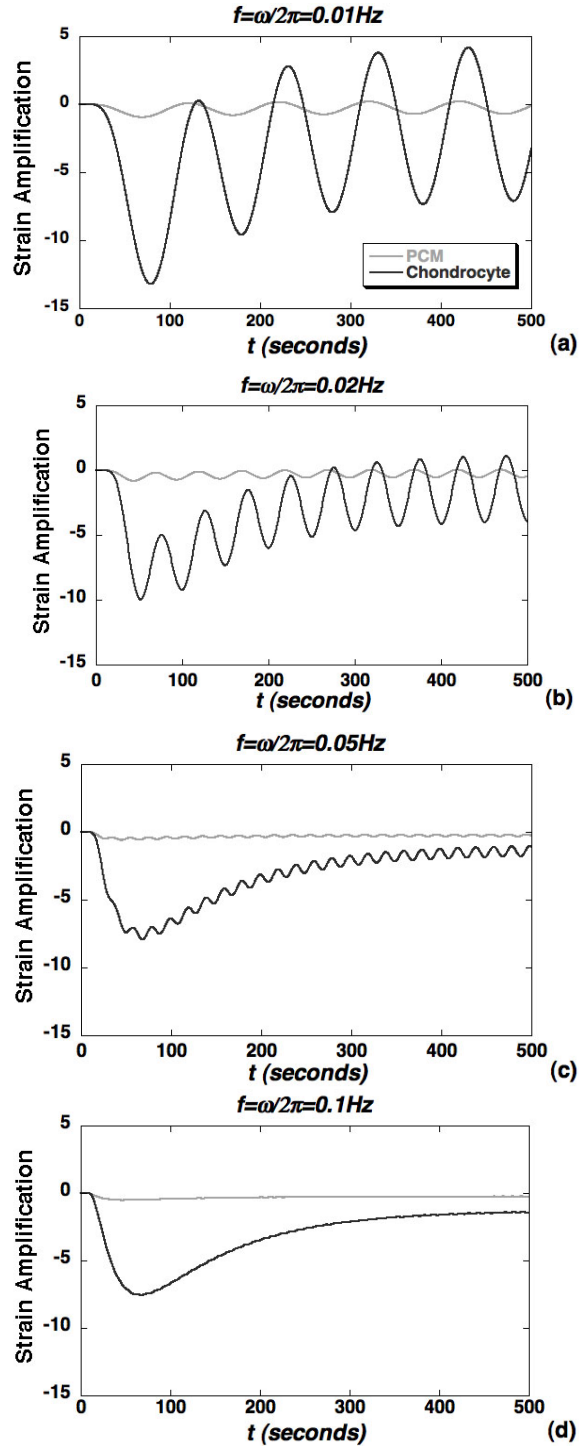


Figure 3.11: Simulations of axial strain amplification within the chondron via representative points (Figure 3.2) with the loading frequencies: (a) $f = 0.01$ Hz, (b) $f = 0.02$ Hz, (c) $f = 0.05$ Hz and (d) $f = 0.1$ Hz.

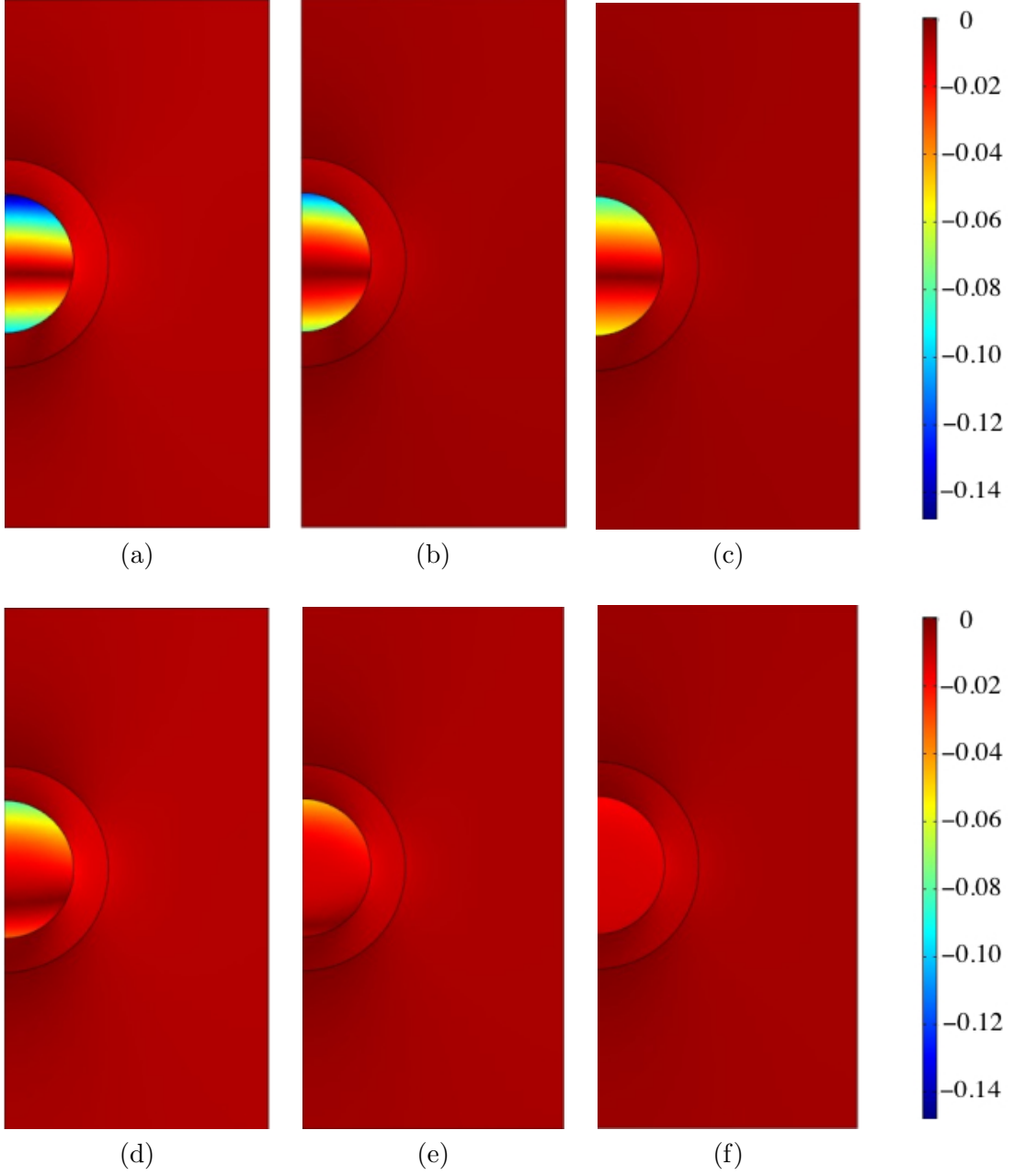


Figure 3.12: Spatial profiles of axial strain magnitude at times corresponding to peak strain amplification for $f = 0.01$ Hz ((a) $t=80$ s), $f = 0.05$ Hz ((b) $t=50$ s) and $f = 0.1$ Hz ((c) $t=70$ s), and steady state amplification at local minima for $f = 0.01$ Hz ((d) $t=480$ s), $f = 0.05$ Hz ((e) $t= 450$ s) and $f = 0.1$ Hz ((f) $t=490$ s).

cellular strain amplification factor was roughly 13 at the lowest frequency (Figure 3.11(a)) and decreased to roughly 7.5 at 0.1 Hz, where the response becomes insensitive to frequency (Figure 3.11(c) and Figure 3.11(d)). Similarly, the steady state strain amplification factor was roughly 7 at 0.01 Hz and decreased to roughly 1.5 at higher frequencies. At times corresponding to peak strain amplification, the chondrocyte exhibits nonuniform spatial distributions of axial strain (Figure 3.12(a) - (c)), while the responses were more spatially uniform in the steady state regime (Figure 3.12(d) - (f)).

3.3.3 Osteoarthritis (OA) Effects on Strain Transmission

To model potential alterations in the cellular microenvironment due to OA, simulations of strain amplification were repeated with biphasic parameter values representing two models of OA (Table 3.1). In the first case (Figure 3.13), loss of matrix stiffness was assumed to be exclusive to the PCM, while in the second case (Figure 3.14) loss of both PCM and ECM stiffness was simulated. For the OA PCM model, alterations in biphasic PCM properties resulted in a significant increase in peak strain amplification factors for all frequencies (0.01-1.0 Hz). Strain amplification factors were less altered in steady state especially at higher frequencies. For OA PCM-ECM model, peak strain amplification factors were slightly lower in the OA case but not significantly changed in the steady state (Figure 3.14). The alterations in peak amplification were less pronounced at lower frequencies as compared with the OA-PCM model. Overall, strain measures within the chondron were observed to exhibit complex spatial and time-varying responses. It was also observed that the strain responses were varied with both macroscopic loading frequency and biphasic PCM properties.

3.3.4 Discussion

Simulations presented in this chapter demonstrate that dynamic biphasic mechanics in the microscopic environment are highly dependent on features of the applied macroscopic loading and material properties of the ECM, the PCM, and cell. In particular, axial strain was shown to be sensitive to relative magnitudes of the macroscopic loading period, and characteristic mechanical response time for the ECM, the PCM and the chondrocyte. For example, in the case of axial strain signal transduction in the ECM, there are two

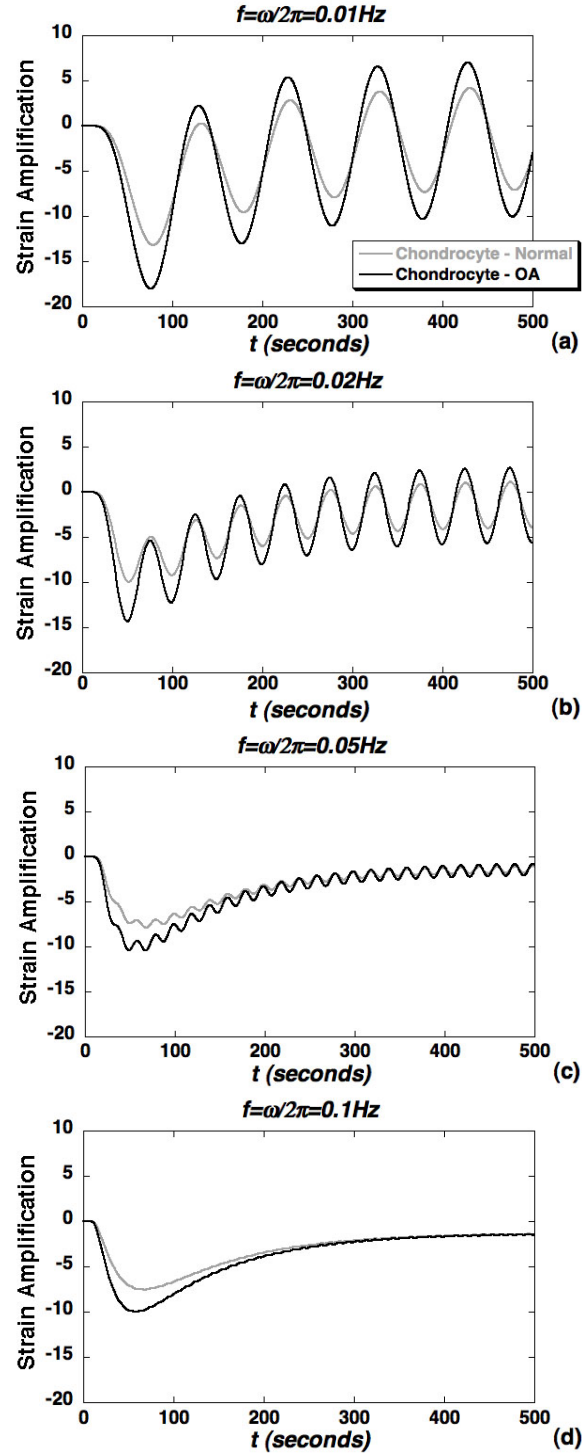


Figure 3.13: Simulations of cellular axial strain amplification within the chondrocyte via a representative point (Figure 3.2) comparing cases of normal PCM and ECM and OA exclusive to the PCM, for the loading frequencies: (a) $f = 0.01 \text{ Hz}$, (b) $f = 0.02 \text{ Hz}$, (c) $f = 0.05 \text{ Hz}$ and (d) $f = 0.1 \text{ Hz}$.

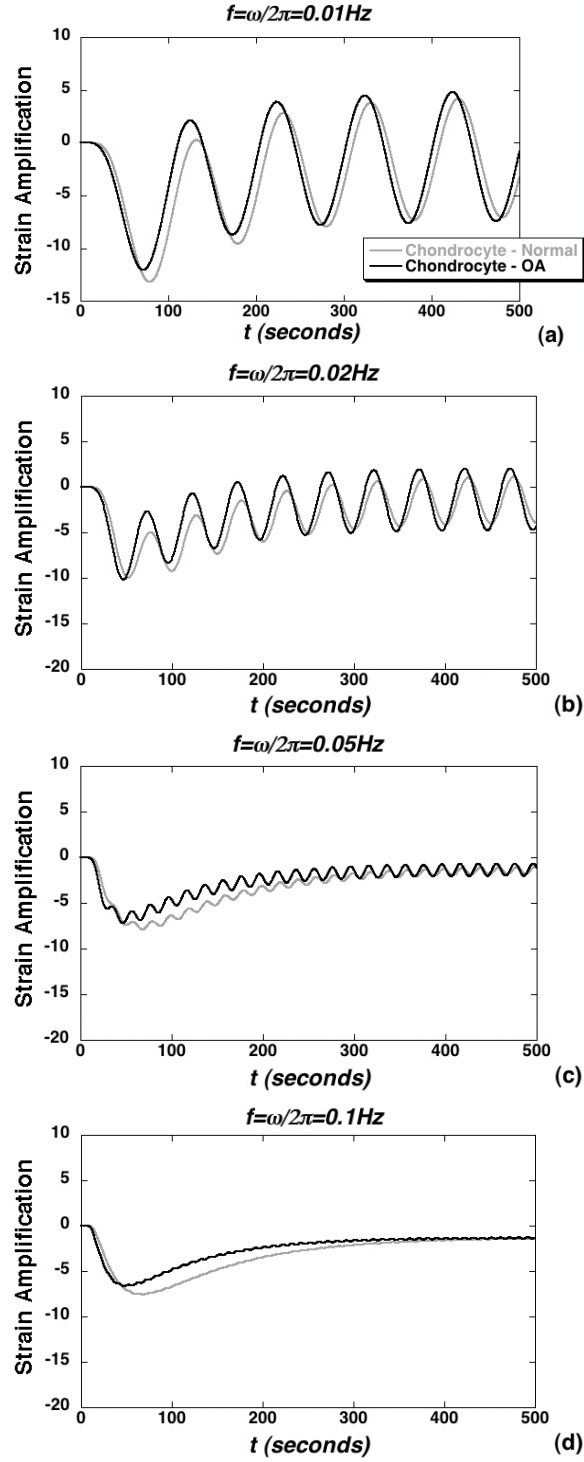


Figure 3.14: Simulations of cellular axial strain amplification within the chondrocyte via a representative point (Figure 3.2) comparing cases of normal PCM & ECM and OA PCM & ECM, for the loading frequencies: (a) $f = 0.01 \text{ Hz}$, (b) $f = 0.02 \text{ Hz}$, (c) $f = 0.05 \text{ Hz}$ and (d) $f = 0.1 \text{ Hz}$.

characteristic time scales, i.e. the loading period and ECM gel diffusion time. Simulations of macroscopic loading and transmission of biphasic deformation at 50% ECM depth under strain-controlled deformation were consistent with the findings in the force-controlled case (Equation (2.33)) that the ECM is a low-pass filter for transmission of strain (Figure 3.10), and a high-pass filter for transmission of pressure and axial solid stress (Figure 3.7) [100].

The protective role of the PCM in shielding the chondrocyte from solid stress is enhanced (Figure 3.9) at lower frequencies. At lower frequencies, the loading period and the cell, PCM and ECM gel diffusion times are on comparable scales for mechanical interaction, thus leading to significant energy dissipation by the PCM (Figure 3.9(a)). As the loading frequency is increased, coupling between these microscale biphasic mechanisms is diminished and the axial stress exhibits a more spatially uniform response (Figure 3.9(c)). The relatively uniform axial solid stress and pressure distributions within the chondron (Figure 3.8) are likely due to continuity of these quantities along biphasic interfaces. Similarly, axial solid stress amplitudes in the chondrocyte microenvironment increase substantially with increasing frequency (Figure 3.8), most likely due to insignificant recovery time for PCM diffusive drag to contribute to the overall mechanical response in this loading regime.

The multiscale simulations of axial strain focus on the potential role of intracellular strain as one biophysical variable in the process of mechanical signal transduction in articular cartilage. For the frequency range considered in this study (0.01-1.0Hz), axial strain exhibited time-varying (Figure 3.11) and nonuniform strain profiles (Figure 3.12) within the chondrocyte. At lower frequencies, axial strain in the chondrocyte is highly amplified and frequency-dependent (Figure 3.11(a)-(c)) suggesting that a combination of intracellular biophysical transduction mechanisms may be involved in this loading regime. At higher frequencies (Figure 3.12), the strain response tends to that of a non-oscillatory creep curve, most likely associated with intermittent loading at the applied strain magnitude. In this frequency range, these simulations suggest that the small loading period inhibits the ability of the tissues to exhibit fast viscoelastic recovery prior to the subsequent load cycle. Together, these findings suggest that confined compressive loading in the frequency range 0.01-0.1 Hz induces a complex time and spatially varying intracellular biophysical state that can be exploited to induce desired spatiotemporal characteristics of specific biomechanical stimuli within a tissue or construct.

Based on in vitro micropipette aspiration of isolated human chondrons, Alexopou-

los et al. [6] determined that biphasic material properties of human PCM were significantly altered with OA (Table 3.1). Simulations using the multiscale biphasic model indicate that alterations in PCM biphasic properties result in significant changes in cellular strain amplification profiles at all frequencies, particularly in the regime of peak amplification at earlier times (Figure 3.13). These findings suggest that a model of early-stage OA, in which matrix degradation is exclusive to the PCM, will induce significant changes in intracellular chondrocyte deformation in both space and time. If degenerative changes are modeled in both the PCM and ECM (Figure 3.14), the effects of these changes on the cellular microenvironment are reduced.

It should be noted that the model developed in this chapter assumes that strains are small and thus application is limited to experimental loading at small amplitudes. Additionally, the assumption of axisymmetric geometry is a model simplification. In reality, chondrocytes within cartilage ECM can exhibit non-spheroidal geometry, off-axis alignment, and small clusters of cells can be surrounded by a single PCM. In summary, the multiscale biphasic simulations presented in this study provide an initial model of dynamic cell-matrix interactions with potential application to correlating fluid and solid mechanical variables in the cartilage microenvironment to experimentally measured chondrocyte biosynthetic activity in cartilage explants and cell-gel constructs.

Chapter 4

Axisymmetric Elastic Boundary Element Method for Domains with Internal Interfaces

When the governing partial differential equations of a mathematical model are linear and elliptic, the boundary element method (BEM) can be employed. BEMs are particularly useful when quantities of interest reside, exclusively, on the domain boundaries, and for inhomogeneous materials, the internal interfaces. In the context of cartilage mechanics, a previous study developed an axisymmetric BEM for simulation of elastic mechanics for single cells subject to micropipette aspiration [50]. In this chapter, the development of a multiscale extension to this previous model for simulation of *in situ* chondron deformation in states of mechanical equilibrium is described. This forward model was developed for application in analysis of the inverse problem for estimation of PCM material properties from experimentally measured shapes of deformed chondrons within the extracellular matrix as described in chapter 5. The axisymmetric BEM requires only a one dimensional mesh along space curves at the outer ECM boundary, at the PCM-ECM interface, and at the cell-PCM interface. The model was implemented in (compiled) C, as an extension of the code developed in [50]. A primary aim was to develop a forward solver that was efficient enough to be directly called by an optimization routine in application to the inverse problem. In this chapter, the formulation, discretization, and implementation of an axisymmetric BEM

for modeling linear, isotropic, elastic deformation of domains with internal interfaces is described.

4.1 Axisymmetric Boundary Integral Formulation

Typically, an axisymmetric geometry is formed by rotating a two dimensional plane through 360° about a given axis. In cylindrical coordinates, r and θ denote the radial and angular coordinates, respectively, while z denotes the direction along the axis of rotational symmetry. The formulations developed in this chapter are exclusive to axisymmetric geometries and consequently, all loads are effectively “ring” loads. For such problems, it is sufficient to represent the domain in the rz plane and thus, the domain is two dimensional. In the BEM context, the dimensionality reduces to one spatial dimension, since the primary variables reside exclusively on the domain boundaries.

An axisymmetric boundary integral formulation requires more mathematical development than either a two or three dimensional Cartesian boundary integral formulation. Unlike finite element methods, extension is not simply a transformation of the coordinate system. There are two approaches to derive an axisymmetric boundary integral formulation. The first approach is to take the three dimensional fundamental solutions and integrate them with respect to the angular direction. The second approach is to derive solutions based on ring loads as opposed to point loads. In this study, an axisymmetric formulation based on the first approach, as in [14], was employed.

4.1.1 Cartesian Boundary Integral Equations

As discussed in Chapter 2, the equations of linear isotropic elasticity model the equilibrium deformation of a biphasic continuum mixture. The weak formulation of the governing equations (2.5) can be derived from Betti’s reciprocal work theorem and the Somigliana identity for displacement [84]. The reciprocity theorem combines two different elastic states of stress σ_{ij} and strain ϵ_{ij} in the domain Ω , described by $(\sigma_{ij}, \epsilon_{ij})$ and $(\sigma_{ij}^*, \epsilon_{ij}^*)$, respectively. The reciprocity theorem states that the work carried out in the domain Ω by applying the stress σ_{ij}^* to the strain state ϵ_{ij} is equal to the work carried out by the stress σ_{ij} on the reciprocal strain state ϵ_{ij}^* . As a result, the integral relationship in tensor form

$$\int_{\Omega} \sigma_{ij} \epsilon_{ij}^* d\Omega = \int_{\Omega} \sigma_{ij}^* \epsilon_{ij} d\Omega, \quad (4.1)$$

holds. Replacing the strains in (4.1) by the linear strain-displacement relation and using the Einstein summation convention, leads to

$$\int_{\Omega} \sigma_{ij} u_{i,j}^* d\Omega = \int_{\Omega} \sigma_{ij}^* u_{i,j} d\Omega. \quad (4.2)$$

The integrals in equation (4.2) can be rewritten as

$$\begin{aligned} \int_{\Omega} \sigma_{ij} u_{i,j}^* d\Omega &= \int_{\Omega} \left(\frac{\partial}{\partial x_j} (\sigma_{ij} u_i^*) - \frac{\partial \sigma_{ij}}{\partial x_j} u_i^* \right) d\Omega, \\ \int_{\Omega} \sigma_{ij}^* u_{i,j} d\Omega &= \int_{\Omega} \left(\frac{\partial}{\partial x_j} (\sigma_{ij}^* u_i) - \frac{\partial \sigma_{ij}^*}{\partial x_j} u_i \right) d\Omega. \end{aligned} \quad (4.3)$$

Introducing $f_i = \frac{\partial \sigma_{ij}}{\partial x_j}$ in equation (4.3), equation (4.3) becomes

$$\int_{\Omega} \left(\frac{\partial}{\partial x_j} (\sigma_{ij} u_i^*) - f_i u_i^* \right) d\Omega = \int_{\Omega} \left(\frac{\partial}{\partial x_j} (\sigma_{ij}^* u_i) - f_i^* u_i \right) d\Omega. \quad (4.4)$$

Applying the divergence theorem to equation (4.4), and noting that $t_i = \sigma_{ij} n_j$, leads to the integral equations

$$\int_{\Gamma} \sigma_{ij} u_i^* n_j d\Gamma + \int_{\Omega} f_j u_i^* d\Omega = \int_{\Gamma} \sigma_{ij}^* u_i n_j d\Gamma + \int_{\Omega} f_i^* u_i d\Omega, \quad (4.5)$$

$$\int_{\Gamma} t_i u_i^* d\Gamma + \int_{\Omega} f_i u_i^* d\Omega = \int_{\Gamma} t_i^* u_i d\Gamma + \int_{\Omega} f_i^* u_i d\Omega, \quad (4.6)$$

$$\int_{\Omega} f_i^* u_i d\Omega = \int_{\Gamma} (t_i u_i^* - t_i^* u_i) d\Gamma + \int_{\Omega} f_i u_i^* d\Omega. \quad (4.7)$$

The next step in deriving a boundary integral formulation involves transforming (4.7) to an integral equation residing exclusively on the boundary. It is also assumed that the point force f_i^* on the reciprocal displacement field u_i^* is due to a singular vector source

$$f_i^* = \delta(p, Q) \alpha_i, \quad (4.8)$$

where p is the interior point in the elastic body Ω , Q is the surface point on Γ , $\delta(p, Q)$ is the Dirac delta function, and α_i are the components of the vector source in (4.8). The solution u_i^* for a vector source of the form (4.8) is called a fundamental solution, and represents the resulting displacement response at load point Q . By inserting (4.8) into the left side

of equation (4.7) and using the property of the Dirac delta function, the left hand side of (4.7) simplifies to

$$\int_{\Omega} f_i^*(p, Q) u_i(Q) d\Omega = \int_{\Omega} u_i(Q) \delta(p, Q) \alpha_i d\Omega = u_i(p) \alpha_i(p). \quad (4.9)$$

The displacements u_i^* at the field point p due to the source at Q can be represented as

$$u_i^* = U_{ij}(p, Q) \alpha_j. \quad (4.10)$$

Similarly, the resulting tractions t_i^* can be written as

$$t_i^* = T_{ij}(p, Q) \alpha_j. \quad (4.11)$$

U_{ij} and T_{ij} are called fundamental solutions and are also known as Kelvin's solution [14], expressed in tensor notation as

$$\begin{aligned} U_{ij}(p, Q) &= \frac{1}{16\pi\mu(1-\nu)} \left[\frac{1}{r(p, Q)} \right] \left[(3-4\nu)\delta_{ij} + \frac{\partial r(p, Q)}{\partial x_i} \frac{\partial r(p, Q)}{\partial x_j} \right], \quad i, j = 1, 2, 3 \\ T_{ij}(p, Q) &= \frac{-1}{8\pi(1-\nu)r^2(p, Q)} \left[\frac{\partial r(p, Q)}{\partial n} \right] \left[(1-2\nu_{ij})\delta_{ij} + 3 \frac{\partial r(p, Q)}{\partial x_i} \frac{\partial r(p, Q)}{\partial x_j} \right] \\ &\quad - \frac{1-2\nu}{8\pi(1-\nu)r^2(p, Q)} \left[\frac{\partial r(p, Q)}{\partial x_j} n_i - \frac{\partial r(p, Q)}{\partial x_i} n_j \right], \quad i, j = 1, 2, 3 \end{aligned} \quad (4.12)$$

where $r(p, Q)$ in the above equation is the distance between the points p and Q . By substituting (4.9)-(4.11) into (4.7) and noting that α_j in (4.8) can be varied independently, the weak formulation

$$u_i(p) = \int_{\Gamma} (U_{ij}(p, Q) t_j(Q) - T_{ij}(p, Q) u_j(Q)) d\Gamma + \int_{\Omega} U_{ij}(p, q) f_i(q) d\Omega, \quad i = 1, 2, 3, \quad (4.13)$$

where p is an interior point is obtained. When there are no body forces ($f_i(p) = 0$), the reduced integral equation

$$u_i(p) = \int_{\Gamma} (U_{ij}(p, Q) t_j(Q) - T_{ij}(p, Q) u_j(Q)) d\Gamma \quad (4.14)$$

is obtained. Equation (4.14) can be rewritten in component form as

$$\begin{aligned} u_1(p) &= \sum_{j=1}^3 \int_{\Gamma} (U_{1j}(p, Q)t_j(Q) - T_{1j}(p, Q)u_j(Q)) d\Gamma, \\ u_2(p) &= \sum_{j=1}^3 \int_{\Gamma} (U_{2j}(p, Q)t_j(Q) - T_{2j}(p, Q)u_j(Q)) d\Gamma, \\ u_3(p) &= \sum_{j=1}^3 \int_{\Gamma} (U_{3j}(p, Q)t_j(Q) - T_{3j}(p, Q)u_j(Q)) d\Gamma. \end{aligned}$$

To obtain a boundary integral formulation, a limit is taken as the interior point p in (4.14) approaches the boundary Γ at a point P . Such a formulation describes the problem exclusively in terms of displacement and traction components on the domain boundary. To achieve this, an extension Γ' of boundary Γ is considered. Specifically, the boundary Γ is extended to Γ' using part of a sphere Γ_ϵ of radius of ϵ , whose center is at the point P (Figure 4.1). By taking the limit $\epsilon \rightarrow 0$, the modified boundary Γ' approaches the original boundary Γ . Based on this boundary extension, (4.14) can be rewritten as

$$\begin{aligned} u_i(p) &= \lim_{\epsilon \rightarrow 0} \int_{\Gamma - \Gamma_\epsilon^*} U_{ij}(p, Q)t_j(Q) d\Gamma - \lim_{\epsilon \rightarrow 0} \int_{\Gamma - \Gamma_\epsilon^*} T_{ij}(p, Q)u_j(Q) d\Gamma \\ &\quad + \lim_{\epsilon \rightarrow 0} \int_{\Gamma_\epsilon} U_{ij}(p, Q)t_j(Q) d\Gamma - \lim_{\epsilon \rightarrow 0} \int_{\Gamma_\epsilon} T_{ij}(p, Q)u_j(Q) d\Gamma. \end{aligned} \quad (4.15)$$

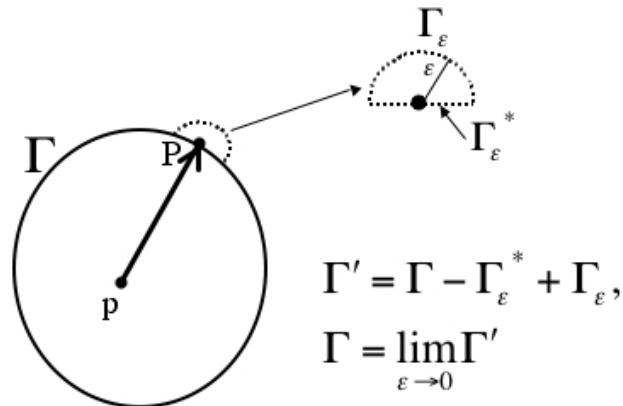


Figure 4.1: An extension of the boundary Γ around the point P .

To evaluate the last two integrals in (4.15), the singular behavior of the fundamental solutions U_{ij} and T_{ij} must be considered. When $\epsilon \rightarrow 0$, the displacement solution U_{ij} is weakly singular ($O(1/\epsilon)$), while the traction solution T_{ij} is strongly singular ($O(1/\epsilon^2)$). For physical reasons, the boundary displacement and the stress components are continuous at the singularity point, and thus, the last two integrals in (4.15) can be expressed as

$$\begin{aligned} \lim_{\epsilon \rightarrow 0} \int_{\Gamma_\epsilon} t_j(Q) U_{ij}(p, Q) d\Gamma &= \sigma_{jk}(p) \lim_{\epsilon \rightarrow 0} \int_{\Gamma_\epsilon} U_{ij}(p, Q) n_k(Q) d\Gamma \\ \lim_{\epsilon \rightarrow 0} \int_{\Gamma_\epsilon} u_j(Q) T_{ij}(p, Q) d\Gamma &= u_j(p) \lim_{\epsilon \rightarrow 0} \int_{\Gamma_\epsilon} T_{ij}(p, Q) d\Gamma. \end{aligned} \quad (4.16)$$

The unit outward normal vector n_k on the sphere Γ_ϵ and the surface area element $d\Gamma$ are

$$n_k = \begin{bmatrix} \sin(\theta_1) \cos(\theta_2) \\ \sin(\theta_1) \sin(\theta_2) \\ \cos(\theta_1) \end{bmatrix} \quad d\Gamma = \epsilon^2 \sin(\theta_1) d\theta_1 d\theta_2.$$

The fundamental solutions can be expressed as

$$U_{ij}(p, Q) = \frac{1}{\epsilon} F_1(\theta_1, \theta_2), \quad T_{ij}(p, Q) = \frac{1}{\epsilon^2} F_2(\theta_1, \theta_2), \quad (4.17)$$

where F_1 and F_2 are the bounded at the point of singularity. Hence, the integrals in (4.16) can be rewritten as

$$\begin{aligned} \lim_{\epsilon \rightarrow 0} \int_{\Gamma_\epsilon} t_j(Q) U_{ij}(p, Q) d\Gamma &= \sigma_{jk}(p) \lim_{\epsilon \rightarrow 0} \int_{\theta_1} \int_{\theta_2} \frac{1}{\epsilon} F_1(\theta_1, \theta_2) n_k(Q) \epsilon^2 \sin(\theta_1) d\theta_1 d\theta_2 = 0 \\ \lim_{\epsilon \rightarrow 0} \int_{\Gamma_\epsilon} u_j(Q) T_{ij}(p, Q) d\Gamma &= u_j(p) \lim_{\epsilon \rightarrow 0} \int_{\theta_1} \int_{\theta_2} \frac{1}{\epsilon^2} F_2(\theta_1, \theta_2) \epsilon^2 \sin(\theta_1) d\theta_1 d\theta_2. \end{aligned} \quad (4.18)$$

Based on (4.18), the boundary integral equation

$$\begin{aligned} C_{ij} u_j(P) &= \int_{\Gamma} [U_{ij}(P, Q) t_j(Q) - T_{ij}(P, Q) u_j(Q)] d\Gamma \\ C_{ij} &\equiv \lim_{\epsilon \rightarrow 0} \int_{\theta_1} \int_{\theta_2} \frac{1}{\epsilon^2} F_2(\theta_1, \theta_2) \epsilon^2 \sin(\theta_1) d\theta_1 d\theta_2, \end{aligned} \quad (4.19)$$

where the source point p has now moved to the boundary point P on Γ is obtained. Geometrically, the constants C_{ij} are proportional to the interior solid angle along Γ at the boundary point P .

4.1.2 Axisymmetric Boundary Integral Equations

To obtain an axisymmetric boundary integral formulation, the boundary integral equation (4.19) is transformed to cylindrical coordinates (r, θ, z) [14]. To achieve this, axisymmetric fundamental solutions for displacement and traction were derived by integrating the Cartesian solutions around the symmetry axis and the representation

$$P \equiv (R_P, 0, Z_P), \quad Q \equiv (r_Q \cos \theta, r_Q \sin \theta, z_Q) \quad (4.20)$$

was used to represent the points P and Q (Figure 4.2).

The axisymmetric fundamental solutions

$$U_{rr} = \frac{1}{2\pi} \int_0^{2\pi} [U_{11} \cos \theta_Q + U_{12} \sin \theta_Q] d\theta_Q, \quad U_{rz} = \frac{1}{2\pi} \int_0^{2\pi} U_{13} d\theta_Q$$

$$U_{zr} = \frac{1}{2\pi} \int_0^{2\pi} [U_{31} \cos \theta_Q + U_{32} \sin \theta_Q] d\theta_Q, \quad U_{zz} = \frac{1}{2\pi} \int_0^{2\pi} U_{33} d\theta_Q$$

can be obtained by integrating the Cartesian fundamental solutions (4.12) with respect to the angular coordinate θ ($0 \leq \theta < 2\pi$).

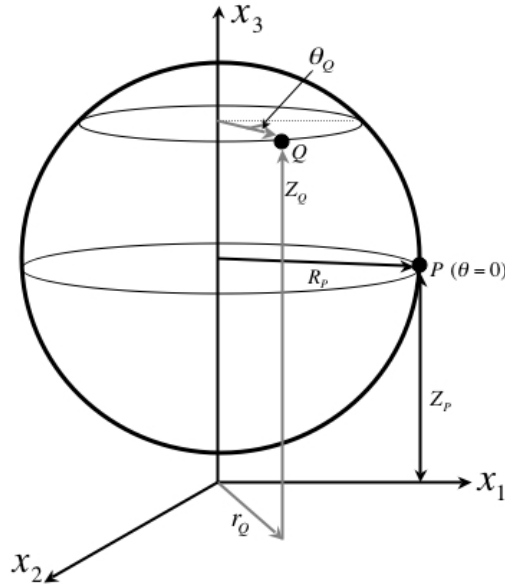


Figure 4.2: Coordinate representations of a point P in the plane $\theta = 0$ and the point Q in the axisymmetric boundary integral formulation.

The resulting displacement fundamental solutions can be written explicitly as ([14], Appendix E),

$$\begin{aligned}
U_{rr} &= \frac{A}{R_P r_Q C} [(3 - 4\nu)(R_P^2 + r_Q^2) + 4(1 - \nu)(Z_P - z_Q)^2] K\left(m, \frac{\pi}{2}\right), \\
&+ \frac{A}{R_P r_Q C} \left[-C^2(3 - 4\nu) - \frac{(Z_P - z_Q)^2 [R_P^2 + r_Q^2 + (Z_P - z_Q)^2]}{D} \right] E\left(m, \frac{\pi}{2}\right), \\
U_{rz} &= \frac{A(Z_P - z_Q)}{R_P C} \left[K\left(m, \frac{\pi}{2}\right) - \frac{r_Q^2 - R_P^2 + (Z_P - z_Q)^2}{D} E\left(m, \frac{\pi}{2}\right) \right], \\
U_{zr} &= \frac{A(Z_P - z_Q)}{r_Q C} \left[-K\left(m, \frac{\pi}{2}\right) - \frac{R_P^2 - r_Q^2 + (Z_P - z_Q)^2}{D} E\left(m, \frac{\pi}{2}\right) \right], \\
U_{zz} &= \frac{2A}{C} \left[(3 - 4\nu) K\left(m, \frac{\pi}{2}\right) + \frac{(Z_P - z_Q)^2}{D} E\left(m, \frac{\pi}{2}\right) \right],
\end{aligned} \tag{4.21}$$

where A, D, C and m are defined as

$$\begin{aligned}
A &= \frac{1}{16\pi^2 \mu (1 - \nu)}, \quad D = (R_P - r_Q)^2 + (Z_P - z_Q)^2, \\
C &= \sqrt{(R_P + r_Q)^2 + (Z_P - z_Q)^2}, \quad m = \frac{2\sqrt{R_P r_Q}}{C}.
\end{aligned} \tag{4.22}$$

In (4.21), $K\left(m, \frac{\pi}{2}\right)$ and $E\left(m, \frac{\pi}{2}\right)$ are elliptic integrals defined

$$K\left(m, \frac{\pi}{2}\right) = \int_0^{\pi/2} \frac{ds}{\sqrt{1 - m^2 \sin^2 s}}, \quad E\left(m, \frac{\pi}{2}\right) = \int_0^{\pi/2} \sqrt{1 - m^2 \sin^2 s} \, ds.$$

The axisymmetric traction fundamental solutions can be derived from the three dimensional Cartesian traction solutions in the same way. However, it is most useful to employ the strain-displacement and stress-strain relationships to express the traction fundamental solutions directly in terms of the axisymmetric displacement solutions via the relations,

$$\begin{aligned}
T_{rr} &= 2\mu n_r \left[\left(\frac{1 - \nu}{1 - 2\nu} \right) \frac{\partial U_{rr}}{\partial r} + \left(\frac{\nu}{1 - 2\nu} \right) \left(\frac{U_{rr}}{r} + \frac{\partial U_{rz}}{\partial z} \right) \right] + \mu n_z \left[\frac{\partial U_{rr}}{\partial z} + \frac{\partial U_{rz}}{\partial r} \right], \\
T_{rz} &= \mu n_r \left[\frac{\partial U_{rr}}{\partial z} + \frac{\partial U_{rz}}{\partial r} \right] + 2\mu n_z \left[\left(\frac{1 - \nu}{1 - 2\nu} \right) \frac{\partial U_{rz}}{\partial z} + \left(\frac{\nu}{1 - 2\nu} \right) \left(\frac{U_{rr}}{r} + \frac{\partial U_{rr}}{\partial r} \right) \right], \\
T_{zr} &= 2\mu n_r \left[\left(\frac{1 - \nu}{1 - 2\nu} \right) \frac{\partial U_{zr}}{\partial r} + \left(\frac{\nu}{1 - 2\nu} \right) \left(\frac{U_{zr}}{r} + \frac{\partial U_{zz}}{\partial z} \right) \right] + \mu n_z \left[\frac{\partial U_{zr}}{\partial z} + \frac{\partial U_{rz}}{\partial r} \right], \\
T_{zz} &= \mu n_r \left[\frac{\partial U_{zr}}{\partial z} + \frac{\partial U_{zz}}{\partial r} \right] + 2\mu n_z \left[\left(\frac{1 - \nu}{1 - 2\nu} \right) \frac{\partial U_{zz}}{\partial z} + \left(\frac{\nu}{1 - 2\nu} \right) \left(\frac{U_{zr}}{r} + \frac{\partial U_{zr}}{\partial r} \right) \right],
\end{aligned} \tag{4.23}$$

where n_r and n_z denote the components of unit outward normal vector at the point Q . The axisymmetric traction fundamental solutions can be then expressed in terms of elliptic integrals by substituting the displacement solutions from (4.21) into (4.23). The explicit expressions of the axisymmetric solutions are omitted, however, they can be found in Appendix D of [14].

When the point P is located on the z -axis ($R_P = 0$), the axisymmetric displacement and traction fundamental solutions remain bounded. In particular, the elliptic integrals E and K evaluate to $\pi/2$. Expanding the fundamental solutions and substituting $R_P = 0$ results in the simplified expressions

$$\begin{aligned}
U_{rr} &= U_{rz} = 0, \\
U_{zr} &= \frac{-\pi A r_Q (Z_P - z_Q)}{C^3}, \\
U_{zz} &= \frac{\pi A}{C} \left[(3 - 4\nu) + \frac{(Z_P - z_Q)^3}{C^2} \right], \\
T_{rr} &= T_{rz} = 0, \\
T_{zr} &= \frac{2\mu\pi A (Z_P - z_Q)}{C^3} \left[2(1 + \nu) - \frac{3(Z_P - z_Q)^2}{C^2} \right] n_r \\
&\quad - \frac{2\mu\pi A r_Q}{C^3} \left[(1 - 2\nu) - \frac{3(Z_P - z_Q)^2}{C^2} \right] n_z, \\
T_{zz} &= -\frac{2\mu\pi A r_Q}{C^3} \left[(1 - 2\nu) - \frac{3(Z_P - z_Q)^2}{C^2} \right] n_r \\
&\quad + \frac{2\mu\pi A (Z_P - z_Q)}{C^3} \left[(1 - 2\nu) - \frac{3(Z_P - z_Q)^2}{C^2} \right] n_z,
\end{aligned} \tag{4.24}$$

for the case $R_P = 0$ [14]. Taken together, the axisymmetric fundamental solutions given by (4.21), (4.23) and (4.24) are employed in the axisymmetric boundary integral formulation,

$$\begin{aligned}
\sum_{j=r,z} C_{rj} u_j(P) &= 2\pi \int_{\Gamma} \left[\sum_{j=r,z} T_{rj} u_j(P) - \sum_{j=r,z} U_{rj} t_j(P) \right] r_Q d\Gamma(Q), \\
\sum_{j=r,z} C_{zj} u_j(P) &= 2\pi \int_{\Gamma} \left[\sum_{j=r,z} T_{zj} u_j(P) - \sum_{j=r,z} U_{zj} t_j(P) \right] r_Q d\Gamma(Q).
\end{aligned} \tag{4.25}$$

4.1.3 Evaluation of C_{ij}

The coefficients $C_{ij}(P)$ in (4.25) depend on the local geometry of the boundary at the point P (Figure 4.3) and are given by the formulas [42]

$$\begin{aligned} C_{rr} = C_{zz} &= \frac{1}{8\pi(1-\nu)}(4(1-\nu)\beta + (\sin 2\beta_1 - \sin 2\beta_2)) \\ C_{rz} = C_{zr} &= \frac{1}{8\pi(1-\nu)}(\cos 2\beta_2 - \cos 2\beta_1) \end{aligned} \quad (4.26)$$

where $\beta_{1,2}$ is the internal angle ($\beta_{1,2} < 2\pi$) along Γ at the point P . When the boundary Γ is smooth, it follows that C_{rr} and C_{zz} are equal to 0.5 and all other terms are zero.

The formulas in (4.26) do not hold in the case that point P lies on the axis of symmetry (z -axis). In this case, the radial components of displacement and traction are zero, and only one boundary integral equation is needed and involves only U_{zr}, U_{zz}, T_{zr} and T_{zz} . Therefore, the only constant nonzero C_{zz} is [42]:

$$C_{zz} = \frac{(1-2\nu)(1-\cos\beta) - \cos^3\beta + 1}{4(1-\nu)}. \quad (4.27)$$

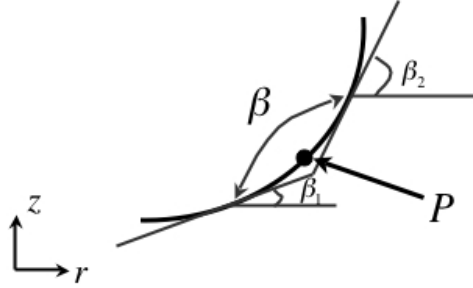


Figure 4.3: Local geometry to calculate C_{ij} .

4.1.4 Domains with Internal Interfaces

The axisymmetric boundary integral formula (4.25) was also extended for consideration of a three-zone domain with one external boundary and two internal interfaces representing the cell-PCM and PCM-ECM boundaries. Extension to this interface problem is relatively straightforward since it employs the same integral operators and fundamental

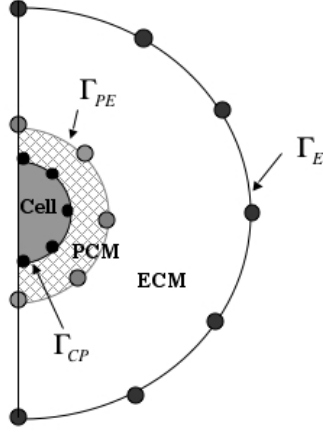


Figure 4.4: A three-zone domain for a BEM model of coupled cell-PCM-ECM deformation in articular cartilage.

solutions as for the boundary value problem (single domain). The difference is that the fundamental solutions (4.21), (4.23), and (4.24) are evaluated separately for material properties of each subdomain, and the resulting integral operators are assembled into equations on the internal interfaces that have twice as many unknowns as on the external boundary (Figure 4.4). Thus, each interface has two integral equations. The boundary integral equations are

$$\begin{aligned}
 \sum_{j=r,z} C_{ij} u_j(P) &= 2\pi \sum_{j=r,z} \int_{\Gamma_E \cup \Gamma_{PE}} [T_{ij}^{ECM} u_j(Q) - U_{ij}^{ECM} t_j(Q)] r_Q d\Gamma, \quad P \in \Gamma_E, \\
 \sum_{j=r,z} C_{ij} u_j(P) &= 2\pi \sum_{j=r,z} \int_{\Gamma_E \cup \Gamma_{PE}} [T_{ij}^{ECM} u_j(Q) - U_{ij}^{ECM} t_j(Q)] r_Q d\Gamma, \quad P \in \Gamma_{PE}, \\
 \sum_{j=r,z} C_{ij} u_j(P) &= 2\pi \sum_{j=r,z} \int_{\Gamma_{PE} \cup \Gamma_{CP}} [T_{ij}^{PCM} u_j(Q) - U_{ij}^{PCM} t_j(Q)] r_Q d\Gamma, \quad P \in \Gamma_{PE}, \quad (4.28) \\
 \sum_{j=r,z} C_{ij} u_j(P) &= 2\pi \sum_{j=r,z} \int_{\Gamma_{PE} \cup \Gamma_{CP}} [T_{ij}^{PCM} u_j(Q) - U_{ij}^{PCM} t_j(Q)] r_Q d\Gamma, \quad P \in \Gamma_{CP}, \\
 \sum_{j=r,z} C_{ij} u_j(P) &= 2\pi \sum_{j=r,z} \int_{\Gamma_{CP}} [T_{ij}^{Cell} u_j(Q) - U_{ij}^{Cell} t_j(Q)] r_Q d\Gamma, \quad P \in \Gamma_{CP},
 \end{aligned}$$

where $i = r, z$, Γ_E is the boundary of the ECM subdomain, Γ_{PE} is the interface between the PCM and ECM subdomains, and Γ_{CP} is the interface between cell and the PCM

subdomains.

4.2 Numerical Implementation

An axisymmetric boundary element method is now presented for solving the boundary integral equations (4.28). The axisymmetric boundary is discretized by placing nodal points along one-dimensional curves in the plane $\theta = 0$. Every element is divided into three segments separated by nodal points. Traction or displacement unknowns on the external boundary and on the two internal interfaces are approximated by interpolating between nodal values in each element using quadratic shape functions.

Gaussian quadrature is used to integrate the fundamental solutions over the elements, whose rotation once about the z -axis from 0 to 2π is accounted for by elliptic integrals outlined in section 4.1.2. Each boundary integral represents the effect at node Q due to a source placed at node P . All possible combinations of P and Q are integrated, including the case when P and Q are in the same element, leading to singular integrals as $r(P, Q) \rightarrow 0$ which require special treatment. In the boundary element literature, there are two primary techniques for treatment of the singular integrals: an indirect approach [14] and a direct approach [43]. The indirect computation of singular integrals employs known analytical solutions, such as plane stress or plane strain. These known solutions are substituted into the linear system of equations, which allows the unknown singular entries to be expressed in terms of matrix entries arising from regular integrals which have already been computed. However, this method is not valid for non-homogeneous problems because there are few analytical solutions available for non-homogenous domains. Thus, direct computation of singular integrals is employed in this study, in contrast to the indirect approach used in [50] which considered only boundary value problems.

Once all matrix entries have been determined, a set of boundary conditions is prescribed at each node. A new linear system is assembled by keeping unknown nodal quantities on the left side of the equation and moving known values to the right side. The system is a block system and is solved using Gaussian elimination.

4.2.1 Discretization of the Boundary and Interfaces

To define a mesh on surfaces that bound the ECM, PCM and cell, the external boundary and two internal interfaces are partitioned into M_E , M_P , and M_C elements, each with three nodes, i.e., two end points and one mid point, as in Figure 4.5. Since each zone boundary is symmetric about the z -axis, discretization requires only one-dimensional curves that represent the bounding surfaces of the ECM, PCM and cell in the plane $\theta = 0$. Since adjacent elements share an endpoint, there are $n_i = 2M_i + 1$ total nodes on each boundary, where $i = E, P, C$.

An unknown quantity on each element can be approximated using shape functions and a local variable ξ , with $\xi = 0$ at the middle node and $\xi = \pm 1$ at the two end nodes (Figure 4.5),

$$(\cdot)^m = \sum_{j=1}^3 (\cdot)^{m,j} N_j(\xi), \quad m = 1, \dots, M_i. \quad (4.29)$$

In equation (4.29), $(\cdot)^{m,j}$ is a nodal value at the j th local node of the m th element, $N_j(\xi)$ is a quadratic shape function for local node j , and $i = E, P, C$. The three following quadratic shape functions $N_j(\xi)$ all have the property that they are equal to one at their corresponding node j and zero at the other two nodes,

$$N_1(\xi) = \frac{-\xi(1-\xi)}{2}, \quad N_2(\xi) = (1+\xi)(1-\xi), \quad N_3(\xi) = \frac{\xi(1+\xi)}{2}. \quad (4.30)$$

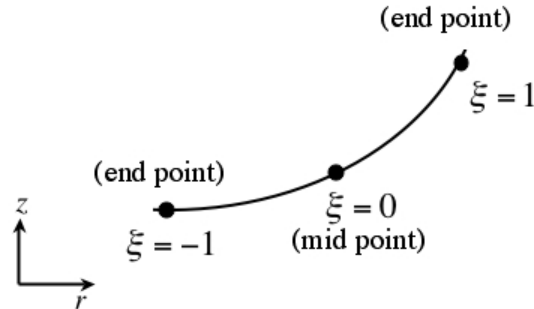


Figure 4.5: A three node isoparametric quadratic boundary element with local coordinate ξ .

4.2.2 Discretization of Boundary Integral Equations

By transforming the boundary integral equations (4.28) to the local coordinate $\xi \in [-1, 1]$, the boundary integrals over each boundary or interface are partitioned into integrals over each element m . Within each element, boundary variables are approximated using the quadratic interpolation functions as in (4.29). To discretize the integral equations, a continuous boundary quantity is replaced by interpolated local nodal values and an algebraic linear system is obtained in the manner now described.

As noted in the previous section, the number of nodes are given as n_C , n_P and n_E . Since each node is associated with two physical variables (i.e., displacement and traction) and each variable has two components (i.e., (u_r, u_z) and (t_r, t_z)), there are a total of four times as many as nodal quantities as points along each boundary. Since two components of either traction or/and displacement are prescribed on the external boundary Γ_E , there are $(2 \times n_E)$ unknowns on the ECM boundary. For the two interfaces, all displacement and traction components are unknown, and thus, there are $(4 \times n_P)$ and $(4 \times n_C)$ unknowns on the cell-PCM (Γ_{CP}) and the PCM-ECM (Γ_{PE}) interfaces, respectively. Therefore, there are a total of $N = [2 \times n_E + 4 \times n_P + 4 \times n_C]$ nodal unknowns.

To yield a unique solution, the same number (N) of equations as unknowns are required. If we assume that the point P is placed at node 1 on the ECM boundary, then the fundamental solutions can be calculated for interactions with the node 1 through node n_E . This yields the first 2 linear equations using the first equation in (4.28). To obtain the second set of linear equations, the point P is now placed at the next node and calculations of fundamental solutions are repeated. This operation is repeated until the point P is placed at the last node, which gives the final $2 \times n_E$ th equation for the external boundary. For the PCM-ECM interface, it is first assumed that the PCM-ECM interface is the boundary of ECM, then the material properties of ECM are employed to calculate fundamental solutions as in the second equation in (4.28). Next, the point P is placed at the first node on the interface, and calculations of fundamental solutions are performed with Q varying from node 1 to node n_P . This yields the first set of linear equations for the PCM-ECM interface. By repeating this operation until we reach the node n_P , the first $2 \times n_P$ linear equations are obtained. Now, the PCM properties have to be employed, since the interface is also the boundary of PCM region. Placing the point P at the node 1, evaluating fundamental

solutions with PCM properties from node 1 to n_P , and repeating a similar operation until the point Q is moved to the last node yields the other $2 \times n_P$ equations. A total of $4 \times n_P$ linear equations are obtained. For the cell-PCM interface, a similar procedure is employed to generate $4 \times n_C$ equations. Therefore, a linear system of $[2 \times n_E + 4 \times n_P + 4 \times n_C]$ equations is obtained to close the linear algebraic system.

The boundary curves are now divided into elements and the numerical integration is performed over each element using the local coordinate ξ . The Jacobian J of the transformation to element coordinates is calculated as

$$J(\xi) = \frac{d\Gamma}{d\xi} = \sqrt{\left[\frac{dr(\xi)}{d\xi}\right]^2 + \left[\frac{dz(\xi)}{d\xi}\right]^2}. \quad (4.31)$$

To determine the normal vector $\mathbf{n} = (n_r, n_z)$ used in the traction solutions, a unit tangent vector \mathbf{T} is first defined as

$$\mathbf{T} = (T_r, T_z), \text{ where } T_r = \frac{1}{|\mathbf{T}|} \frac{dr(\xi)}{d\xi}, \quad T_z = \frac{1}{|\mathbf{T}|} \frac{dz(\xi)}{d\xi}. \quad (4.32)$$

The length $|\mathbf{T}|$ is equal to the Jacobian $J(\xi)$, defined in (4.31). From the cross product of the vectors \mathbf{T} and \mathbf{e}_θ , the unit normal vector

$$\mathbf{n} = (n_r, n_z) = \frac{1}{J(\xi)} \left(\frac{dz(\xi)}{d\xi}, -\frac{dr(\xi)}{d\xi} \right) \quad (4.33)$$

is obtained. The derivatives of the coordinates $r(\xi)$ and $z(\xi)$ with respect to ξ are

$$\begin{aligned} \frac{dr(\xi)}{d\xi} &= \frac{dN_1(\xi)}{d\xi} r_1 + \frac{dN_2(\xi)}{d\xi} r_2 + \frac{dN_3(\xi)}{d\xi} r_3, \\ \frac{dz(\xi)}{d\xi} &= \frac{dN_1(\xi)}{d\xi} z_1 + \frac{dN_2(\xi)}{d\xi} z_2 + \frac{dN_3(\xi)}{d\xi} z_3. \end{aligned} \quad (4.34)$$

Now, the boundary integral equations (4.28) can be written in terms of the local coordinate

ξ as

$$\begin{aligned}
\sum_{j=r,z} C_{ij} u_j(P) &= 2\pi \left(\sum_{m=1}^{M_E+M_P} \sum_{c=1}^3 \int_{-1}^1 [T_{ir}^{ECM} u_r(Q(\xi)) - U_{ir}^{ECM} t_r(Q(\xi))] r_Q(\xi) N_c(\xi) J(\xi) d\xi \right) \\
&+ 2\pi \left(\sum_{m=1}^{M_E+M_P} \sum_{c=1}^3 \int_{-1}^1 [T_{iz}^{ECM} u_z(Q(\xi)) - U_{iz}^{ECM} t_z(Q(\xi))] r_Q(\xi) N_c(\xi) J(\xi) d\xi \right), \quad P \in \Gamma_E, \\
\sum_{j=r,z} C_{ij} u_j(P) &= 2\pi \left(\sum_{m=1}^{M_E+M_P} \sum_{c=1}^3 \int_{-1}^1 [T_{ir}^{ECM} u_r(Q(\xi)) - U_{ir}^{ECM} t_r(Q(\xi))] r_Q(\xi) N_c(\xi) J(\xi) d\xi \right) \\
&+ 2\pi \left(\sum_{m=1}^{M_E+M_P} \sum_{c=1}^3 \int_{-1}^1 [T_{iz}^{ECM} u_z(Q(\xi)) - U_{iz}^{ECM} t_z(Q(\xi))] r_Q(\xi) N_c(\xi) J(\xi) d\xi \right), \quad P \in \Gamma_{PE}, \\
\sum_{j=r,z} C_{ij} u_j(P) &= 2\pi \left(\sum_{m=1}^{M_P+M_C} \sum_{c=1}^3 \int_{-1}^1 [T_{ir}^{PCM} u_r(Q(\xi)) - U_{ir}^{PCM} t_r(Q(\xi))] r_Q(\xi) N_c(\xi) J(\xi) d\xi \right) \\
&+ 2\pi \left(\sum_{m=1}^{M_P+M_C} \sum_{c=1}^3 \int_{-1}^1 [T_{iz}^{PCM} u_z(Q(\xi)) - U_{iz}^{PCM} t_z(Q(\xi))] r_Q(\xi) N_c(\xi) J(\xi) d\xi \right), \quad P \in \Gamma_{PE}, \\
\sum_{j=r,z} C_{ij} u_j(P) &= 2\pi \left(\sum_{m=1}^{M_P+M_C} \sum_{c=1}^3 \int_{-1}^1 [T_{ir}^{PCM} u_r(Q(\xi)) - U_{ir}^{PCM} t_r(Q(\xi))] r_Q(\xi) N_c(\xi) J(\xi) d\xi \right) \\
&+ 2\pi \left(\sum_{m=1}^{M_P+M_C} \sum_{c=1}^3 \int_{-1}^1 [T_{iz}^{PCM} u_z(Q(\xi)) - U_{iz}^{PCM} t_z(Q(\xi))] r_Q(\xi) N_c(\xi) J(\xi) d\xi \right), \quad P \in \Gamma_{CP}, \\
\sum_{j=r,z} C_{ij} u_j(P) &= 2\pi \left(\sum_{m=1}^{M_C} \sum_{c=1}^3 \int_{-1}^1 [T_{ir}^{cell} u_r(Q(\xi)) - U_{ir}^{cell} t_r(Q(\xi))] r_Q(\xi) N_c(\xi) J(\xi) d\xi \right) \\
&+ 2\pi \left(\sum_{m=1}^{M_C} \sum_{c=1}^3 \int_{-1}^1 [T_{iz}^{cell} u_z(Q(\xi)) - U_{iz}^{cell} t_z(Q(\xi))] r_Q(\xi) N_c(\xi) J(\xi) d\xi \right), \quad P \in \Gamma_{CP},
\end{aligned} \tag{4.35}$$

where $i = 1, 2, 3$. Taking each node in turn as the source point P and performing the integrations indicated in the above equation, a set of linear equations in the form of $\mathbf{A}\mathbf{u} = \mathbf{B}\mathbf{t}$

emerges, where the matrices \mathbf{A} and \mathbf{B} contain the integrals of the fundamental solutions T_{ij} and U_{ij} , respectively. It is noted that the free term C_{ij} contributes only to the diagonal entries of the matrix \mathbf{A} .

4.2.3 Numerical Integration

The fundamental solutions in the integrals of T_{ij} and U_{ij} in (4.35) are evaluated for all choices of P and Q along the boundary curves. When P and Q are in the same element, the distance variable $r(P, Q) \rightarrow 0$ and the fundamental solutions become singular. Since the fundamental solutions are dependent on the distance between P and Q , the following three different possibilities for the positions of P and Q have to be considered. When P and Q are in different elements, integrals in (4.35) are nonsingular and can be evaluated by standard Gaussian quadrature,

$$\int_{-1}^1 f(\xi) d\xi = \sum_{i=1}^{n_G} w_i f(\xi_i), \quad (4.36)$$

where w_i and ξ_i are the weights and abscissas for Gaussian quadrature integration of order n_G [3].

When P and Q are in the same element but not at the same node ($P \neq Q$), the fundamental solutions U_{ij} and T_{ij} are singular. However, the singularity can be removed because the shape function $N_c(\xi)$ in the vicinity of P is of order $r(P, Q)$. Hence, the product of the fundamental solutions and the shape function is not singular and the integrals can be evaluated by the standard Gaussian quadrature (4.36). So far, all of the off-diagonal entries of the matrices \mathbf{A} and \mathbf{B} have been evaluated.

When P and Q are at the same node ($P = Q$), special techniques were employed to evaluate the integrals. For the displacement fundamental solutions U_{ij} , the singularity is of the form of $\ln(1/\eta)$ when $r(P, Q) \rightarrow 0$. This form of integral can be calculated using logarithmic Gaussian quadrature given below [97],

$$\int_0^1 f(\eta) \ln\left(\frac{1}{\eta}\right) d\eta = \sum_{gL=1}^{n_{LG}} w_{gL} f(\eta_{gL}), \quad (4.37)$$

where n_{LG} is the total number of logarithmic Gaussian integration points used and η_{gL} is the Gaussian coordinate with the weight w_{gL} . Since the limits of integration are now 0 to 1, a linear transformation can be employed to transform the integral variable from ξ to η .

If P is the first node of the element, η can be defined as $\eta = 0.5(1 + \xi)$. If P is the third node of the element, η can be defined as $\eta = 0.5(1 - \xi)$. Lastly, if P is the middle node of the element, the element is divided into two subelements ($-1 < \xi < 0$) and ($0 < \xi < 1$) and η can be defined as $\eta = -\xi$ and $\eta = \xi$, respectively, on each subinterval.

The remaining fundamental solutions T_{ij} are strongly-singular, and the strongly singular integrals exist only in the sense of the Cauchy principal value. The definition of classical Cauchy principal value in one dimension is discussed before going into the description of the calculation of strongly singular integrals in the boundary integral equations (4.35). For a function $f(x)$ with a single singularity at a point s of an interval $[a, b]$, the Cauchy principal value integral is defined by the limit

$$\oint_{[a,b]} f(x)dx = \lim_{\epsilon \rightarrow 0} \left[\int_a^{s-\epsilon} f(x)dx + \int_{s+\epsilon}^b f(x)dx \right]. \quad (4.38)$$

It is noted that the integrals on both sides of the singularity s must be taken together and that the limit is performed in a symmetric neighborhood ($s - \epsilon, s + \epsilon$) about the singular point s . To evaluate Cauchy principal integrals, the method suggested in [43] was employed. When the singular point P lies at the common point of two adjacent boundary elements, say Γ_b and Γ_a (Figure 4.6), the point P is associated with the local coordinate $\xi = 1$ in element Γ_b and the local coordinate $\xi = -1$ in element Γ_a , where ξ represents a local coordinate with $-1 \leq \xi \leq 1$.

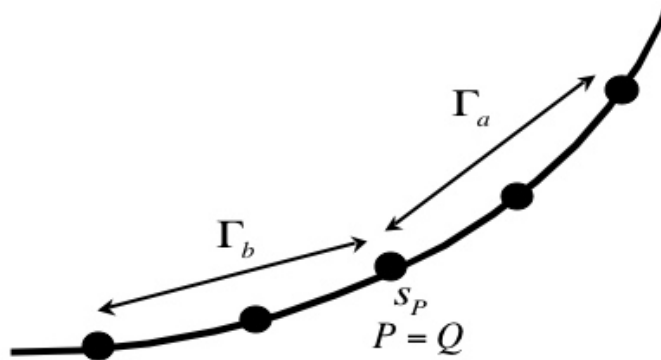


Figure 4.6: A strongly singular point P located between two boundary elements Γ_b and Γ_a on a boundary element mesh.

As in [43], the product of the traction kernel and shape function $T_{ij}(P, Q(\xi))N_c(\xi)$ is denoted as $g_b(\xi)$ and $g_a(\xi)$ on the boundary segments Γ_b and Γ_a , respectively

$$g_b(\xi) = T_{ij}(P, Q(\xi))N_c(\xi), \quad Q \in \Gamma_b, \quad g_a(\xi) = T_{ij}(P, Q(\xi))N_c(\xi), \quad Q \in \Gamma_a. \quad (4.39)$$

These functions are written in terms of regular and continuous functions $f_b(\xi)$ and $f_a(\xi)$ as follows,

$$g_b(\xi) = \frac{f_b(\xi)}{\xi - 1}, \quad g_a(\xi) = \frac{f_a(\xi)}{\xi + 1}, \quad (4.40)$$

where the denominators correspond to the strength of the singularities as $Q \rightarrow P$ within each element. Now, the Cauchy principal value integral can be expressed as,

$$\begin{aligned} I &= \oint_{\Gamma_b + \Gamma_a} T_{ij}(P, Q(\xi))N_c(\xi)d\Gamma \\ &= \lim_{\epsilon \rightarrow 0} \left(\int_{-1}^{1-\Delta\xi_b} \frac{f_b(\xi)}{\xi - 1} J_b(\xi)d\xi + \int_{-1+\Delta\xi_a}^1 \frac{f_a(\xi)}{\xi + 1} J_a(\xi)d\xi \right), \end{aligned} \quad (4.41)$$

where, in general, $J_b(\xi) \neq J_a(\xi)$. It is noted that $\Delta\xi_b$ and $\Delta\xi_a$ are related to ϵ by the Taylor series,

$$\epsilon = J_b(1)\Delta\xi_b + O(\Delta\xi_b^2) = J_a(-1)\Delta\xi_a + O(\Delta\xi_a^2). \quad (4.42)$$

Therefore, the equation (4.43) can be rewritten as

$$\begin{aligned} I &= \oint_{\Gamma_b + \Gamma_a} T_{ij}(P, Q(\xi))N_c(\xi)d\Gamma \\ &= \lim_{\epsilon \rightarrow 0} \left(\int_{-1}^{1-(\epsilon/J_b(1))} \frac{f_b(\xi)}{\xi - 1} J_b(\xi)d\xi + \int_{-1+(\epsilon/J_a(-1))}^1 \frac{f_a(\xi)}{\xi + 1} J_a(\xi)d\xi \right). \end{aligned} \quad (4.43)$$

Let $h_b(\xi) = f_b(\xi)J_b(\xi)$ and $h_a(\xi) = f_a(\xi)J_a(\xi)$. It then follows that functions $h_{b,a}(\xi)$ are regular and continuous. Noting that $h_b(1) = h_a(-1)$ from the existence of the Cauchy principal value integral, the Cauchy principal value integral I can be rewritten as,

$$\begin{aligned} I &= \lim_{\epsilon \rightarrow 0} \left(\int_{-1}^{1-(\epsilon/J_b(1))} \frac{h_b(\xi) - h_b(1)}{\xi - 1} d\xi + \int_{-1+(\epsilon/J_a(-1))}^1 \frac{h_a(\xi) - h_a(-1)}{\xi + 1} d\xi \right) \\ &+ \lim_{\epsilon \rightarrow 0} \left(\int_{-1}^{1-(\epsilon/J_b(1))} \frac{h_b(1)}{\xi - 1} d\xi + \int_{-1+(\epsilon/J_a(-1))}^1 \frac{h_a(-1)}{\xi + 1} d\xi \right) \\ &= \lim_{\epsilon \rightarrow 0} \left(\int_{-1}^{1-(\epsilon/J_b(1))} \frac{h_b(\xi) - h_b(1)}{\xi - 1} d\xi + \int_{-1+(\epsilon/J_a(-1))}^1 \frac{h_a(\xi) - h_a(-1)}{\xi + 1} d\xi \right) \\ &+ \lim_{\epsilon \rightarrow 0} ([h_b(1) \ln |\xi - 1|]_{-1}^{-1+(\epsilon/J_b(1))} + [h_a(-1) \ln |\xi + 1|]_{-1+(\epsilon/J_a(-1))}^1), \end{aligned} \quad (4.44)$$

which simplifies to

$$I = \oint_{\Gamma_b + \Gamma_a} T_{ij}(P, Q(\xi)) N_c(\xi) d\Gamma = \int_{-1}^1 \frac{h_b(\xi) - h_b(1)}{\xi - 1} d\xi + \int_{-1}^1 \frac{h_a(\xi) - h_a(-1)}{\xi + 1} d\xi - h_b(1) \ln |J_b(1)| + h_a(-1) \ln |J_a(-1)|. \quad (4.45)$$

The Cauchy principal value integral is thus expressed as the computation of two regular integrals plus logarithmic terms to take into account the relation between ξ and a singular point P . In the case of P at the middle node, the Cauchy principal value integrals can be computed by dividing the element into two sub-elements for the domains $[-1, 0]$ and $[0, 1]$, and then applying a similar procedure, using an appropriate coordinate transformation.

The numerical evaluation of the regular integrals in (4.45) can be accomplished by standard Gaussian quadrature formula,

$$I = \oint_{\Gamma_b + \Gamma_a} T_{ij}(P, Q(\xi)) N_c(\xi) d\Gamma = \sum_{i=1}^{n_G} w_i g_b(\eta_i) J_b(\eta_i) - \sum_{i=1}^{n_G} w_i \frac{h_b(1)}{\eta_i - 1} + \sum_{i=1}^{n_G} w_i g_a(\eta_i) J_a(\eta_i) + \sum_{i=1}^{n_G} w_i \frac{h_a(-1)}{\eta_i + 1} - h_b(1) \ln |J_b(1)| + h_a(-1) \ln |J_a(-1)|, \quad (4.46)$$

where η_i and w_i are the coordinates and weights of the standard Gaussian quadrature formula of order N_G . In the case of P at the middle node, the Cauchy principal value integrals can be evaluated by

$$\oint_{\Gamma_b + \Gamma_a} T_{ij}(P, Q(\xi)) N_c(\xi) d\Gamma = \sum_{i=1}^{n_G} \frac{w_i}{2} g_b \left(\frac{\eta_i - 1}{2} \right) J_b \left(\frac{\eta_i - 1}{2} \right) + \sum_{i=1}^{n_G} \frac{w_i}{2} g_a \left(\frac{\eta_i + 1}{2} \right) J_a \left(\frac{\eta_i + 1}{2} \right), \quad (4.47)$$

where the linear transformation $\xi \in [-1, 0]$ and $\xi \in [0, 1]$ in $\eta \in [-1, 1]$ have been employed. In this case, the calculation of logarithmic terms is not necessary because the Jacobians $J_b(\xi)$ and $J_a(\xi)$ are continuous across the two subelements $[-1, 0]$ and $[0, 1]$. To evaluate $h_b(1)$, it is convenient to let $h_b(1) \cong h_b(0.9999)$ as suggested in [43].

4.2.4 Boundary Conditions and Assembly

Since formulas for all coefficients of the matrices \mathbf{A} and \mathbf{B} have been determined, the boundary conditions can now be applied. At each node of Γ_E , exactly two quantities

must be specified: either u_r or t_r and either u_z or t_z . Unknown quantities are assembled on the left side of the linear system, and prescribed nodal values are moved to the right side. A new linear system $\mathbf{C}\mathbf{x} = \mathbf{bb}$ results, where \mathbf{C} and \mathbf{bb} are both formed from entries in \mathbf{A} and \mathbf{B} and the prescribed boundary conditions on Γ_E . In summary, the following matrices \mathbf{C} and \mathbf{x} are obtained.

$$\mathbf{C} = \begin{bmatrix} \mathbf{C}^{\mathbf{RR}} & \mathbf{C}^{\mathbf{RZ}} \\ \mathbf{C}^{\mathbf{ZR}} & \mathbf{C}^{\mathbf{ZZ}} \end{bmatrix} \quad (4.48)$$

$$\mathbf{C}^{\mathbf{RR}} = \begin{bmatrix} \mathbf{X}_{rr}^{\mathbf{E}} & \mathbf{A}_{rr}^{\mathbf{E}} & -\mathbf{B}_{rr}^{\mathbf{E}} & \mathbf{0} & \mathbf{0} \\ \mathbf{0} & \mathbf{A}_{rr}^{\mathbf{P}} & \mathbf{B}_{rr}^{\mathbf{P}} & \mathbf{A}_{rr}^{\mathbf{P}} & -\mathbf{B}_{rr}^{\mathbf{P}} \\ \mathbf{0} & \mathbf{0} & \mathbf{0} & \mathbf{A}_{rr}^{\mathbf{C}} & \mathbf{B}_{rr}^{\mathbf{C}} \end{bmatrix} \quad (4.49)$$

$$\mathbf{C}^{\mathbf{RZ}} = \begin{bmatrix} \mathbf{X}_{rz}^{\mathbf{E}} & \mathbf{A}_{rz}^{\mathbf{E}} & -\mathbf{B}_{rz}^{\mathbf{E}} & \mathbf{0} & \mathbf{0} \\ \mathbf{0} & \mathbf{A}_{rz}^{\mathbf{P}} & \mathbf{B}_{rz}^{\mathbf{P}} & \mathbf{A}_{rz}^{\mathbf{P}} & -\mathbf{B}_{rz}^{\mathbf{P}} \\ \mathbf{0} & \mathbf{0} & \mathbf{0} & \mathbf{A}_{rz}^{\mathbf{C}} & \mathbf{B}_{rz}^{\mathbf{C}} \end{bmatrix} \quad (4.50)$$

$$\mathbf{C}^{\mathbf{ZR}} = \begin{bmatrix} \mathbf{X}_{zr}^{\mathbf{E}} & \mathbf{A}_{zr}^{\mathbf{E}} & -\mathbf{B}_{zr}^{\mathbf{E}} & \mathbf{0} & \mathbf{0} \\ \mathbf{0} & \mathbf{A}_{zr}^{\mathbf{P}} & \mathbf{B}_{zr}^{\mathbf{P}} & \mathbf{A}_{zr}^{\mathbf{P}} & -\mathbf{B}_{zr}^{\mathbf{P}} \\ \mathbf{0} & \mathbf{0} & \mathbf{0} & \mathbf{A}_{zr}^{\mathbf{C}} & \mathbf{B}_{zr}^{\mathbf{C}} \end{bmatrix} \quad (4.51)$$

$$\mathbf{C}^{\mathbf{ZZ}} = \begin{bmatrix} \mathbf{X}_{zz}^{\mathbf{E}} & \mathbf{A}_{zz}^{\mathbf{E}} & -\mathbf{B}_{zz}^{\mathbf{E}} & \mathbf{0} & \mathbf{0} \\ \mathbf{0} & \mathbf{A}_{zz}^{\mathbf{P}} & \mathbf{B}_{zz}^{\mathbf{P}} & \mathbf{A}_{zz}^{\mathbf{P}} & -\mathbf{B}_{zz}^{\mathbf{P}} \\ \mathbf{0} & \mathbf{0} & \mathbf{0} & \mathbf{A}_{zz}^{\mathbf{C}} & \mathbf{B}_{zz}^{\mathbf{C}} \end{bmatrix} \quad (4.52)$$

$$\mathbf{x} = \begin{bmatrix} x_r & u_r & t_r & x_z & u_z & t_z \end{bmatrix}^T \quad (4.53)$$

where the elements of $\mathbf{X}_{ij}^{\mathbf{E}}, i, j = r, z$, can be integrals involving fundamental solutions of displacement, if traction is prescribed on Γ_E , and integrals of fundamental solutions for traction if displacement is prescribed on Γ_E . Similarly, x_r and x_z can be either traction or displacement components, depending on what quantity is prescribed on the external boundary.

The elements of the two matrices \mathbf{A}_{ij} and \mathbf{B}_{ij} are the integrals of traction and displacement solutions:

$$[\mathbf{A}_{ij}^k] = \left[\int_{-1}^1 T_{ij}^k(P, Q(\xi)) N_c(\xi) J(\xi) d\xi \right] \quad [\mathbf{B}_{ij}^k] = \left[\int_{-1}^1 U_{ij}^k(P, Q(\xi)) N_c(\xi) J(\xi) d\xi \right] \quad (4.54)$$

where $k = E, P, C$.

In all axisymmetric problems, the radial displacement and radial traction at the axial nodes must be exactly zero. To directly enforce these conditions, ones and zeros are placed in the corresponding entries of \mathbf{C} and \mathbf{bb} . The linear system $\mathbf{Cx} = \mathbf{bb}$ is solved by Gaussian elimination with partial pivoting. Verification of the method and results for application to the inverse problem are described in chapter 5.

Chapter 5

Application of Axisymmetric Elastic BEM for Estimation of Pericellular Matrix Properties

The boundary integral equation models developed in chapter 4 were verified against previous plane strain, plane stress, and unconfined compression solutions from linear elasticity theory. For a boundary value problem, model solutions were compared with analytical solutions for these three configurations. Accuracy of the three-zone model was also evaluated by comparison to both analytical solutions and finite element solutions.

While the elastic and viscoelastic properties of the ECM and the chondrocyte have been well established by several theoretical or experimental studies [12, 13, 28, 39, 44, 49, 53, 55, 57, 58, 73, 88, 103, 114], the mechanical properties of the PCM have been the focus of only a few studies. Previously, Alexopoulos et al. [4, 6] estimated Young's modulus, Poisson's ratio and hydraulic permeability of the PCM by comparing the model prediction of a linear biphasic finite element method with *in vitro* data from a micropipette aspiration experiment. Recently, *in situ* changes in the three-dimensional morphology of the chondron within the ECM of a cartilage explant under equilibrium unconfined compression were quantified using a novel fluorescence imaging technique targeted to type VI collagen and based on confocal microscopy [30].

The three-zone BEM model developed in the previous chapter was employed to de-

termine elastic properties of the PCM via application to analysis of experimental data from the confocal study [30]. To accomplish this task, the forward (BEM) code was integrated with nonlinear optimization techniques to estimate a set of chondron material parameters (i.e. E_{PCM} and ν_{PCM}) that minimizes the least squares residual between computed model predictions and measured quantities from the *in situ* experimental data [30].

5.1 Verification of BEM Model

Accuracy of the BEM model was evaluated by comparison to analytical solutions for plane strain, plane stress, and unconfined compression for a single domain homogeneous problem (boundary value problem). The three-zone model was also verified against these analytical solutions by assigning material properties in all three zones (cell, PCM, ECM) to be equal. For the non-homogenous three-zone case, BEM model predictions were verified against finite element solutions obtained using the software package *Comsol Multiphysics*.

The axisymmetric BEM model was implemented in compiled C on a MacBookPro laptop computer (2.0 GHz Intel Core Duo processor). All results shown employed $M = 13$ quadratic boundary elements on one-dimensional semi-ellipsoidal curves for the ECM, the PCM and cell, respectively, with 10-point Gaussian quadrature, which was sufficient for demonstrating accuracy between the numerical and analytical solutions. Analytical solutions used for verification of the BEM model are summarized in the following paragraphs.

Plane Strain: Plane strain is defined to be a state of strain in which the strains ϵ_{zz} , ϵ_{rz} and $\epsilon_{\theta z}$ are assumed to be zero. From these assumptions, the analytical solution

$$u_r = (1 + \nu)(1 - 2\nu)r, \quad u_z = 0, \quad t_r = En_r, \quad t_z = 2\nu En_z, \quad (5.1)$$

is obtained. A comparison of axisymmetric BEM model solutions to the known solutions for plane strain deformation demonstrates excellent agreement with equation (5.1) (Figure 5.1).

Plane Stress: Plane stress is a state of stress in which σ_{zz} , σ_{rz} and $\sigma_{\theta z}$ are assumed to be zero. Under these assumptions, the plane stress solution is

$$u_r = (1 - \nu)r, \quad u_z = -2\nu z, \quad t_r = En_r, \quad t_z = 0. \quad (5.2)$$

BEM model solutions were also verified against the above plane stress solution with excellent agreement (Figure 5.2).

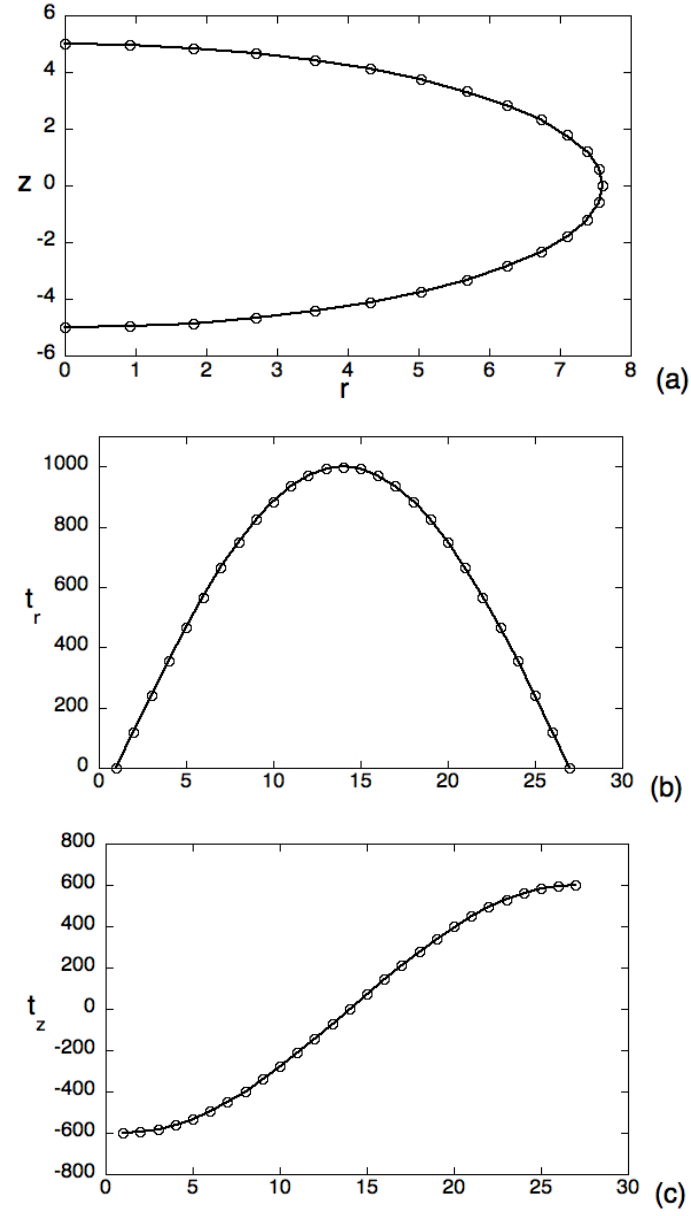


Figure 5.1: Verification of BEM model for plane strain with $\nu = 0.3$ and $E = 1000\text{Pa}$ shown for (a) displacement, (b) radial traction, and (c) axial traction comparing BEM model solutions (circles) to the analytical solution (solid line).

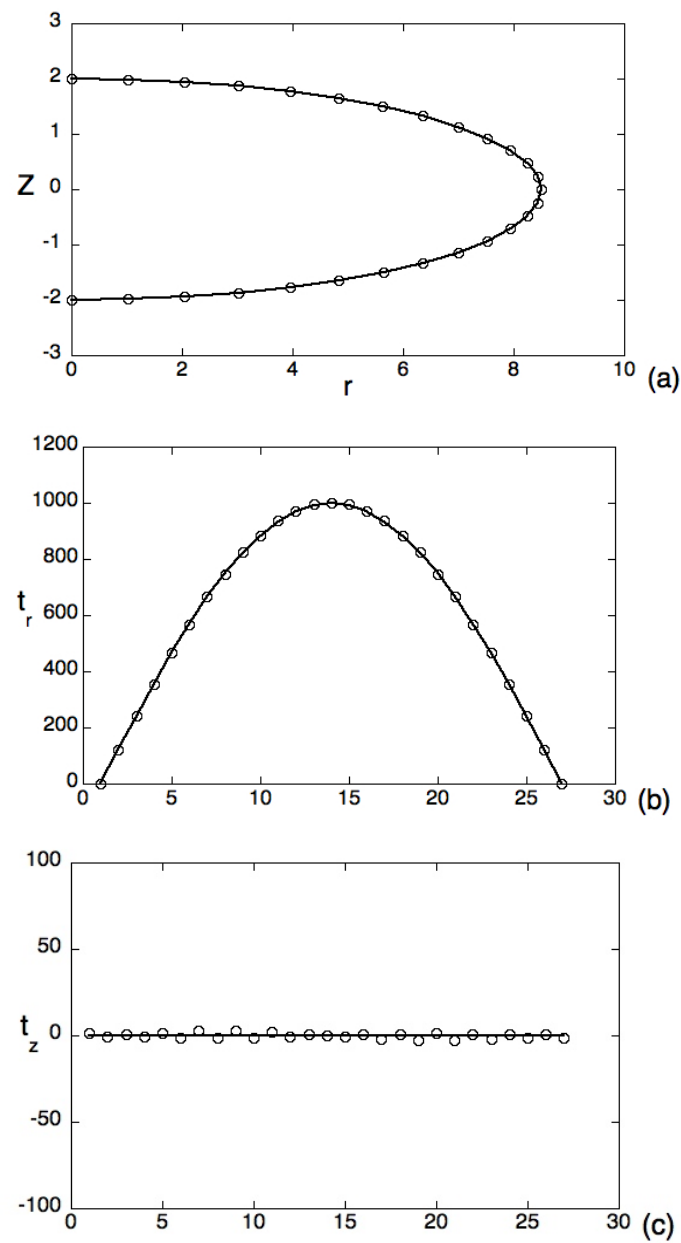


Figure 5.2: Verification of BEM model for plane stress with $\nu = 0.3$ and $E = 1000\text{Pa}$ shown for (a) displacement, (b) radial traction, and (c) axial traction comparing BEM model solutions (circles) to the analytical solution (solid line).

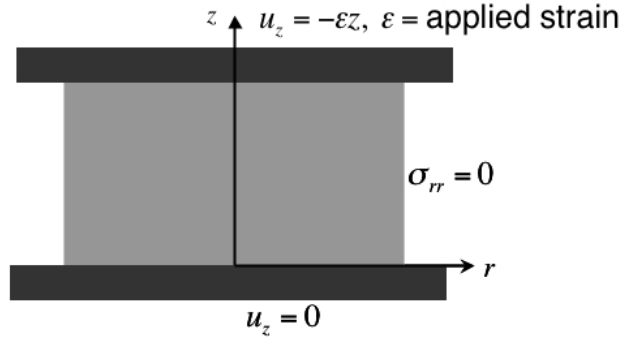


Figure 5.3: Diagram of unconfined compression test on a cylindrical biphasic sample.

Unconfined compression: As articular cartilage experiences significant compressive stresses, it is important to evaluate its response in compression. The unconfined compression test is one of the most commonly used tests for in vitro analysis of deformation in articular cartilage explants. A compressive normal displacement or normal traction is applied over the top surface of the cartilage explant as shown in Figure 5.3. The compression platen is impermeable and smooth, and thus radial expansion is allowed. The boundary condition $u_z = -\epsilon z$ is applied on the top platen and fluid in the tissue flows out of the sample as the tissue undergoes volumetric deformation. Under the assumption that the tissue achieves a state of linear, isotropic, biphasic mechanical equilibrium, the following elastic analytical solution for the displacements can be derived [11],

$$u_r = -\frac{\lambda}{2(\lambda + \mu)}\epsilon r, \quad u_z = -\epsilon z. \quad (5.3)$$

The traction solution can be obtained using the strain-stress relations as,

$$t_r = (2C(\lambda + \mu) + \epsilon\lambda)n_r, \quad t_z = (2\lambda C + \epsilon(\lambda + 2\mu))n_z. \quad (5.4)$$

where $C = -\frac{\lambda}{2(\lambda + \mu)}\epsilon$.

A comparison of axisymmetric BEM model solutions to the solutions in (5.3)-(5.4) is shown for radial displacement, and radial and axial traction, and demonstrates excellent agreement (Figure 5.4).

The three-zone BEM model was also verified against analytical solutions for plane stress, plane strain and unconfined compression by assuming all three zones have the same material properties (Figures 5.5-5.7). For the non-homogenous problem, an elastic finite

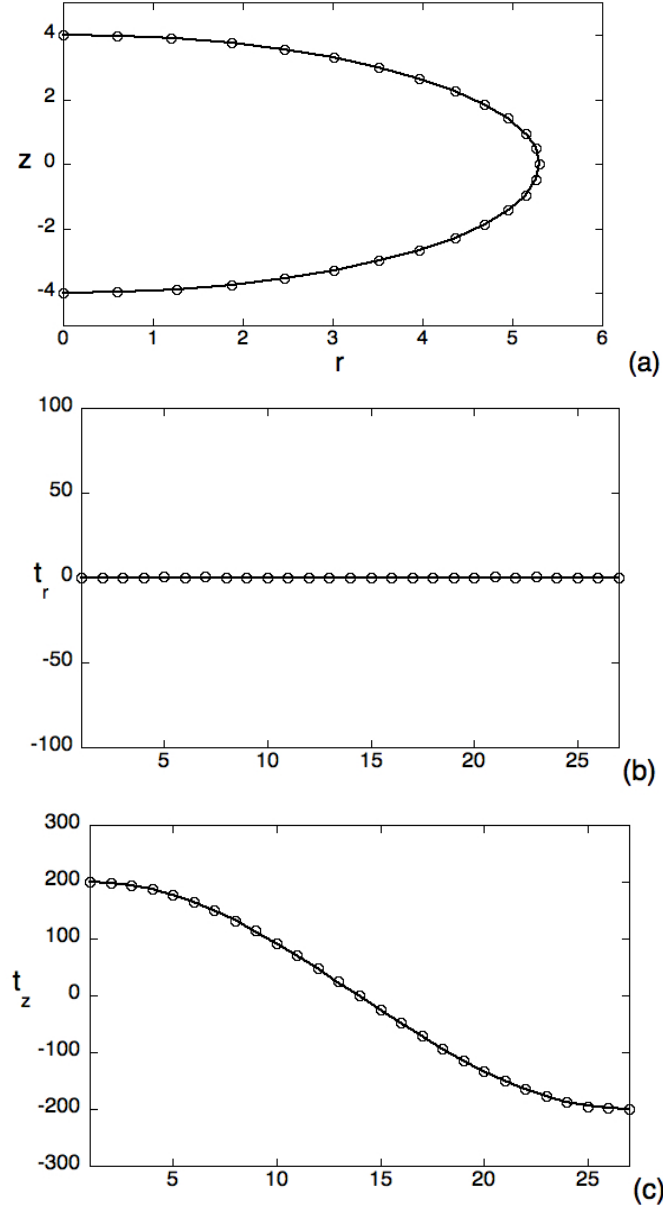


Figure 5.4: Verification of BEM model for unconfined compression with $\nu = 0.3$ and $E = 1000\text{Pa}$ shown for (a) displacement, (b) radial traction, and (c) axial traction comparing BEM solutions (circles) to the analytical solution (solid line).

element solution was also compared with solutions to the three-zone BEM model (Figure 5.8). Cell, PCM and ECM material properties from the *in vitro* study [6] (see Table 3.1) were used to simulate the unconfined compression test and to compare BEM solutions with finite element solutions, which were obtained from *COMSOL Multiphysics* via the *Structural Mechanics Module* using the options *Axial Symmetry, Stress-Strain Application Module*. All of these comparisons demonstrated excellent agreement (Figures 5.5-5.8).

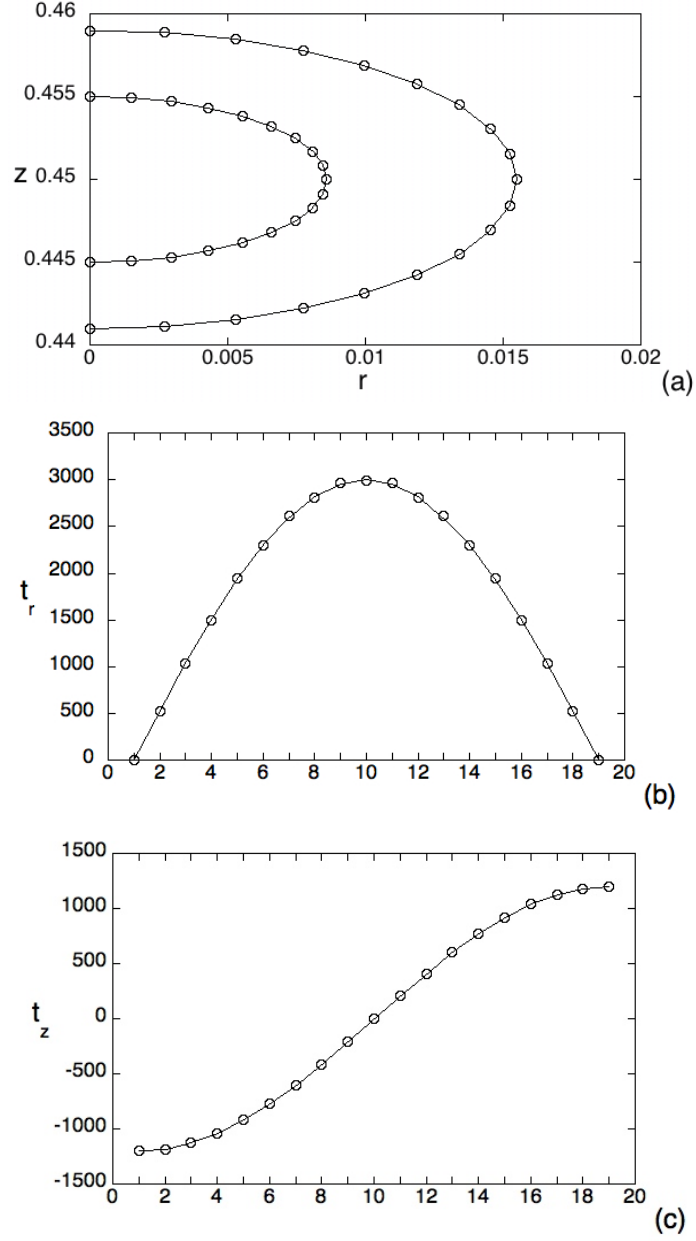


Figure 5.5: Verification of the three-zone BEM model for plane strain with $\nu_{ECM} = \nu_{PCM} = \nu_{cell} = 0.2$ and $E_{ECM} = E_{PCM} = E_{cell} = 2000\text{Pa}$ shown for (a) displacement on cell-PCM and PCM-ECM interfaces, (b) radial traction on PCM-ECM interface, (c) axial traction on PCM-ECM interface comparing BEM model solutions (circles) to the analytical solution (solid line).

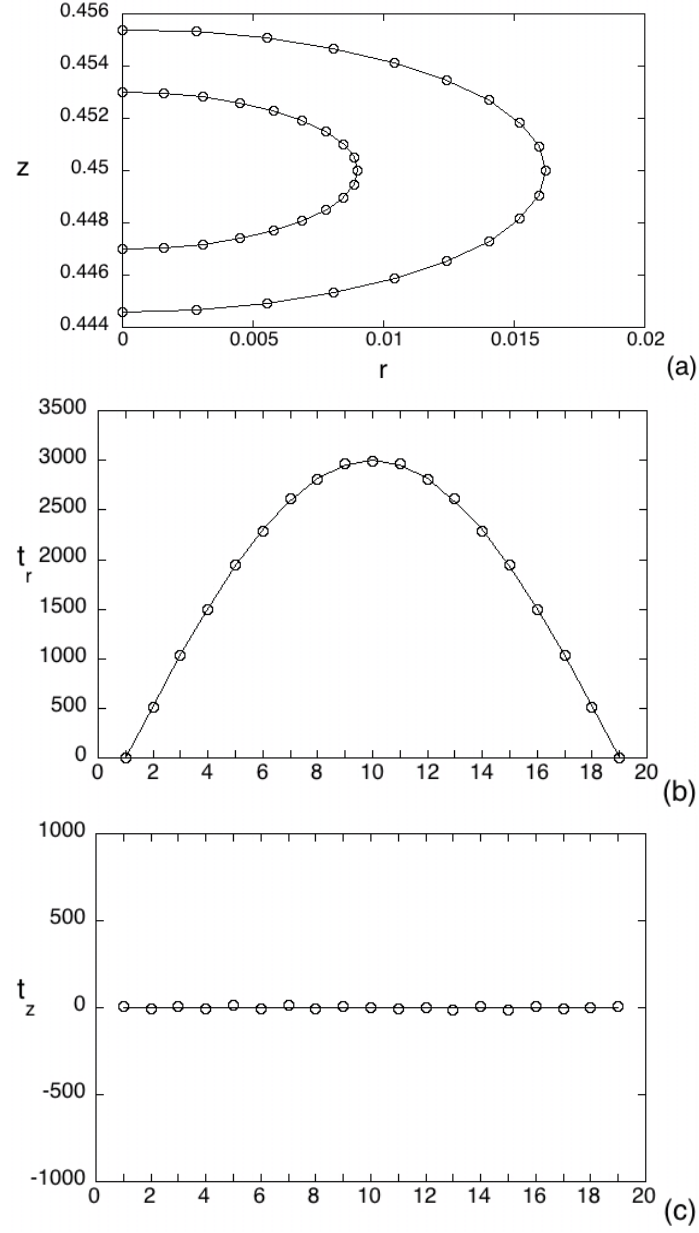


Figure 5.6: Verification of the three-zone BEM model for plane stress with $\nu_{ECM} = \nu_{PCM} = \nu_{cell} = 0.2$ and $E_{ECM} = E_{PCM} = E_{cell} = 2000\text{Pa}$ shown for (a) displacement on cell-PCM and PCM-ECM interfaces, (b) radial traction on PCM-ECM interface, (c) axial traction on PCM-ECM interface comparing BEM solutions (circles) to the analytical solution (solid line).

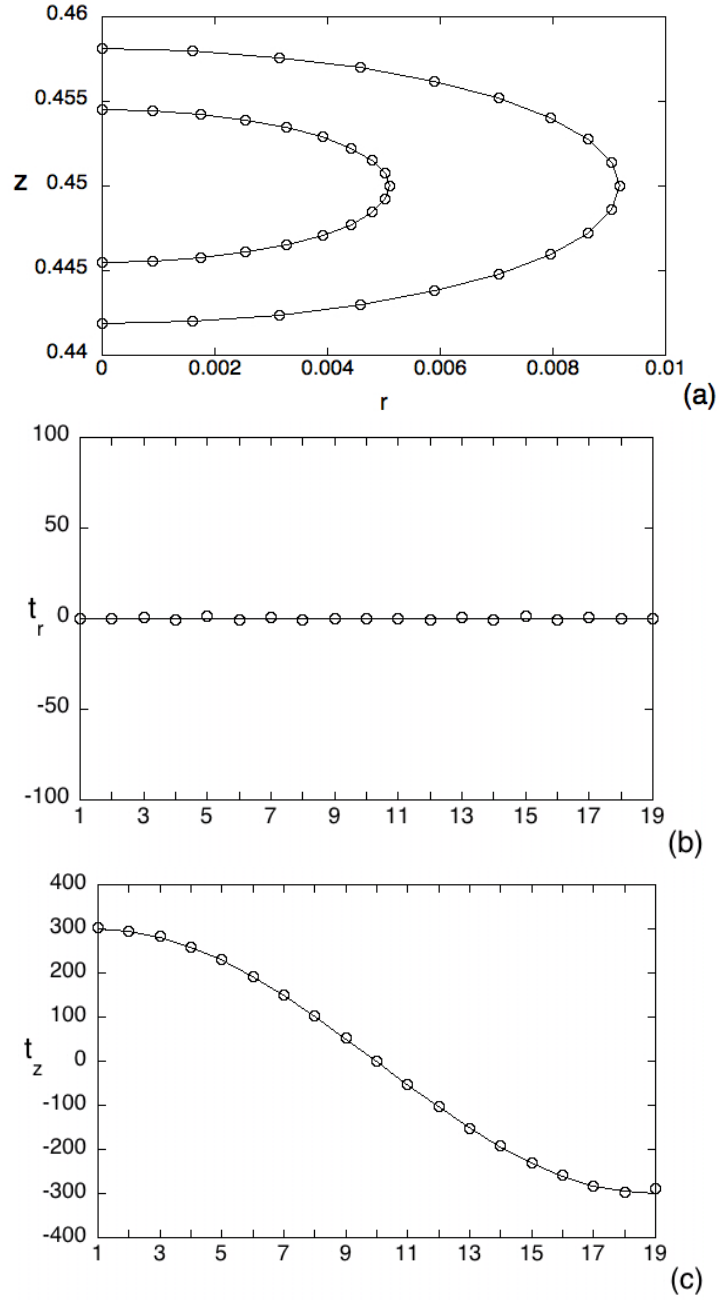


Figure 5.7: Verification of the three-zone BEM model for unconfined compression test with $\nu_{ECM} = \nu_{PCM} = \nu_{cell} = 0.2$ and $E_{ECM} = E_{PCM} = E_{cell} = 2000\text{Pa}$ shown for (a) displacement on cell-PCM and PCM-ECM interfaces, (b) radial traction on PCM-ECM interface, (c) axial traction on PCM-ECM interface comparing BEM solutions (circles) to the analytical solution (solid line).

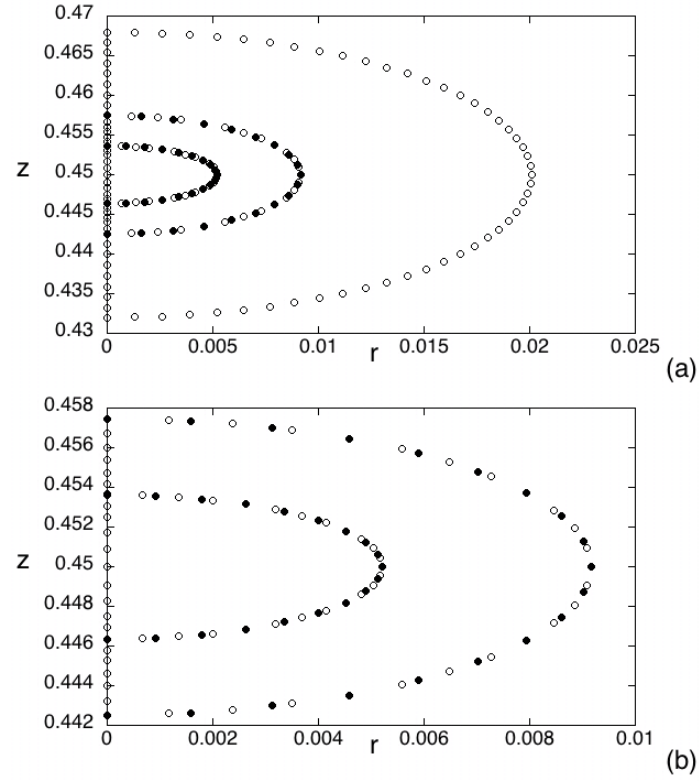


Figure 5.8: Verification of three-zone BEM model solutions for unconfined compression shown for (a) displacement on cell-PCM and PCM-ECM interfaces and (b) magnified figure of displacement comparing BEM solutions (open circles) to finite element solutions (solid circle).

5.2 Experimental Data for In Situ Chondron Deformation

While *in vitro* experimental studies use techniques like micropipette aspiration to measure deformation of isolated chondrocytes or chondrons, *in situ* studies examine their deformation within the ECM of cartilage explants. Previously, either confocal microscopy [48] or histologic fixation and physical sectioning [23, 83] were employed to study the three-dimensional deformation behavior of the chondrocyte. These studies show that cell shape and volume are highly dependent upon local ECM deformation. While several *in situ* measurements of the chondrocyte deformation are available, the *in situ* mechanical behavior of the PCM has not been fully characterized.

Recently, Choi et al. [30] quantified changes in the three dimensional morphology of the intact chondron in different zones (superficial, middle, deep) under 10% - 50% magnitudes of equilibrium unconfined compressive strain applied to cylindrical cartilage explants. They used a novel confocal microscopy technique, based on fluorescence immunolabeling for type-VI collagen (which is exclusive to PCM), to identify the boundary of the PCM. All chondrons used to quantify morphological changes were selected from radially central regions of the tissue to avoid inhomogeneous strain fields due to friction between the compressing platen and the tissue. This choice of cells is also consistent with use of an axisymmetric model for analysis of the experimental data. From their three dimensional reconstructed ellipsoidal shapes of the chondron, they recorded the chondron's height, medial-lateral (ML) width, anterior-posterior (AP) width and estimated the cell's volume. Examples of chondron and cell shapes and morphological data at 10% compression are shown in Figure 5.9, and examples of chondrons and cell experimental data are shown in Tables 5.1-5.2.

Table 5.1: Chondrons' morphological parameters at superficial, middle and deep zones. Left columns in each zone represent uncompressed data and right columns represent deformed shapes under 10% compressive strain, from [30].

	superficial		middle		deep	
ML width [μm]	19.43	19.81	18.10	18.38	16.20	16.61
Height [μm]	13.95	10.57	18.93	15.58	38.85	38.21
AP width [μm]	17.25	17.54	18.13	18.58	21.59	19.31

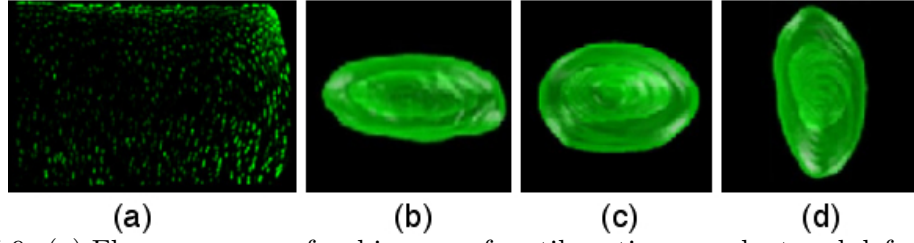


Figure 5.9: (a) Fluorescence confocal images of cartilage tissue explant and deformed chondron shapes in (b) superficial (c) middle, and (d) deep zones [30] (Reprinted from Journal of Biomechanics, 40/12, Jae Bong Choi, Inchan Youn, Li Cao, Holly A. Leddy, Christopher L. Gilchrist, Lori A. Setton and Farshid Guilak, Zonal changes in the three-dimensional morphology of the chondron under compression: The relationship among cellular, pericellular, and extracellular deformation in articular cartilage, 2596-2603., Copyright (2007), with permission from Elsevier.).

Table 5.2: Chondrocytes' morphological parameters at superficial, middle and deep zones. Left columns in each zone represent uncompressed data and right columns represent deformed shapes under 10% compressive strain, from [30].

	superficial		middle		deep	
ML width [μm]	12.34	12.58	11.49	11.66	11.69	11.73
Height [μm]	6.56	4.77	11.26	8.89	22.63	22.14

5.3 Inverse Problem

In a forward problem, the parameters and model are known and they can be used to generate model outputs. In an inverse problem, however, the parameters are unknown while observed data is available and a model can be hypothesized. The parameters can be estimated by solving an inverse problem and the resulting parameter values generate model outputs that best fit the observations in the data. In our specific context, the observations are experimental measures based on geometric characteristics of the chondron such as its deformed axial and radial coordinates and the unknown parameters are the Young's modulus and Poisson's ratio for the PCM or chondrocyte. The aim is to find a set of parameters (\hat{E} & $\hat{\nu}$) that minimize the error between the computed model output $\mathbf{X}(\hat{E}, \hat{\nu})$ and the data \mathbf{y}^d .

A least-squares formulation was used for the cost function that quantifies the error, and this cost function can be minimized using an optimization algorithm. A general

least-squares cost function J can be written as,

$$J = \sum_{i=1}^N |X_i(\hat{E}, \hat{\nu}) - y_i^d|^2, \quad (5.5)$$

The vectors \mathbf{y} and \mathbf{X} consist of multiple components and N is the total number of data points.

To solve the nonlinear optimization problem, a direct search Nelder-Mead algorithm [75] was considered because it does not require the use of a gradient of the cost function for the problem to be solved. In a direct search method, a set of trial parameter values is generated and their cost function values are compared with the best solution previously obtained. This information is then used to determine the next set of trial values. This is a convenient first choice of algorithm because the gradients may be difficult to evaluate in the absence of an analytical model. Because the gradient is not required for direct search algorithms, they are also attractive for systems with discontinuities. In practice, the simplicity of the direct search algorithms is a further advantage that makes them easier to implement.

The Nelder-Mead algorithm employs a regular simplex which moves in the direction nearest to the direction of steepest descent by replacing the highest cost vertex in the simplex with its mirror image across the face formed by the remaining vertices. A simplex is a polytope in n -dimensional space with $n + 1$ connected vertices. For example, a simplex in 2-dimensional space is a triangle, and it is a tetrahedron in 3-dimensional space. The algorithm evaluates the cost function J at the vertices of a simplex of parameters, orders the function value, replace the worst value with a new point that has a lower function value through one of the following operation: reflection, expansion or contraction. If all of these three operations fail to find a new point to replace the worst point in the simplex, then the entire simplex shrinks towards the vertex with the lowest function value. The procedure repeats until a user-prescribed error tolerance has been reached. An outline of the rules for the Nelder-Mead algorithm for function minimization is as follows and based on the specific algorithm described in [56].

1. Initialization: For a parameter set P of n dimensions, choose $n + 1$ points of simplex S to form an initial simplex in the parameter space. Evaluate J at vertices and order function values in ascending order. That is, $P_{(1)}$ represents the vertex with the lowest function value $J(P_{(1)})$, $P_{(2)}$ represents the vertex with the second lowest function value $J(P_{(2)})$ and $P_{(n+1)}$

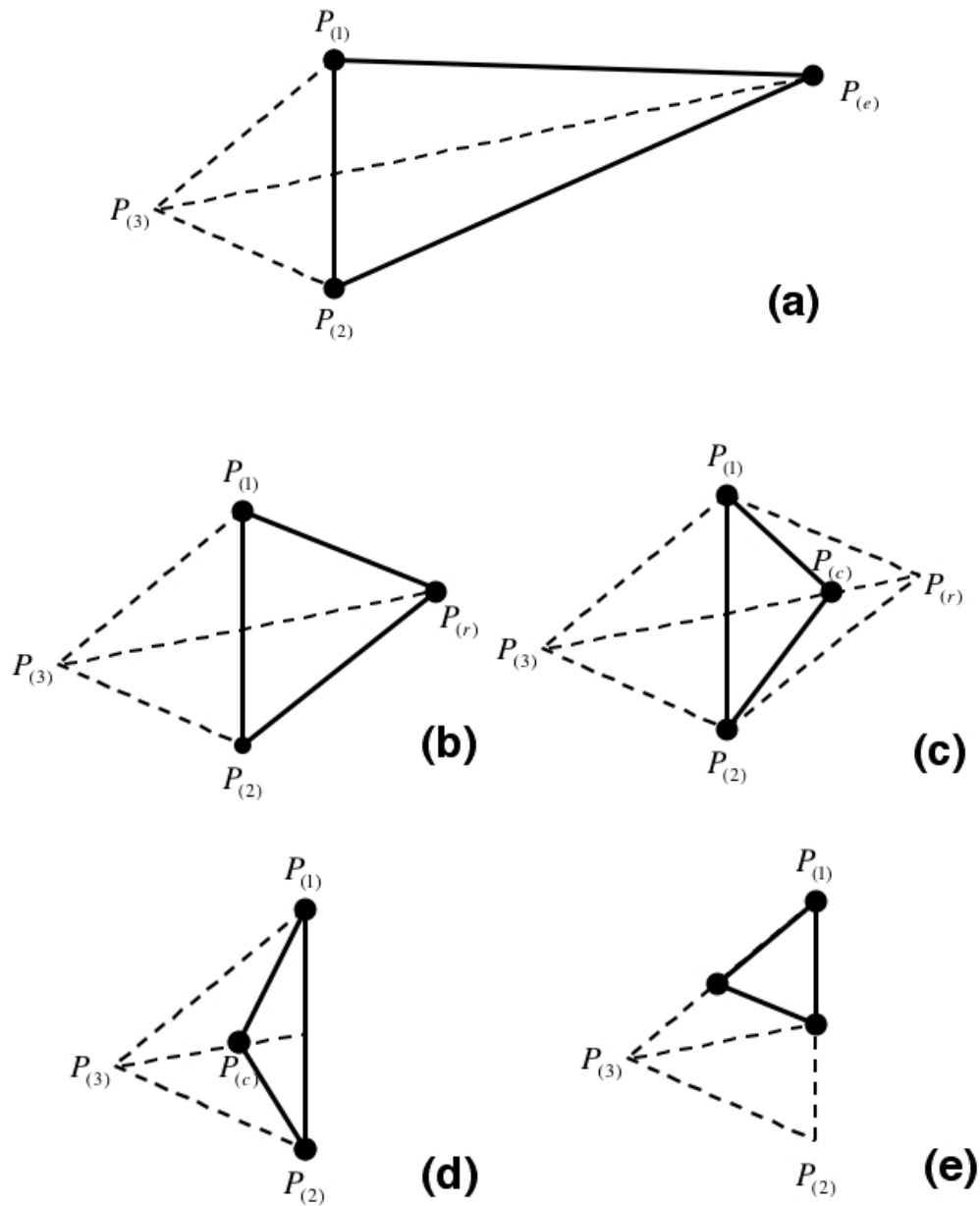


Figure 5.10: Representation of the Nelder-Mead simplex method in 2 dimensions where solid circles indicate new simplex for (a) Expansion, (b) Reflection, (c) Contraction from reflection, (d) Contraction from the worst point and (e) Shrinkage toward to the best point $P_{(1)}$.

represents the vertex with the highest function value $J(P_{(n+1)})$, yielding the ordered set $\{P_{(1)}, P_{(2)}, \dots, P_{(n+1)}\}$.

2. Simplex updates: While $|J(P_{(n+1)}) - J(P_{(1)})| > \tau$, where τ is a user specified tolerance,

(a) Find the centroid, \bar{P} of the n points: $\bar{P} = \frac{1}{n} \sum_{i=1}^n P_{(i)}$

(b) Generate a new point P_r by reflecting the $P_{(n+1)}$, $P_r = (1 + \alpha)\bar{P} - \alpha P_{(n+1)}$ where α is usually taken to be 1.

(c) Depending on the rank of \bar{P} among the n points, one of the following operations is performed on the current simplex:

– Expansion : If $J(P_r) < J(P_{(1)})$, then the reflection point P_r is extended to the point $P_e = \gamma P_r + (1 - \gamma)\bar{P}$ where $\gamma = 2$.

If $J(P_e) < J(P_{(1)})$, then P_e replaces $P_{(n+1)}$.

Else P_r replaces $P_{(n+1)}$ in the simplex.

– Reflection: If $J(P_{(1)}) \leq J(P_r) \leq J(P_{(n)})$, then P_r replaces $P_{(n+1)}$.

– Contraction: If $J(P_r) > J(P_{(n)})$, then a contraction of the simplex is attempted.

If $J(P_r) \leq J(P_{(n+1)})$, then P_r replaces $P_{(n+1)}$ before a contraction is performed.

The contraction point $P_c = \beta P_{(n+1)} + (1 - \beta)\bar{P}$, where $\beta = 0.5$.

If $J(P_c) \leq J(P_{(n+1)})$, then P_c replaces $P_{(n+1)}$.

Otherwise ($J(P_c) > J(P_{(n+1)})$), shrink the entire simplex toward to P_1 by replacing all other vertices $P_{(i)}, i = 2, \dots, (n + 1)$ by $P_{(i)} = 0.5P_{(i)} + 0.5P_{(1)}$.

(d) Return to update stage or terminate: At this time either a new point has replaced the worst point $P_{(n+1)}$ by an expansion, a reflection or a contraction, or a shrinkage occurred. The new set of points is reordered according to their respective function value $J(P_{(i)}), i = 1, \dots, (n + 1)$. If the stopping criteria is satisfied, then the algorithm terminates, otherwise it returns to step 1.

5.4 Parameter Estimation

Since the BEM model developed is restricted to the linear isotropic case, elastic properties of the PCM were estimated for experimental data at 10% macroscopic unconfined

compression in the mid-zone. Since any given set of optimal parameters only represents a local solution to the minimization problem, parameters defining this local minimum may or may not be within physiological range, and there may be multiple sets of parameters that define the same model states. Thus, it is essential to select initial parameter ranges using a priori knowledge such as literature values. Also, it is necessary to test the inverse problem for sensitivity to different sets of initial values. In this study, initial values for PCM Young's modulus were chosen and varied in the range of 10 kPa -100 kPa. For the PCM Poisson's ratio, initial values between 0 and 0.2 were considered.

Experimental data for the chondron selected from the middle zone (50% depth of the tissue) was considered. To represent the middle zone in the BEM model, the center of the microscopic domain (ECM domain) was located at 50% depth ($z = h/2 = 0.5$ mm) of the tissue, and the height of the tissue was assumed to be $h = 1$ mm. The three zone domain was modeled as an undeformed ellipsoidal cell with surrounding PCM, which was embedded in a spherical ECM with a radius of $30 \mu\text{m}$ (Figure 5.11). The heights and widths of the cell and the PCM domains were chosen based on the uncompressed data (Tables 5.1-5.2).

To make the optimization routine more robust, additional data points were generated based on the ellipsoidal heights and widths in the experimental data. Given height, h_d and width, w_d of the chondron, $N = 19$ points were generated by an ellipsoidal parameterization $(r, z) = \left(\frac{w_d}{2} \sin \theta, -\frac{h_d}{2} \cos \theta\right)$ on the chondron boundary and cell-PCM interface, respectively. The centers of these ellipses were aligned with those of the BEM model simulation (Figure 5.12). All optimization results shown employed $M = 13$ quadratic boundary elements for the ECM, the PCM and cell, respectively, with 10-point Gaussian quadrature.

5.5 Results

Analysis of the inverse problem focused on identifying PCM material properties. Material properties of the ECM and the cell were assigned to be

$$E_{ECM} = 1 \text{ MPa}, E_{cell} = 350 \text{ Pa}, \nu_{ECM} = 0.04 \text{ or } 0.12, \nu_{cell} = 0.43. \quad (5.6)$$

In (5.6), the value $\nu_{ECM} = 0.04$ was chosen since it is a representative value of the Poisson's ratio for cartilage ECM as determined by macroscopic testing of cartilage explants. However, as part of the in situ confocal microscopy study of chondron deformation [30], an

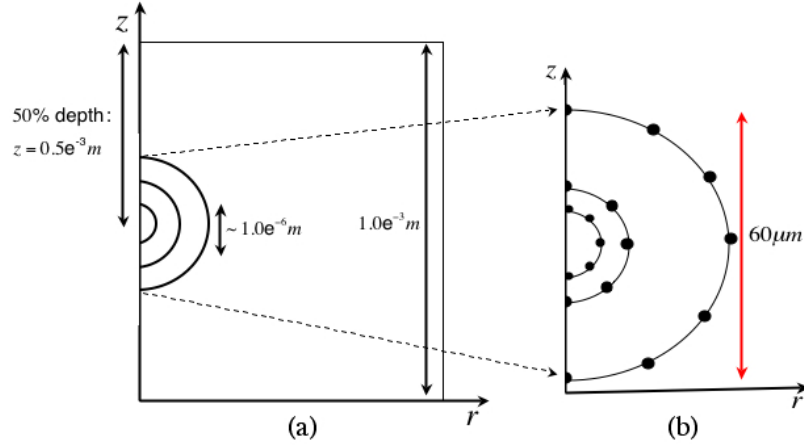


Figure 5.11: Illustration of the three-zone BEM model for simulation of chondron deformation in unconfined compression. The analytical solution (5.3-5.4) was prescribed on the outer (ECM) boundary.

estimate of the ECM Poisson's ratio for the explant under consideration was also calculated from the change in principal lengths of the chondron under deformation. For the mid-zone, the Poisson's ratio was estimated to be $\nu_{ECM} = 0.12$ [30]. Based on these observations, both values of the ECM Poisson's ratio were considered in this study, i.e., in (5.6).

To estimate the Young's modulus and Poisson's ratio of the PCM, two different cost functions were considered. First, a cost function based on deformed coordinate values of the chondron (See Figure 5.12) was considered and optimal values of E_{PCM} and ν_{PCM} were determined. Second, the cell volume data was also incorporated into the cost function with an appropriate weighting coefficient w , and new optimal values were obtained.

Estimation of Parameters from Shape of Deformed Chondron

The cost function

$$J = \sum_{(r_i, z_i) \in \Gamma_{PE}} \left(|r_i^d - r_i^m|^2 + |z_i^d - z_i^m|^2 \right) \quad (5.7)$$

was considered first for optimization to estimate E_{PCM} and ν_{PCM} with $N = 19$ points. In (5.7), the subscript d denotes data and m denotes model predictions that were obtained from the three-zone BEM model with boundary conditions (5.3)-(5.4).

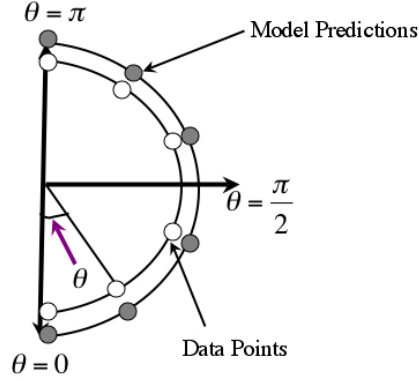


Figure 5.12: Generation of data points on the chondron boundary by parameterization of the ellipsoid as $(r, z) = \left(\frac{w_d}{2} \sin \theta, -\frac{h_d}{2} \cos \theta\right)$. The centers of the ellipses in the BEM simulation of the deformed chondrons were aligned to the corresponding centers in the experimental data.

First, this cost function was employed to estimate one parameter, E_{PCM} , and the results are shown in Tables 5.3 and 5.4 for the two values of ν_{ECM} under consideration. An illustration of agreement between deformed profiles of the chondron in the data and BEM model estimation is also shown in Figure 5.13.

Table 5.3: One parameter estimation of E_{PCM} with the cost function (5.7) and $\nu_{ECM} = \nu_{PCM} = 0.04$.

$E_{PCM}^{Initial}$ [Pa]	\hat{E}_{PCM} [Pa]	$J(\hat{E}_{PCM})$
10000-15000	44218.75	0.0101944967
20000-25000	44218.75	0.0101045921
30000-35000	44375.00	0.0100962770
40000-45000	44375.24	0.0100962682
1000 -100000	44500.00	0.0100180805

Second, a two parameter estimation of both E_{PCM} and ν_{PCM} was conducted with the same cost function (5.7), and results are shown in Table 5.5, Table 5.6, and Figure 5.14. It is noted that the estimations were not highly sensitive to the choice of initial iterates, with less sensitivity in the case $\nu_{ECM} = 0.04$. Overall, the values in Table 5.3 and Table 5.5 were consistent with previous *in vitro* measurements of E_{PCM} in the sense that values were on the order of roughly ~ 10 -100kPa [4, 6]. In particular, the one-parameter BEM model estimate of $E_{PCM} \approx 44$ kPa, was highly consistent with previous mean *in vitro* values

Table 5.4: One parameter estimation of E_{PCM} with the cost function (5.7) and $\nu_{ECM} = \nu_{PCM} = 0.12$.

$E_{PCM}^{Initial}$ [Pa]	\hat{E}_{PCM} [Pa]	$J(\hat{E}_{PCM})$
10000-15000	117281.25	0.0603402613
20000-25000	118359.37	0.0603402619
30000-35000	118281.25	0.0603401904
40000-45000	118359.38	0.0603402619
1000 -100000	118323.73	0.0603402477

for normal human cartilage PCM of 66.5kPa [4] and 38.7kPa [6]. It is also noted that the case $\nu_{ECM} = 0.04$ exhibited a significantly lower cost irrespective of whether one or two parameter estimation was used.

Table 5.5: Two parameter estimation of E_{PCM} and ν_{PCM} with the cost function (5.7) and $\nu_{ECM} = 0.04$.

$E_{PCM}^{Initial}$ [Pa]	\hat{E}_{PCM} [Pa]	$\nu_{PCM}^{Initial}$	$\hat{\nu}_{PCM}$	$J(\hat{E}_{PCM}, \hat{\nu}_{PCM})$
10000 - 20000	46816.40	0.01 - 0.1	0.164	0.0105082117
20000 - 30000	46789.57	0.01 - 0.1	0.147	0.0100044343
30000 - 40000	47578.13	0.01 - 0.1	0.166	0.0100918162
40000 - 50000	47490.23	0.01 - 0.1	0.161	0.0100777621

Table 5.6: Two parameter estimation of E_{PCM} and ν_{PCM} with the cost function (5.7) and $\nu_{ECM} = 0.12$.

$E_{PCM}^{Initial}$ [Pa]	\hat{E}_{PCM} [Pa]	$\nu_{PCM}^{Initial}$	$\hat{\nu}_{PCM}$	$J(\hat{E}_{PCM}, \hat{\nu}_{PCM})$
10000 - 20000	141750.00	0.01 - 0.1	0.002	0.04213600
20000 - 30000	125297.85	0.01 - 0.1	0.003	0.05140625
30000 - 40000	125120.30	0.01 - 0.1	0.004	0.04996874
40000 - 50000	119941.40	0.01 - 0.1	0.005	0.05014203

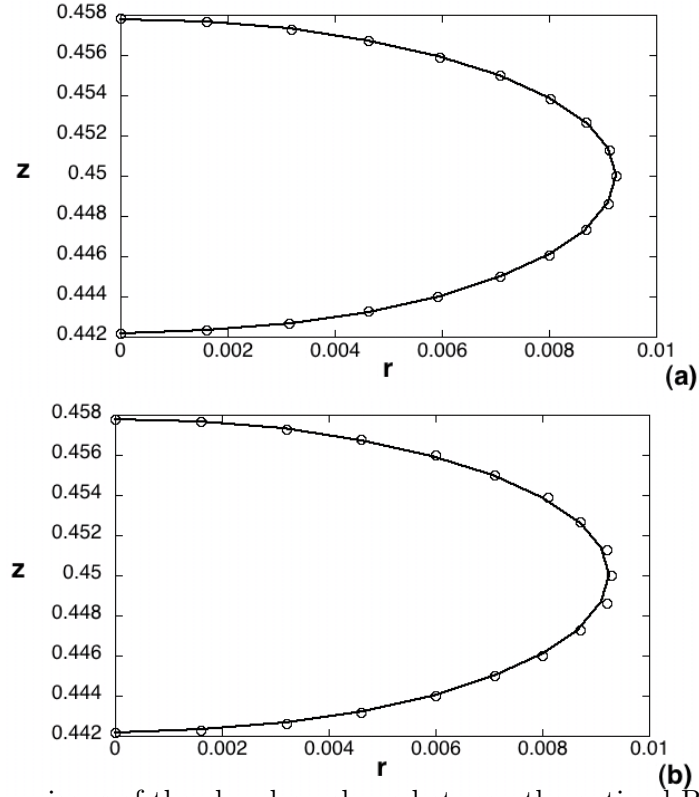


Figure 5.13: Comparisons of the chondron shape between the optimal BEM model prediction (circles) with estimated E_{PCM} and the experimental data (solid line) in the case of one parameter estimation: (a) $\hat{E}_{PCM} = 44.375$ kPa from Table 5.3 and (b) $\hat{E}_{PCM} = 118.28$ kPa from Table 5.4.

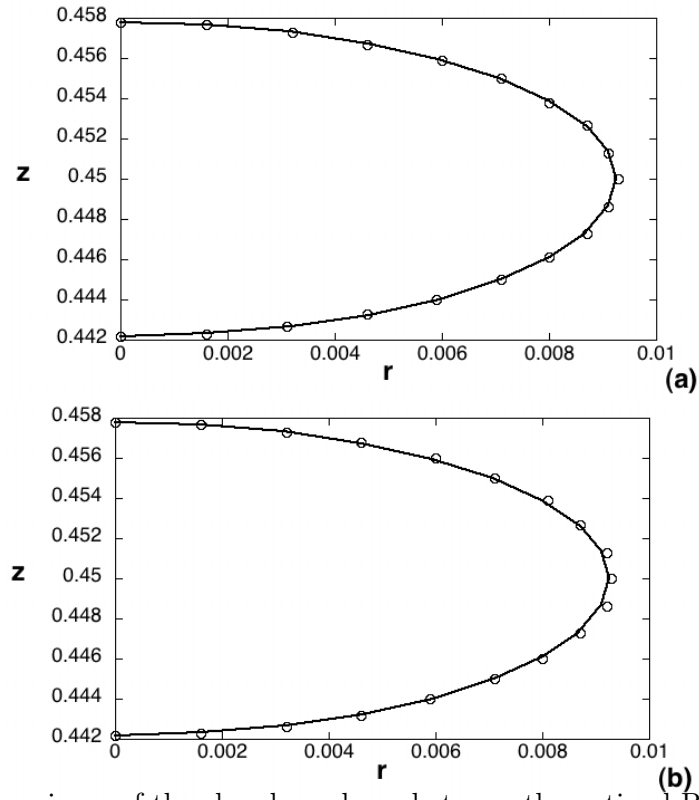


Figure 5.14: Comparisons of the chondron shape between the optimal BEM model prediction (circle) with estimated E_{PCM} and ν_{PCM} and the experimental data (solid line) in the case of two parameter estimation: (a) $\hat{E}_{PCM} = 47.58$ kPa and $\hat{\nu}_{PCM} = 0.166$ from Table 5.5 and (b) $\hat{E}_{PCM} = 125.30$ kPa and $\hat{\nu}_{PCM} = 0.003$ from Table 5.6.

Estimation of Parameters from Shape of Deformed Chondron and Cell Volume

Based on mean volume data for the deformed shape of the cell, a new cost function

$$J = w|V^d - V^m|^2 + \sum_{(r_i, z_i) \in \Gamma_{PE}} \left(|r_i^d - r_i^m|^2 + |z_i^d - z_i^m|^2 \right), \quad (5.8)$$

was also considered, where w is a scaling coefficient chosen to be 0.01, and a cell volume term was added to (5.7).

The Young's modulus and the Poisson's ratio were estimated with the new cost function (5.8) and results are shown in Tables 5.7, Table 5.8, and Figure 5.15. As compared to the original cost function in (5.7), optimal values of E_{PCM} in the case $\nu_{ECM} = 0.04$ were more sensitive to the initial iterates. However, optimal E_{PCM} values were reasonably consistent (53.4-58.2kPa vs. 46.8-47.6kPa) when compared to the previous two-parameter estimation. In the case $\nu_{ECM} = 0.12$, optimal E_{PCM} values were significantly lower with use of the new cost function (83.1-84.9kPa vs. 125.1-141.8kPa). While these values are closer to previously measured in vitro values of E_{PCM} , it is noted that, when using (5.8), the cost was significantly higher for the case $\nu_{ECM} = 0.12$.

Table 5.7: Two parameter estimation of E_{PCM} and ν_{PCM} with the cost function (5.8) and $\nu_{ECM} = 0.04$.

$E_{PCM}^{Initial}$ [Pa]	\hat{E}_{PCM} [Pa]	$\nu_{PCM}^{Initial}$	$\hat{\nu}_{PCM}$	$J(\hat{E}_{PCM}, \hat{\nu}_{PCM})$
10000 - 20000	58193.53	0.01 - 0.1	0.340	0.0104067326
20000 - 30000	53447.26	0.01 - 0.1	0.353	0.0108026931
30000 - 40000	54687.50	0.01 - 0.1	0.359	0.0108100616
40000 - 50000	52875.04	0.01 - 0.1	0.343	0.0109604540

Table 5.8: Two parameter estimation of E_{PCM} and ν_{PCM} with the cost function (5.8) and $\nu_{ECM} = 0.12$.

$E_{PCM}^{Initial}$ [Pa]	\hat{E}_{PCM} [Pa]	$\nu_{PCM}^{Initial}$	$\hat{\nu}_{PCM}$	$J(\hat{E}_{PCM}, \hat{\nu}_{PCM})$
10000 - 20000	83067.71	0.01 - 0.1	0.388	0.1177000656
20000 - 30000	84860.01	0.01 - 0.1	0.390	0.1178240475
30000 - 40000	81471.99	0.01 - 0.1	0.386	0.1177322050
40000 - 50000	83069.92	0.01 - 0.1	0.388	0.1176807719

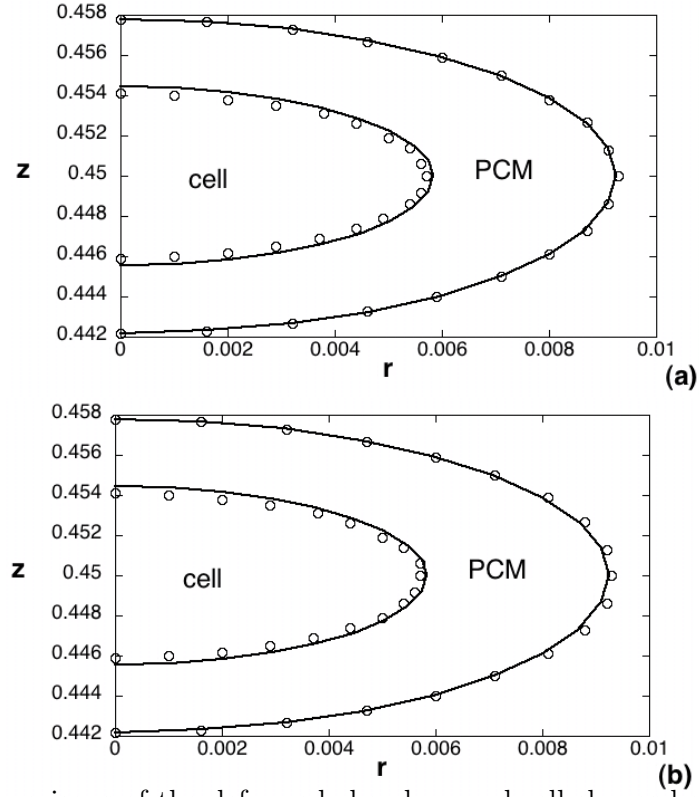


Figure 5.15: Comparisons of the deformed chondron and cell shapes between the optimal BEM model prediction (circles), with estimated values of E_{PCM} and ν_{PCM} , and the experimental data (solid line) based on the cost function (5.8): (a) $\hat{E}_{PCM} = 53.4$ kPa and $\hat{\nu}_{PCM} = 0.353$ from Table 5.7 and (b) $\hat{E}_{PCM} = 84.9$ kPa and $\hat{\nu}_{PCM} = 0.386$ from Table 5.8.

5.6 Discussion

The axisymmetric elastic BEM model that was developed for domains with internal interfaces was applied to analyze confocal microscopy data for in situ deformation of chondrons within the extracellular matrix of a cartilage explant. Overall, estimated values of E_{PCM} were more consistent with in vitro measurements in the case $\nu_{ECM} = 0.04$. Noting that $\nu_{ECM} = 0.04$ is a common value based on macroscopic analysis of ECM deformation in cartilage explants, our findings suggest that the method for estimation of $\nu_{ECM} = 0.12$ in the confocal study may be inconsistent with the assumption of our multiscale model. In particular, the confocal study estimated this value based on the deformed shape the chondron thus, inherently, assuming that the chondron was comprised of ECM material. In reality, the chondron is a soft inclusion that perturbs the local biomechanical environment around the cells of articular cartilage. In our multiscale BEM models, the ECM properties are used, exclusively, in enforcement of the far field boundary conditions, i.e., away from the location of the cell and PCM regions. We hypothesize that this observation is the primary reason why predictions of E_{PCM} for the case $\nu_{ECM} = 0.04$ are generally more consistent with the previous in vitro studies.

However, it is also noted that there may be inherent differences between in vitro and in situ values of PCM stiffness due to several factors. One factor is the species from which the tissue explant was extracted, which was porcine in the confocal study and human for the in vitro studies [4, 6]. Furthermore, within the ECM of articular cartilage, the detailed structure of attachment between the PCM and the ECM is not well understood. Thus, a chondron from the same species and site may exhibit inherent differences in PCM stiffness between the in vitro and in situ environments.

This study represents the first application of a computational model to estimate in situ material properties of the cartilage ECM. While, excellent results were obtained with two parameter estimation, future studies could consider the development of extended models, cost functions and optimization algorithms for simultaneous estimation of cell and PCM material properties based on the in situ confocal experiment.

Other direct search methods, such as multidirectional search method or the Hooke-Jeeves algorithm can also be considered. The multidirectional search method [20] makes a new simplex congruent to the previous simplex. The method is different in that it generates

whole points to expand simplex. Because of this restriction of congruence, the method is more stable and known to be convergent, which means that only a finite number of function evaluations are needed to find its minimum. The Hooke-Jeeves algorithm [52] evaluates the cost function on a stencil and the cost function value is used to find the search direction. At each iteration, the algorithm begins with a base point and pattern size. As in [52], the cost function is sampled at successive perturbations of the base point in the search direction $\{\mathbf{v}_j\}$, where \mathbf{v}_j is the j th column of a direction matrix \mathbf{I} . The entire pattern of points is shifted to a new location, which is determined by extrapolating the line from the old base point in the m dimensional parameter space to the new base point. The step sizes in this process are constantly adjusted. This method is usually quite effective, and can be considered if the simplex methods fail to produce reasonable estimates.

When the cost function is easily differentiable, a gradient-based optimization method can be used. These methods use the gradient and Hessian matrix of the cost function to locate the local minimum, and several variants on standard iterative Newton's method are presented in [56]. In gradient based methods, the quadratic model

$$m(\mathbf{x}) = J(\mathbf{x}_{(n)}) + (\nabla J(\mathbf{x}_{(n)}))^T (\mathbf{x} - \mathbf{x}_{(n)}) + \frac{1}{2} (\mathbf{x} - \mathbf{x}_{(n)})^T \nabla^2 J(\mathbf{x}_{(n)}) (\mathbf{x} - \mathbf{x}_{(n)}) \quad (5.9)$$

is considered. For a minimizer $\hat{\mathbf{x}}$, the gradient

$$\nabla J(\hat{\mathbf{x}}) = \mathbf{0}, \quad (5.10)$$

and $\nabla^2 J(\hat{\mathbf{x}})$ is positive definite. Via a Newton's method, the new candidate set of parameters $\mathbf{x}_{(n+1)}$ is determined from the current set $\mathbf{x}_{(n)}$ by the relation

$$\mathbf{x}_{(n+1)} = \mathbf{x}_{(n)} - \nabla^2 J(\mathbf{x}_{(n)})^{-1} \nabla J(\mathbf{x}_{(n)}). \quad (5.11)$$

The Gauss-Newton algorithm uses an approximation for the Hessian $\nabla^2 J$ and the method is usually employed for the nonlinear least square problem. Another variation called the Levenberg-Marquardt algorithm is especially useful when the initial iterate happens to be far from the minimizer, and the non-negative regularization damping parameter is added to the step. The theory predicts the convergence of the method [56] when initial parameter estimates are far from the solution and rapid convergence when near the solution.

Lastly, the implicit filtering method [56] is a steepest descent algorithm for a noisy cost function with bound constraint. The method is intended for the problems with many

local minima. The algorithm uses difference gradients and reduces the difference increment as the optimization progresses. The method uses the central difference gradient, $\nabla_h J(\mathbf{x}_{(n)})$ as the basis for a Newton's method, and finds the steepest descent direction by identifying the least integer $0 \leq m \leq \alpha_{max}$ such that the equation

$$J(\mathbf{x}_{(n)} - \lambda \nabla_h J(\mathbf{x}_{(n)})) - J(\mathbf{x}_{(n)}) < -\alpha \lambda \|\nabla_h J(\mathbf{x}_{(n)})\|^2, \quad \alpha > 0, \quad (5.12)$$

holds for $\lambda = \beta^m$. Then, the λ is employed to update parameter estimates, via the relation $\mathbf{x}_{(n+1)} = \mathbf{x}_{(n)} - \lambda \nabla_h J(\mathbf{x}_{(n)})$.

The experimental data for in situ chondron deformation with a cartilage explant leads to a novel parameter estimation problem. The results presented in this chapter indicate that algorithms based on one or two-parameter estimation yield estimates for PCM elastic material properties that are highly consistent with previous in vitro studies. In future studies, the inverse BEM method can be extended to, simultaneously, estimate both PCM and cell elastic properties. However, achieving this goal will require careful consideration of the optimal combination of experimental data design, and choice of both the cost function and the optimization algorithm.

Bibliography

- [1] *Comsol Multiphysics Modeling Guide (version 3.2)- Chapter 10. The Weak Form.* COMSOL AB, Burlington, MA, 2005.
- [2] *Comsol Multiphysics User's Guide (version 3.2) - Chapter 6. Solving the Model.* COMSOL AB, Burlington, MA, 2005.
- [3] M. Abramowitz and I. A. Stegun. *Handbook of mathematical functions with formulas, graphs, and mathematical tables.* U.S. Govt. Print. Off., Washington, 1964.
- [4] L. G. Alexopoulos, M. A. Haider, T. P. Vail, and F. Guilak. Alterations in the mechanical properties of the human chondrocyte pericellular matrix with osteoarthritis. *J Biomech Eng*, 125(3):323–333, 2003.
- [5] L. G. Alexopoulos, L. A. Setton, and F. Guilak. The biomechanical role of the chondrocyte pericellular matrix in articular cartilage. *Acta Biomater*, 1(3):317–325, 2005.
- [6] L. G. Alexopoulos, G. M. Williams, M. L. Upton, L. A. Setton, and F. Guilak. Osteoarthritic changes in the biphasic mechanical properties of the chondrocyte pericellular matrix in articular cartilage. *J Biomech*, 38(3):509–517, 2005.
- [7] E. Almeida and R. Spilker. Mixed and penalty finite element models for the nonlinear behavior of biphasic soft tissues in finite deformation: Part i - alternate formulations. *Comput Methods Biomech Biomed Engin*, 1(1):25–46, 1997.
- [8] E. Almeida and R. Spilker. Mixed and penalty finite element models for the nonlinear behavior of biphasic soft tissues in finite deformation: Part ii - nonlinear examples. *Comput Methods Biomech Biomed Engin*, 1(2):151–170, 1998.

- [9] P. Angele, D. Schumann, M. Angele, B. Kinner, C. Englert, R. Hente, B. Fuchtmeyer, M. Nerlich, C. Neumann, and R. Kujat. Cyclic, mechanical compression enhances chondrogenesis of mesenchymal progenitor cells in tissue engineering scaffolds. *Biorheology*, 41(3-4):335–346, 2004.
- [10] J. H. Argyris. *Energy theorems and structural analysis*. London, 1960.
- [11] C. G. Armstrong, W. M. Lai, and V. C. Mow. An analysis of the unconfined compression of articular cartilage. *J Biomech Eng*, 106(2):165–173, 1984.
- [12] G. A. Ateshian, W. H. Warden, J. J. Kim, R. P. Grelsamer, and V. C. Mow. Finite deformation biphasic material properties of bovine articular cartilage from confined compression experiments. *J Biomech*, 30(11-12):1157–1164, 1997.
- [13] K. A. Athanasiou, M. P. Rosenwasser, J. A. Buckwalter, T. I. Malinin, and V. C. Mow. Interspecies comparisons of in situ intrinsic mechanical properties of distal femoral cartilage. *J Orthop Res*, 9(3):330–340, 1991.
- [14] A. A. Bakr. *The boundary integral equation method in axisymmetric stress analysis problems*, volume 14. Springer-Verlag, Berlin, 1986.
- [15] K. J. Bathe. *Numerical Methods in Finite Element Analysis*. Prentice Hall Inc., 1996.
- [16] D. E. Beskos. *Boundary element methods in mechanics*, volume v. 3. North-Holland, Amsterdam, 1987.
- [17] D. E. Beskos. *Boundary element methods in structural analysis*. ASCE, New York, N.Y., 1989.
- [18] D. E. Beskos. *Boundary element analysis of plates and shells*. Springer-Verlag, Berlin, 1991.
- [19] E. J. Blain, S. J. Gilbert, R. J. Wardale, S. J. Capper, D. J. Mason, and V. C. Duance. Up-regulation of matrix metalloproteinase expression and activation following cyclical compressive loading of articular cartilage in vitro. *Arch Biochem Biophys*, 396(1):49–55, 2001.

- [20] D. M. Bortz and C. T. Kelley. The simplex gradient and noisy optimization problems. In *Computational Methods in Optimal Design and Control*, pages 77–90, 1998.
- [21] C. A. Brebbia and P. W. Partridge. *Boundary elements in fluid dynamics*. Computational Mechanics Publications, Southampton, 1992.
- [22] P. N. Brown, A. C. Hindmarsh, and L. R. Petzold. Using krylov methods in the solution of large-scale differential algebraic systems. *SIAM J Sci Comput*, 15(6):1467–1488, 1994.
- [23] M. D. Buschmann, Y. A. Gluzband, A. J. Grodzinsky, and E. B. Hunziker. Mechanical compression modulates matrix biosynthesis in chondrocyte/agarose culture. *J Cell Sci*, 108 (Pt 4):1497–1508, 1995.
- [24] M. D. Buschmann, Y. J. Kim, M. Wong, E. Frank, E. B. Hunziker, and A. J. Grodzinsky. Stimulation of aggrecan synthesis in cartilage explants by cyclic loading is localized to regions of high interstitial fluid flow. *Arch Biochem Biophys*, 366(1):1–7, 1999.
- [25] N. O. Chahine, C. T. Hung, and G. A. Ateshian. In-situ measurements of chondrocyte deformation under transient loading. *Eur Cell Mater*, 13:100–111, 2007.
- [26] B. Chan, P. S. Donzelli, and R. L. Spilker. A mixed-penalty biphasic finite element formulation incorporating viscous fluids and material interfaces. *Ann Biomed Eng*, 28(6):589–597, 2000.
- [27] S. Chen, B. Merriman, S. Osher, and P. Smereka. A simple level set method for solving stefan problems. *J Comput Phys*, 135(1):8 – 29, 1997.
- [28] S. S. Chen, Y. H. Falcovitz, R. Schneiderman, A. Maroudas, and R. L. Sah. Depth-dependent compressive properties of normal aged human femoral head articular cartilage: relationship to fixed charge density. *Osteoarthr Cartilage*, 9(6):561–569, 2001.
- [29] Y. K. Cheung and M. F. Yeo. *A practical introduction to finite element analysis*. A Pitman International Text, 1979.

- [30] J. B. Choi, I. Youn, L. Cao, H. A. Leddy, C. L. Gilchrist, L. A. Setton, and F. Guilak. Zonal changes in the three-dimensional morphology of the chondron under compression: the relationship among cellular, pericellular, and extracellular deformation in articular cartilage. *J Biomech*, 40(12):2596–2603, 2007.
- [31] T. T. Chowdhury, D. L. Bader, and D. A. Lee. Dynamic compression counteracts il-1 β induced inos and cox-2 activity by human chondrocytes cultured in agarose constructs. *Biorheology*, 43(3):413–429, 2006.
- [32] T. T. Chowdhury, D. L. Bader, J. C. Shelton, and D. A. Lee. Temporal regulation of chondrocyte metabolism in agarose constructs subjected to dynamic compression. *Arch Biochem Biophys*, 417(1):105–111, 2003.
- [33] R. D. Ciskowski and C. A. Brebbia. *Boundary element methods in acoustics*. International series on computational engineering. Computational Mechanics Publications, Southampton, 1991.
- [34] T. Davisson, S. Kunig, A. Chen, R. Sah, and A. Ratcliffe. Static and dynamic compression modulate matrix metabolism in tissue engineered cartilage. *J Orthop Res*, 20(4):842–848, 2002.
- [35] T. L. H. Donahue, M. L. Hull, M. M. Rashid, and C. R. Jacobs. A finite element model of the human knee joint for the study of tibio-femoral contact. *J Biomech Eng*, 124(3):273–280, 2002.
- [36] J. Donea and A. Huerta. *Finite element methods for flow problems*. John Wiley and Sons Inc., 2003.
- [37] S. H. Elder, S. A. Goldstein, J. H. Kimura, L. J. Soslowsky, and D. M. Spengler. Chondrocyte differentiation is modulated by frequency and duration of cyclic compressive loading. *Ann Biomed Eng*, 29(6):476–482, 2001.
- [38] R. P. Fedkiw, T. Aslam, and S. J. Xu. The ghost fluid method for deflagration and detonation discontinuities. *J Comput Phys*, 154(2):393 – 427, 1999.
- [39] P. M. Freeman, R. N. Natarajan, J. H. Kimura, and T. P. Andriacchi. Chondrocyte cells respond mechanically to compressive loads. *J Orthop Res*, 12(3):311–320, 1994.

- [40] A. A. Goldsmith, A. Hayes, and S. E. Clift. Application of finite elements to the stress analysis of articular cartilage. *Med Eng Phys*, 18(2):89–98, 1996.
- [41] W. Y. Gu, W. M. Lai, and V. C. Mow. Transport of fluid and ions through a porous-permeable charged-hydrated tissue, and streaming potential data on normal bovine articular cartilage. *J Biomech*, 26(6):709–723, 1993.
- [42] M. Guiggiani and P. Casalini. The numerical implementation of bem for axisymmetric elasticity. In *Proceedings of the 8th International Conference*, volume 2, pages 695–705, 1986.
- [43] M. Guiggiani and P. Casalini. Direct computatin of cauchy principal value integrals in advanced boundary elements. *Int J Numer Meth Eng*, 24:1711–1720, 1987.
- [44] F. Guilak. The deformation behavior and viscoelastic properties of chondrocytes in articular cartilage. *Biorheology*, 37(1):27–44, 2000.
- [45] F. Guilak, L. G. Alexopoulos, M. A. Haider, H. P. Ting-Beall, and L. A. Setton. Zonal uniformity in mechanical properties of the chondrocyte pericellular matrix: micropipette aspiration of canine chondrons isolated by cartilage homogenization. *Ann Biomed Eng*, 33(10):1312–1318, 2005.
- [46] F. Guilak, W. R. Jones, H. P. Ting-Beall, and G. M. Lee. The deformation behavior and mechanical properties of chondrocytes in articular cartilage. *Osteoarthr Cartilage*, 7(1):59–70, 1999.
- [47] F. Guilak and V. C. Mow. The mechanical environment of the chondrocyte: a biphasic finite element model of cell-matrix interactions in articular cartilage. *J Biomech*, 33(12):1663–1673, 2000.
- [48] F. Guilak, A. Ratcliffe, and V. C. Mow. Chondrocyte deformation and local tissue strain in articular cartilage: a confocal microscopy study. *J Orthop Res*, 13(3):410–421, 1995.
- [49] M. A. Haider. A radial biphsic model for local cell-matrix mechanics in articular cartilage. *SIAM J Appl Math*, 64:1588–1608, 2004.

- [50] M. A. Haider and F. Guilak. An axisymmetric boundary integral model for assessing elastic cell properties in the micropipette aspiration contact problem. *J Biomech Eng*, 124(5):586–595, 2002.
- [51] W. S. Hall and G. Oliveto. *Boundary element methods for soil-structure interaction*. Kluwer Academic Publishers, Dordrecht, The Netherlands, 2003.
- [52] R. Hooke and T. Jeeves. Direct search solution of numerical and statistical problems. *J Assoc Comput Mach*, 8:212 – 229, 1961.
- [53] R. Y. Hori and L. F. Mockros. Indentation tests of human articular cartilage. *J Biomech*, 9(4):259–268, 1976.
- [54] C. T. Hung, R. L. Mauck, C. C. B. Wang, E. G. Lima, and G. A. Ateshian. A paradigm for functional tissue engineering of articular cartilage via applied physiologic deformational loading. *Ann Biomed Eng*, 32(1):35–49, 2004.
- [55] W. R. Jones, H. P. Ting-Beall, G. M. Lee, S. S. Kelley, R. M. Hochmuth, and F. Guilak. Alterations in the young’s modulus and volumetric properties of chondrocytes isolated from normal and osteoarthritic human cartilage. *J Biomech*, 32(2):119–127, 1999.
- [56] C. T. Kelley. *Iterative methods for optimization*. SIAM, Philadelphia, 1999.
- [57] M. M. Knight, J. van de Breevaart Bravenboer, D. A. Lee, G. J. V. M. van Osch, H. Weinans, and D. L. Bader. Cell and nucleus deformation in compressed chondrocyte-alginate constructs: temporal changes and calculation of cell modulus. *Biochim Biophys Acta*, 1570(1):1–8, 2002.
- [58] E. J. Koay, A. C. Shieh, and K. A. Athanasiou. Creep indentation of single cells. *J Biomech Eng*, 125(3):334–341, 2003.
- [59] W. M. Lai, J. S. Hou, and V. C. Mow. A triphasic theory for the swelling and deformation behaviors of articular cartilage. *J Biomech Eng*, 113(3):245–258, 1991.
- [60] D. A. Lee and D. L. Bader. Compressive strains at physiological frequencies influence the metabolism of chondrocytes seeded in agarose. *J Orthop Res*, 15(2):181–188, 1997.

- [61] D. A. Lee, T. Noguchi, S. P. Freat, P. Lees, and D. L. Bader. The influence of mechanical loading on isolated chondrocytes seeded in agarose constructs. *Biorheology*, 37(1-2):149–161, 2000.
- [62] G. M. Lee, T. A. Paul, M. Slabaugh, and S. S. Kelley. The incidence of enlarged chondrons in normal and osteoarthritic human cartilage and their relative matrix density. *Osteoarthr Cartilage*, 8(1):44–52, 2000.
- [63] R. J. LeVeque and Z. Li. The immersed interface method for elliptic equations with discontinuous coefficients and singular sources. *SIAM J Numer Anal*, 31:1019 – 1044, 1994.
- [64] R. W. Lewis and B. A. Schrefler. *The finite element method in the deformation and consolidation of porous media*. John Wiley and Sons Inc, 1987.
- [65] K. W. Li, A. K. Williamson, A. S. Wang, and R. L. Sah. Growth responses of cartilage to static and dynamic compression. *Clin Orthop Relat Res*, 391 Suppl:S34–48, 2001.
- [66] Z. Li. Immersed interface methods for moving interface problems. *Numer Algorithms*, 14(4):269 – 293, 1997.
- [67] Z. Li. An overview of the immersed interface method and its applications. *Taiwanese J. Math.*, 7(1):1 –49, 2003.
- [68] Z. Li and K. Ito. *The immersed interface method : numerical solutions of PDEs involving interfaces and irregular domains*. SIAM, Society for Industrial and Applied Mathematics, Philadelphia, 2006.
- [69] E. N. Marieb. *Human anatomy & physiology*. Benjamin Cummings, San Francisco, 5th ed edition, 2001.
- [70] R. L. Mauck, S. L. Seyhan, G. A. Ateshian, and C. T. Hung. Influence of seeding density and dynamic deformational loading on the developing structure/function relationships of chondrocyte-seeded agarose hydrogels. *Ann Biomed Eng*, 30(8):1046–1056, 2002.

- [71] D. M. McQueen, C. S. Peskin, and L. Zhu. The immersed boundary method for incompressible fluid-structure interaction. In *Computational fluid and solid mechanics*, volume 1, pages 26–30, 2001.
- [72] V. C. Mow and X. E. Guo. Mechano-electrochemical properties of articular cartilage: their inhomogeneities and anisotropies. *Annu Rev Biomed Eng*, 4:175–209, 2002.
- [73] V. C. Mow, S. C. Kuei, W. M. Lai, and C. G. Armstrong. Biphasic creep and stress relaxation of articular cartilage in compression: Theory and experiments. *J Biomech Eng*, 102(1):73–84, 1980.
- [74] V. C. Mow, A. Ratcliffe, and A. R. Poole. Cartilage and diarthrodial joints as paradigms for hierarchical materials and structures. *Biomaterials*, 13(2):67–97, 1992.
- [75] J. Nelder and R. Mead. A simplex method for function minimization. *Comput J*, 7:308–313, 1965.
- [76] S. Osher and R. P. Fedkiw. Level set methods: an overview and some recent results. *J Comput Phys*, 169(2):463 – 502, 2001.
- [77] M. J. Palmoski and K. D. Brandt. Effects of static and cyclic compressive loading on articular cartilage plugs in vitro. *Arthritis Rheum*, 27(6):675–681, 1984.
- [78] C. S. Peskin. Two examples of mathematics and computing in the biological sciences: blood flow in the heart and molecular dynamics. *American Mathematical Society centennial publications*, 2:395 – 415, 1992.
- [79] C. S. Peskin. The immersed boundary method. *Acta Numer*, 11:479 – 517, 2002.
- [80] J. L. Piscoya, B. Fermor, V. B. Kraus, T. V. Stabler, and F. Guilak. The influence of mechanical compression on the induction of osteoarthritis-related biomarkers in articular cartilage explants. *Osteoarthritis Cartilage*, 13(12):1092–1099, 2005.
- [81] C. A. Poole, S. Ayad, and R. T. Gilbert. Chondrons from articular cartilage. v. immunohistochemical evaluation of type vi collagen organisation in isolated chondrons by light, confocal and electron microscopy. *J Cell Sci*, 103 (Pt 4):1101–1110, 1992.

- [82] H. Power. *BE applications in fluid mechanics*, volume v. 4. Computational Mechanics Publications, Southampton, UK, 1995.
- [83] T. M. Quinn, A. J. Grodzinsky, M. D. Buschmann, Y. J. Kim, and E. B. Hunziker. Mechanical compression alters proteoglycan deposition and matrix deformation around individual cells in cartilage explants. *J Cell Sci*, 111 (Pt 5):573–583, 1998.
- [84] F. Rizzo. An integral equation approach to boundary value problems of classic elastostatics. *The Quarterly of Applied Mathematics*, 25:83 – 95, 1967.
- [85] A. M. Roma, C. S. Peskin, and M. J. Berger. An adaptive version of an adaptive version of the immersed boundary method. *J Comput Phys*, 153(2):509 – 534, 1999.
- [86] R. L. Sah, Y. J. Kim, J. Y. Doong, A. J. Grodzinsky, A. H. Plaas, and J. D. Sandy. Biosynthetic response of cartilage explants to dynamic compression. *J Orthop Res*, 7(5):619–636, 1989.
- [87] K. Sauerland, R. X. Raiss, and J. Steinmeyer. Proteoglycan metabolism and viability of articular cartilage explants as modulated by the frequency of intermittent loading. *Osteoarthr Cartilage*, 11(5):343–350, 2003.
- [88] R. M. Schinagl, D. Gurskis, A. C. Chen, and R. L. Sah. Depth-dependent confined compression modulus of full-thickness bovine articular cartilage. *J Orthop Res*, 15(4):499–506, 1997.
- [89] J. A. Sethian. Theory, algorithms, and applications of level set methods for propagating interfaces. *Acta Numer*, 5:309 – 395, 1996.
- [90] R. L. Spilker, E. S. de Almeida, and P. S. Donzelli. Finite element methods for the biomechanics of soft hydrated tissues: nonlinear analysis and adaptive control of meshes. *Crit Rev Biomed Eng*, 20(3-4):279–313, 1992.
- [91] R. L. Spilker and T. A. Maxian. A mixed-penalty finite element formulation of the linear biphasic theory for soft tissues. *Int J for Numer Meth Eng*, 30:1063–1082, 1990.
- [92] R. L. Spilker, J. K. Suh, and V. C. Mow. Effects of friction on the unconfined compressive response of articular cartilage: a finite element analysis. *J Biomech Eng*, 112(2):138–146, 1990.

- [93] R. L. Spilker, J. K. Suh, and V. C. Mow. A finite element analysis of the indentation stress-relaxation response of linear biphasic articular cartilage. *J Biomech Eng*, 114(2):191–201, 1992.
- [94] J. Steinmeyer, S. Daufeldt, and D. A. Kalbhen. The proteoglycan metabolism, morphology and viability of articular cartilage treated with a synthetic matrix metalloproteinase inhibitor. *Res Exp Med (Berl)*, 197(2):63–79, 1997.
- [95] J. Steinmeyer and S. Knue. The proteoglycan metabolism of mature bovine articular cartilage explants superimposed to continuously applied cyclic mechanical loading. *Biochem Biophys Res Commun*, 240(1):216–221, 1997.
- [96] R. A. Stockwell. *Biology of cartilage cells*, volume 7. Cambridge University Press, Cambridge, 1979.
- [97] A. H. Stroud and D. Secrest. *Gaussian quadrature formulas*. Prentice-Hall, Englewood Cliffs, N.J., 1966.
- [98] J. K. Suh. Dynamic unconfined compression of articular cartilage under a cyclic compressive load. *Biorheology*, 33(4):289–304, 1996.
- [99] J. K. Suh and S. Bai. Finite element formulation of biphasic poroviscoelastic model for articular cartilage. *J Biomech Eng*, 120(2):195–201, 1998.
- [100] J. K. Suh, Z. Li, and S. L. Woo. Dynamic behavior of a biphasic cartilage model under cyclic compressive loading. *J Biomech*, 28(4):357–364, 1995.
- [101] F. Thomasset. *Implementation of finite element methods for Navier-Stokes equations*. Springer Series in Computational Physics., 1981.
- [102] P. A. Torzilli, R. Grigienė, C. Huang, S. M. Friedman, S. B. Doty, A. L. Boskey, and G. Lust. Characterization of cartilage metabolic response to static and dynamic stress using a mechanical explant test system. *J Biomech*, 30(1):1–9, 1997.
- [103] W. R. Trickey, G. M. Lee, and F. Guilak. Viscoelastic properties of chondrocytes from normal and osteoarthritic human cartilage. *J Orthop Res*, 18(6):891–898, 2000.

- [104] K. Un and R. L. Spilker. A penetration-based finite element method for hyperelastic 3d biphasic tissues in contact: Part 1—derivation of contact boundary conditions. *J Biomech Eng*, 128(1):124–130, 2006.
- [105] K. Un and R. L. Spilker. A penetration-based finite element method for hyperelastic 3d biphasic tissues in contact. part ii: finite element simulations. *J Biomech Eng*, 128(6):934–942, 2006.
- [106] S. D. Waldman, D. C. Couto, M. D. Gryn timer, R. M. Pilliar, and R. A. Kandel. A single application of cyclic loading can accelerate matrix deposition and enhance the properties of tissue-engineered cartilage. *Osteoarthr Cartilage*, 14(4):323–330, 2006.
- [107] S. D. Waldman, C. G. Spiteri, M. D. Gryn timer, R. M. Pilliar, J. Hong, and R. A. Kandel. Effect of biomechanical conditioning on cartilaginous tissue formation in vitro. *J Bone Joint Surg Am*, 85-A Suppl 2:101–105, 2003.
- [108] S. D. Waldman, C. G. Spiteri, M. D. Gryn timer, R. M. Pilliar, and R. A. Kandel. Long-term intermittent compressive stimulation improves the composition and mechanical properties of tissue-engineered cartilage. *Tissue Eng*, 10(9-10):1323–1331, 2004.
- [109] M. D. Warner, W. R. Taylor, and S. E. Clift. Finite element biphasic indentation of cartilage: a comparison of experimental indenter and physiological contact geometries. *Proc Inst Mech Eng [H]*, 215(5):487–496, 2001.
- [110] J. S. Wayne, S. L. Woo, and M. K. Kwan. Application of the u-p finite element method to the study of articular cartilage. *J Biomech Eng*, 113(4):397–403, 1991.
- [111] J. W. Weaver and P. R. Johnston. *Finite element methods for structural analysis*. Prentice-Hall, Inc., 1984.
- [112] J. Z. Wu and W. Herzog. Analysis of the mechanical behavior of chondrocytes in unconfined compression tests for cyclic loading. *J Biomech*, 39(4):603–616, 2006.
- [113] T. W. Wu. *Boundary element acoustics : fundamentals and computer codes*, volume 7. WIT Press, Southampton, UK, 2000.

- [114] W. Zhu, V. C. Mow, T. J. Koob, and D. R. Eyre. Viscoelastic shear properties of articular cartilage and the effects of glycosidase treatments. *J Orthop Res*, 11(6):771–781, 1993.